UNIVERSITY OF TRENTO
Department of Physics

Doctoral Dissertation

Nanostructured Materials for Hydrophobic Drug Delivery

Candidate:
Chiara Piotto

Advisor:
Prof. Paolo Bettotti

April 2019


BY NC SA

Acknowledgement

I want to thank all the people who stand by me every day and supported me both scientifically and personally during these years:
my supervisor Prof. Paolo Bettotti, for helping me from both the professional and the personal point of view and for the enthusiasm shown in his researches;
Prof. Graziano Guella, not only for HPLC and NMR measurements, but also for all the advises he gave me;
Prof. Alessandra M. Bossi (Univeristy of Verona) for the ζ-potential analysis, Prof. Andreas Bernkop-Schnürch (University of Innsbruck) who gave me the possibility to perform permeation experiments, Prof. Giorgio Arrigoni (University of Padova) for the MALDI-TOF measurements, Ms. Cristina Armellini (Bruno Kessler Foundation-Trento) for x-ray analysis, MiNALab (Bruno Kessler Foundation-Trento) for the access to the SEM and SCA Östrand (Sweden) for the supply of cellulose material;
the researches of LaBSSAH (Bruno Kessler Foundation-Trento) and of ICRM (CNR-Milano), for fruitful collaborations;
all the members of the NL group, from professors (Marina Scarpa and Lorenzo Pavesi) to researchers and students, who shared with me both moments at university and free time; Maddalena, Claudio, David and Stefano, for supporting me and for the regenerating walks in the mountains;
my relatives and Andrea, for the backing they give me, even if they are far away;
last, but not least, my mother, my father and Elisa, who are always there for me and encourage me to believe in myself.
The very last thank is for the one who, silently, takes care of me.

Contents

1 Introduction

1.1 Thesis motivation

Nanotechnology is heavily accelerating the pace of functional materials development. Benefits of nano-engineered materials can be found in several applications ranging from informatics, automotive, sensing and medicine. In the field of drug delivery (DD) the nanostructured materials are increasingly investigated as drug delivery systems (DDSs), i.e. as vehicles designed to transport and deliver the pharmaceutical compounds to the target place, while protecting them from degradation. The development of DDSs is encouraged by the fact that they overcome some of the main issues in DD: they can be designed to release the drugs in a rate-controlled manner, under specific stimuli and only at the desired place; furthermore, they increase the active ingredients water solubility. The low solubility of a huge number of drugs decreases their bioavailability (defined as the extent and rate at which the active moiety enters the systemic circulation, thereby accessing the site of action) and results in an increase of the medicament dose.

The focus of this work is to understand the physical and chemical processes governing the interactions of hydrophobic molecules with both inorganic and organic nanostructured carriers. I investigate porous silicon (Psi) and nanocellulose (NC) hydrogels as vehicles for β-carotene (BC) and clofazimine (CFZ).

Psi is fabricated from crystalline silicon (c-Si) through an electrochemical etching in hydrofluoric (HF) acid solutions. The silicon corrosion occurs along preferred directions and pores with well defined shapes are formed; both pores dimension and shape can be tuned by changing the experimental parameters. The easy fabrication and the great flexibility in the porous morphology that can be obtained, make Psi a suitable and versatile material for various applications. Concerning DD, Psi is heavily studied since its porosity can reach 80% and its surface/volume ratio is very high (up to several hundreds of m^2/cm^3), thus it allows high drug-loading capacity; nowadays there are already private companies (e.g. pSiMedica Ltd. (UK) and pSivida (USA)) dedicated to manufacture and market DDSs based on Psi. Moreover the fact that it is opaque might encourage its use to protect light-sensitive drugs. Another great advantage is the possibility to individually address the internal pore surface and the external with different functionalization strategies on the same sample (the interior

surface is optimised to the loaded cargo, while the external to hide the particle to the immune system) [1–3]. Once Psi is reduced to nanosize, it becomes an efficient photoluminescent material, thus it can be used as fluorescent tag, too.
Cellulose is the most abundant and renewable polysaccharide in nature and it is characterized by a hierarchical structure based on nanometric fibrils that are extracted from native cellulose by deconstruction reactions. From these nano-sized elements (the so called nanocellulose (NC)) various nanomaterials (such as film, hydrogels and aerogels) can be prepared. Hydrogels are very promising DDSs, since they are three dimensional, hydrophilic networks capable of trapping large amount of water. For this reason they are widely exploited as carriers for hydrophilic drugs and there are only few results about their use for hydrophobic molecules.
In this work I exploit the co-loading of drug and surfactant to increase the lipophilic compounds water solubility. Literature reports contradicting results regarding the surfactant class that provides the highest solubilization capacity for poorly water soluble molecules [4–6]. Moreover, the facts that ionic surfactants could hinder the NC hydrogels formation acting as cross-linkers and that non-ionic surfactants are more effective in solubilizing CFZ in aqueous environment [7, 8], lead me to use the non-ionic ones. Among them I choose Tween-20 (TW20) and Tween-80 (TW80) (Fig. 1.1 reports their structural formula) mainly because they are widely use as excipients in pharmaceuticals.

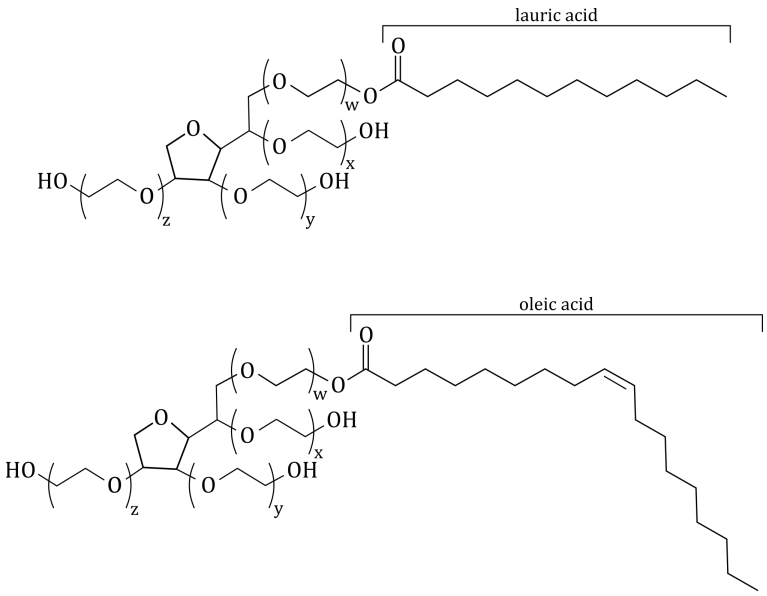

Fig. 1.1: Structural formula of Tween-20 (upper panel) and Tween-80 (lower pannel); for both molecules w+x+y+z=20.

As models of truly lipophilic compounds I use β-carotene (BC) and clofazimine (CFZ) (their structural formula are reported in Fig. 1.2): they absorb in the visible range, thus their quantification down to nmol can be achieved by spectrophotometric method.
BC is the major retinol precursor, providing a substantial proportion of the vitamin

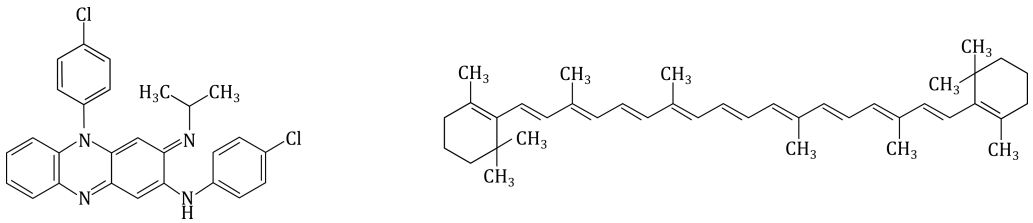

Fig. 1.2: Structural formula of CFZ (left panel) and BC (right panel).

A in the human diet [9] [10]; moreover, due to its well-established antioxidant properties, it protects against some human cancers and cardiovascular diseases [11, 12], arteriosclerosis, macular degeneration and other age related diseases [13]. Having octanol/water partitioning coefficient (logP) equal to 17.5 [14], it is virtually insoluble in water [15] and tend to form microaggregates in aqueous environment which can no longer be enzymatically converted [16]. To increase its aqueous solubility, BC has been successfully encapsulated in liposomes [17], niosomes [13] and alginate-pectin hydrogels [18]; furthertmore it may be solubilized by microemulsions [19], nanoemulsions [20] nanodispersions [21] and by complexation with cyclodextrins [22]. I exploit the facts that BC is insoluble in aqueous media and that it is a delicate molecule (as it is rather sensitive to heat, light and oxygen [23]) to investigate if the carriers (both Psi and NC hydrogels) are inert vehicles and if they can protect this drug from degradation.
CFZ is a highly lipophilic antibiotic (logP=7.13) [24] with very low water solubility (0.225 μg/ml) [25], that is routinely used for leprosy treatment [26, 27]. Its efficacy against inflammatory, Mycobacterium tuberculosis and Mycobacterium avium diseases are demonstrated as well as its in-vitro activity against other members of the mycobacteria and other Gram-positive bacteria [28]. The undesired effects due to its low solubility (such as drug accumulation in tissues and crystal-like drug inclusions formation in macrophages [29–31]) stimulate the development of different strategies to increase its solubility: CFZ salts [32], encapsulation into liposomes [33, 34], water-soluble polymer carriers [25, 35, 36], conjugation onto modified cyclodextrin [37] and amorphous solid dispersions [38].

1.2 Drug delivery

DD refers to approaches and systems designed to deliver pharmaceutical compounds to safely achieve the desired therapeutic effect. There are several administration routes by which a drug can reach the site of action and they are generally classified as enteral (if the drug is delivered through the gastrointestinal (GI) tract, e.g. oral, rectal), parenteral (if the drug is delivered by routes other than the GI tract with a system-wide effect, e.g intravenous) and topical/local (when both the application location and the pharmacodynamic effect is local, e.g. transdermal, inhalation).

For several diseases, the oral delivery remains the preferred route because it is non-invasive, can be self-administered, improves patient compliance and is among the less expensive method. Furthermore, it can provide a long-term, continuous release of the drugs using lower (and thus safer) concentrations resulting in much better efficacy and fewer side effects compared to the intermittent injection therapy [39]. However, many pharmaceutical compounds suffer from poor bioavailability, so that they are unsuitable for conventional oral formulations. Their low bioavailability can be related to the physiology of the GI tract, that is characterised by the following formidable barriers [40–44]:

1. *chemical barrier*: the pH value changes from highly acidic (pH 1.2-3) in the stomach, to neutral or slightly alkaline (pH 6.5-8) in the intestine. Several active ingredients are susceptible to the pH change which may cause drug degradation.

2. *physical barriers*: the first physical barrier is represented by the mucus. It is a complex aqueous mixture of glycoprotein, lipid, salts and cellular debris produced by epithelial cells, that on one hand affords protection for the underlying tissues from various environmental attacks, enzymes and other chemical agents, on the other it may adversely affect the drug absorption. The second physical barrier is constituted by the epithelial cell layer that have to be crossed by the drugs to finally achieve the systemic circulation (either blood or limph). The pharmaceutical compounds can pass through this layer by paracellular or transcellular transport, but also by lymphatic uptake:

    - paracellular transport: if hydrophilic and charged particles are small enough, they may cross the epithelial cell layer by passing between the cells through the junctional complex. Enhancers have been shown to improve paracellular transport either via interactions with the negatively charged cell membrane or by complexing Ca^{2+} involved in the structure of tight junctions [45].

    - transcellular transport: particles are absorbed by intestinal enterocytes at the apical membrane and are subsequently released into the basolateral compartment; the phospholipid bilayers of the cell membrane only support the passive diffusion of lipophilic small molecule drugs, whereas most of the hydrophilic particles are translocated by active transcellular transport (i.e. endocytosis followed by exocytosis).

    - lymphatic uptake: the particles are internalized by highly specialised epithelial cells, the so called M cells of the Peyers patches; these cells have

a unique anatomy and physiology that allow both the rapid delivery of vaccine antigen directly to immune system cells and the drugs absorption via the intestinal lymphatic system, so that the pharmaceutical compounds are protected from hepatic first-pass metabolism (see next item).

To increase the drug permeability across the GI wall, the active ingredients are often administered together with permeation enhancers.

3. *enzymatic barrier* (called first-pass or pre-systemic metabolism): the orally administered drugs face the proteolytic degradation by GI luminal enzymes and by enzymes located inside the intestinal cells (if transcellular transport is involved). Additionally, the majority of the compounds enters the systemic circulation via the portal vein and the amount of available drug is further decreased by the liver enzyme system. To decrease the extent of pre-systemic metabolism, the drugs are often administered with enzyme inhibitors and for highly lipophilic compounds it is possible to relay on intestinal lymphatic transport avoiding the hepatic fist-pass metabolism.

Futhermore, the GI tract is an aqueous environment so that poorly water soluble drugs results in low dissolution rate and elimination of a fraction of the compound prior to absorption, decreasing even further their bioavailability. The facts that an estimated 40% of approved drugs and nearly 90% of the developmental pipeline drugs consist of poorly soluble molecules [46] make the low solubility one of the major problem encountered in formulation development of new drugs. To increase the molecule solubility either chemical or physical modification of the active ingredients and the use of the DDSs have been introduced. These strategies are listed in Fig. 1.3 and described here below.

1.2.1 Chemical modification

Prodrugs Prodrugs are biologically inactive molecules that, once introduced into the body, undergo chemical transformations (usually by enzymes) which activate them; thus they are precursors of the active ingredients [47].

Salt formation Salt formation is one of the most common and effective method of increasing solubility and dissolution rates of highly acidic and basic drugs [48]. However, this strategy cannot be applied to neutral compounds. When dealing with weakly acidic or basic drug the salt formation may often not be practical and, even

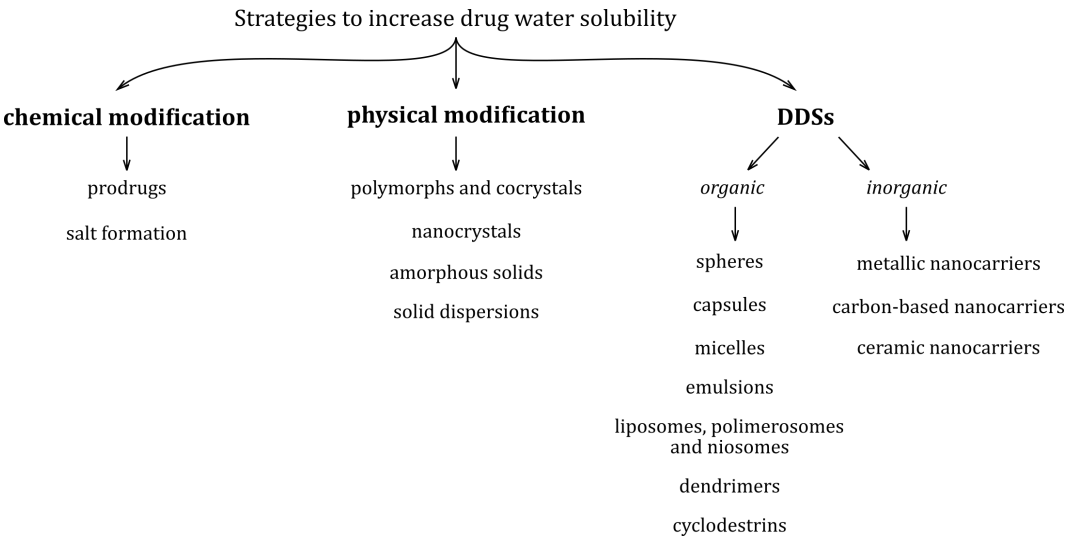

Fig. 1.3: List of different strategies used to increase drug water solubility.

when salts can be prepared, a decreased dissolution rate in the GI tract may be achieved due to the reconversion of salts into aggregates of their respective acid or base forms [49].

1.2.2 Physical modification

Polymorphs and co-crystals The majority of the orally administered drug products is in crystalline state [50] and several efforts have been made to create new solid forms, with superior solubility while preserving the pharmacological properties of the active ingredient. Drug molecules can crystallize as either single- or multi-component. Single-component crystals provide limited opportunity to modulate the physicochemical properties of a compound since they are limited to **polymorphs** whose solubility difference is typically less than two-fold (see Fig. 1.4 A and B). Multi-component crystals (also known as **co-crystals**) are systems constituted by the active ingredient and the coformer bonded together in the crystal lattice with non-covalent interactions. They can be stoichiometric (as in Fig. 1.4) or non-stoichiometric; either molecular (if the active ingredient is neutral, as in Fig. 1.4 C) or ionic (for charged drug, as in Fig. 1.4 D) [51].

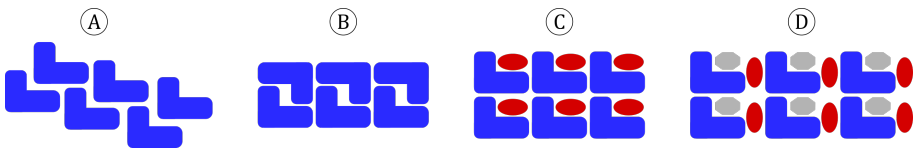

Fig. 1.4: Schematics of polymorphs (A and B) and co-crystals (C and D); blue shapes represent the drug molecules (either neutral or charged), red shapes are the coformers and the gray ones the counterions (present in case of charged drugs) (adapted from [51]).

Nanocrystals One of the oldest strategies for improving drug solubility is the particle size reduction. It has been demonstrated that the reduction of size below 1 μm in diameter gives rise to an increase in solubility (as reported in Fig. 1.5) due to an increase in the solvation pressure and the disruption of solvent-solute interaction which eases the solubilization process [52]. For this reason nanoparticles composed of 100% drug and sized in the range from few nanometers to 1 μm (the so called nanocrystals) have been developed. They can be produced either by reducing the size of a large drug crystal or by aggregating molecules. Most of the oral nanocrystal formulations are solid dosage forms (e.g. tablets, capsules with pellets), but also liquid dispersions exist [53].

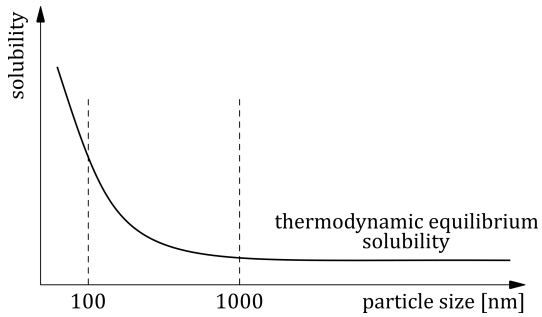

Fig. 1.5: Trend of drug solubility as a function of particle dimension (adapted from [53]).

Amorphous solids Amorphous solids have also been selected for use in drug products, since the transformation of a drug from the crystalline state to an amorphous form leads to an increase in solubility; however, the high-energy amorphous state is not stable and needs to be stabilized, for example using the amorphous solid dispersion [51].

Solid dispersions Solid products consisting of at least two different components, matrix and drug, are defined as solid dispersions [54]. The drug can be dispersed molecularly, in amorphous or in crystalline particles; moreover the matrix can be either in crystalline or amorphous state [55].

1.2.3 Drug delivery systems

DDSs are vehicles designed to carry the drug to the desired place, while preserving the cargo integrity. They are used in several administration routes to improve drug bioavailability (in the particular case of oral DD they are exploited to improve drug stability, solubility and permeability) [56–59].
When dealing with orally administered carriers two different strategies can be adopted:

- the vehicles either adhere to the mucus layer or to the epithelial tissue releasing their content; then the active ingredients penetrate the GI walls to reach the systemic circulation;

- after being in contact with the mucosal surface, the carriers themselves either enter the GI barrier to deliver their content inside epithelial cells or cross the GI barrier to deliver the drug to the systemic circulation or even to the target organ. The possible mechanisms to pass through the GI barriers are the same described above for the active ingredients [39, 44].

Here I give an overview about DDSs surface chemistry and size that are crucial characteristics to develop any drug carrier; furthermore, the diverse organic and inorganic DDSs are summarised.

External surface functionalization

The outer surface of the carriers is of paramount importance and has to be designed considering how it will interact with the physiological environment. Carrier solubility, stability against aggregation, interactions with biomolecules and crossing of physiological barriers have to be considered to maximize the efficacy and minimise toxicity of the treatment [60, 61].
Concerning oral DD, an important challenge is to maximize the retention time in the intestine to increase the absorption probability. Bioadhesive materials (such as polyvinyl alcohol (PVA) or polyethylene glycol (PEG)) are used to increase the transit time of the DDSs in the GI tract, resulting in prolonged time window either for the release of the payload or for their absorption into the intestinal cells. Moreover, enhanced drug absorption could occur because of the increased effective surface area in contact with the intestinal mucosa upon material swelling: swollen material fills the crevices of the mucous membrane and yields to a high local concentration of the drug [62–64].
The particle uptake and translocation dependence on hydrophilicity and surface charge of the carriers is still a controversial issue [65–68]; probably the complexity of the interactions, that strongly depend on the system under investigation, does not allow to obtain general rules.
A strategy that has been investigated to improve the carrier absorption across the intestinal epithelium is to couple the vehicles with targeting ligands that are specific for receptors expressed at enterocyte or M cell surface [69, 70].
If the orally administer DDSs are designed to enter the blood circulation, they finally come in contact with blood cells and plasma proteins, therefore their surface may experience non-specific protein adsorption (opsonization), making them more visible

to phagocytic cells [71]. To reduce protein adsorption, prevent agglomeration and increase circulation time a PEG coating can be exploited [71, 72].

Particle size

The in vivo distribution, biological fate, toxicity and targeting ability of DDSs is determined also by the vehicle size [73], as it plays a key role in the adhesion to and interaction with the biological cells [39, 74]; moreover, it affects the movement of the carriers in and out the vasculature [75]. The particle size should be optimized, depending on the administration route and the targeted cells: for carriers injected into tissue or inhaled they should be smaller than 200 μm and 100 μm [76]. The vehicles released into circulation can have dimensions up to 10 μm, but usually they are much smaller (the smallest capillaries in the body are 5-6 μm in diameter and the particles should be small enough to avoid aggregation and embolism). Once in the bloodstream, nanocarriers smaller than 10 nm are rapidly cleared by the kidneys or through extravasation, while larger nanoparticles have higher tendency to be cleared by cells of the mononuclear phagocyte system (MPS) [71]. Oral DDSs can have dimensions ranging from few nanometers up to few millimeters; generally, nanoparticles have relatively higher intracellular uptake compared to microparticles and, due to their small size and relative mobility, they are available to a wider range of biological targets [77]. For example, in Caco-2 cell line 100 nm size DDSs showed 2.5 fold greater uptake compared to 1 μm size carriers and 6 fold higher uptake compared to 10 μm microparticles. Using a rat in situ intestinal loop model, it has been demonstrated that the uptake efficiency of 100 nm vehicles is 15-250 fold greater than larger (1 and 10 μm) microparticles [78]. Furthermore, nanoparticles penetrate throughout the submucosal layers, while microparticles predominantly remain in the epithelial lining [79]. The importance of size for the biological fate of particles, has been investigated also for DDSs internalised by the Peyers patches: the larger ones (>5 μm) are typically retained in the Peyers patches, while the smaller particles escape this site to disseminate via the lymphatics to more distant sites [80].

The dimensions of the carrier influence its absorption and its stability, too; in fact during storage smaller particles have greater tendency to aggregate. Particle dimensions affect also the drug release profile: smaller particles have a larger surface/volume ratio, so that most of the drug is at or near the carrier surface and this is reflected in a faster drug release. On the other hand the larger DDSs allow more drug to be encapsulated per particle and give slower release [58, 81].

Organic DDSs

The most investigated materials use to fabricate organic DDSs are polymers and lipids and carriers with diverse geometries can be obtained (their basic realizations are reported in Fig. 1.6).

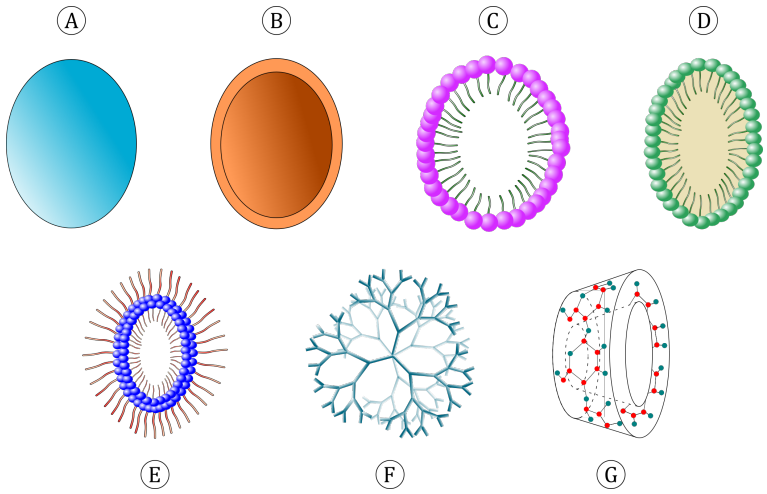

Fig. 1.6: Schematics of the most used organic DDSs: A) sphere, B) capsule, C) micelle, D) emulsion, E) liposome, polimerosome, niosome, F) dendrimer and G) cyclodestrin.

Spheres They are classified in lipid spheres, polymeric spheres and polymeric hydrogels.

The most common **lipid-spheres** are the solid-lipid nanoparticles (SLNs), that possess a solid lipid matrix core and the nanostructured lipid carriers (NLC), whose matrix is composed of both solid and liquid lipids that improve drug loading and increased stability on storage thereby reducing drug expulsion. Both these vehicles are stabilized by surfactants or polymers to prevent particle agglomeration and opsonization [82, 83].

Polymeric-spheres possess a core structure which can be varied by changing the composition of the hydrophobic and the hydrophilic blocks on the polymer chains. They are mainly produced by solvent evaporation, emulsion polymerization and sedimentation polymerization [84, 85].

Polymeric hydrogels are obtained if the cross-linked networks of hydrophilic polymers absorb large amount of water (up to 90% of their weight) while keeping the 3D structure of the polymer network (more details cane be found in Chap. 3.2).

Capsules Capsules are systems characterized by a core-shell structure. The core is usually constituted by water or oil (these capsules are fabricated starting from w/o or o/w emulsion), but also SLN and polymeric spheres are used. The shell is obtained through interfacial polymerization, interfacial precipitation or LbL deposition. Even if the majority of the capsules have a polymeric shell, also entirely lipidic capsules can be prepared: they have an internal liquid or semi-liquid oil core and an external lipid

layer that is solid at room temperature. These lipidic capsules should be stabilized by surfactants or by polymers to prevent particle agglomeration and opsonization [82, 84, 86–89].

Micelles Micelles are thermodynamically stable aggregates of amphiphilic molecules in water, which under certain conditions self-aggregate to minimize their surface energy, creating a hydrophobic core with a hydrophilic outer surface. Shape and dimensions of these carriers depend on the type of molecules and the environment. The majority of the micelles are made either of lipids (e.g. phosphatidylcholine and bile salts) or of amphiphilic copolymers [90, 91].

Emulsions Emulsions can be obtained when a third component that is insoluble in water (e.g. oil) is added to the water-amphiphile mixture. Under certain conditions a stable, transparent and isotropic phase is obtained that contains large quantities of both water and oil. Depending on whether the system is thermodynamically or kinetically stable, one can distinguish between micro- and nano-emulsion. Recently it has been developed the so called self-emulsifying DDSs (SEDDSs) that are used for oral DD: drug, oil and large quantity of surfactants are inserted inside a gelatin capsule; upon dilution with water these three ingredients form an emulsion [92].

Liposomes, polimerosomes and niosomes Liposomes, polimerosomes and niosomes are hollow shell carriers constituted by a double layer membrane enclosing a hydrophilic environment, that enable the encapsulation of water-soluble molecules. Hydrophobic drugs can be segregated in the vesicle membrane. Liposomes are constituted by one or more bilayers consisting of amphiphilic lipid molecules concentrically oriented around an aqueous compartment [93]. Polymersomes differ from liposomes by the fact that the membrane is made of amphiphilic block copolymers [94], while that of niosomes results from the self-assembly of hydrated surfactant monomers [13].

Dendrimers Dendrimers are nano-sized monodisperse polymeric molecules with a typical branched structure that grows as a kind of "L-system" around an inner core. They are made of several layered building blocks formed by repeated units and multiple peripheral functional groups. The dendrimer interior is usually hydrophobic, whereas the exterior surface is hydrophilic [95].

Cyclodextrins Cyclodextrins are cyclic oligosaccharides with a hydrophilic outer surface and a hydrophobic central cavity. The fact that these molecules are relatively large with a number of hydrogen donors and acceptors, prevent their permeation through the lipophilic membranes. They are mainly used as complexing agents since

they increase drug water solubility, enhancing their bioavailability and stability [96, 97].

Inorganic DDSs

Here I give a brief overview about metallic, carbon-based and ceramic nanocarriers; details can be found in literature [58, 81, 98–100].

Metallic nanocarriers Metallic nanospheres (in the range 1-200 nm) and nanocapsules (hollow metal nanoshells) are often made of gold, silver, platinum, palladium gadolinium and nickel. These carriers are characterized by large surface area that enables the incorporation of high drug amount (a 2 nm Au nanoparticle could, in principle, be conjugated with hundred drug molecules). The possibility to modify their surface with various functional groups enable both drug loading and targeted DD. Metallic carriers are not biodegradable and their toxicity is still of concern.

Carbon-based nanocarriers Carbon nanotubes and fullerenes are hollow, cage-like architectures that have received much attention recently, even if some studies suggest a possible toxicity of these materials.
Carbon nanotubes are obtained by self-assembling sheets of atoms rolled up in tubular shape. It is possible to fabricate both single-wall and multi-wall carbon nanotubes. The first are constituted by a single cylindrical graphite sheet (diameters in the range 0.7-1.5 nm), while the multi-wall carbon nanotubes are characterized by several (from 2 to 30) concentric tubes; the diameters for the inner tubular layer is in the range 2-10 nm, yet the resulting external diameter range from several nanometers to tens of nanometers (an extra thickness of about 0.7 nm is added for each extra layer).
Fullerenes are carbon allotropes constituted by tens of atoms resulting in polygonal structures with diameters in the order of 1 nm. Their geometry and size make them appealing as DDSs, provided that they are subjected to a proper surface functionalization to render them biocompatible.

Ceramic nanocarriers Ceramic nanocarriers are porous vehicles made of silica, alumina and titania. They are characterized by a high drug loading capacity, due to their very large surface area and pore volume. They are very stable against chemical (pH), physical (heat) stress and in aqueous environment. The silica nanoparticles are the most investigated: they are synthesized in basic or acidic conditions through polymerization of silica species on surfactant template, which is then removed by high temperature calcination or organic solvent extraction. The fact that the mesoporous silica-based framework is produced by a sol-gel process, allow

to control very precisely the particle size. The first mesoporous silica carriers used in DD was MCM-41 (Mobil Composition of Matter-41) and later also SBA (Santa Barbara Amorphous), HMS (hollow mesoporous sphere) and MSU (Michigan State University) have been employed as DDSs.

1.3 Mathematical models of diffusion

Given the huge amount experimental trials needed to develop and optimize a pharmaceutical product, the availability of mathematical models to describe the release profile of the drug, would save large amount of time and help in reducing costs. Drug diffusion models are classified in two main families: mechanistic and empirical. Those based on physico-chemical phenomena, such as diffusion, dissolution, swelling, erosion, precipitation and degradation of the DDS are defined as mechanistic mathematical theories; depending on the complexity of the resulting set of mathematical equations, either analytical or numerical solutions can be derived. Generally, by increasing the model complexity, the accuracy of a mathematical theory is increased, however too complex models might be cumbersome to use. In the case of empirical models, the mathematical treatment is not based on real physical, chemical or biological phenomena. Although, no or very limited insight into the underlying drug release mechanisms can be gained, these theories are often used to compare different types of drug release profiles, yet caution must be paid to draw mechanistic conclusions or to make quantitative predictions.
Here I give an overview about the modelling of diffusion-controlled DDSs, neglecting carrier erosion, swelling and degradation.

Diffusion is the spontaneous net movement of molecules along the concentration gradient. Fick's laws are used to quantify the diffusional mass transport: the first law describes the steady-state diffusion, i.e. when the concentration within the diffusion volume depends only on position and does not change with respect to time, while Fick's second law describes the non-steady state diffusion.
Fick's first law relates the diffusion flux (J) (i.e. amount of drug particles that passes through a unit area per unit time) to the position-dependent drug concentration (c) under the assumption of steady-state:

$$J = -D \cdot \nabla c \tag{1.1}$$

where D is the drug diffusion coefficient (also called diffusivity). The minus sign shows that diffusion tends to nullify the concentration gradient.
The Fick's first law is not sufficient to completely solve the problems of diffusion, since the diffusional flux can modify the concentration gradient that, often, is

time dependent. Starting form the first law and taking into account mass balance considerations, the Fick's second law can be derived:

$$\frac{\partial c}{\partial t} = -\nabla \cdot J = \nabla \cdot (D \nabla c) \tag{1.2}$$

where all the parameters have the same meanings as in the first law, except that c is the time- and position-dependent drug concentration and t is time.
Generally the mathematical treatment of the Fick's second law is heavily simplified if "perfect sink conditions" are assumed (i.e. very dilute and well stirred solutions are used in such a way that the released drug is immediately carried away from the device into the fluid) and if D is constant (matrix erosion, swelling and degradation might give rise to a time, concentration and position dependent D), so that Eq. 1.2 can be rewritten as:

$$\frac{\partial c}{\partial t} = D \cdot \nabla^2 c \tag{1.3}$$

As for any differential equation, both initial and boundary conditions have to be supplied, to solve it. The solution of the diffusion equation is the drug concentration profiles during the release (i.e. $c(t, x, y, z)$); by integrating this solution it is possible to obtain the amount of drug released at time t (M_t). Usually it is normalised with respect to the amount released at infinite time (M_∞), obtaining the fractional release of the drug, $\frac{M_t}{M_\infty}$.

When dealing with diffusion-controlled delivery systems, it is crucial to distinguish between reservoir and monolithic systems. In the "reservoir system" or "core-shell system" the drug is located at the center of the dosage form and is surrounded by a membrane that constitute the release rate controlling barrier, so that the drug depot and the membrane are physically separated. In the case of "monolithic system" (also called "matrix system") the drug and the release rate controlling material are homogeneously distributed throughout the device. Here only monolithic systems are reviewed and details about reservoir dosage forms can be found in literature. Another important information deals with the initial drug concentration inside the device: if it is below the drug solubility the dosage form is referred as "solution", while if it is above the device is called "dispersion". Moreover, the DDS geometry significantly affects the resulting drug release kinetics; here slab (i.e. thin film with negligible edge effects) and sphere are discussed, yet other geometries are reported elsewhere [101–103].

1.3.1 Mechanistic models

Monolithic solution

One of the most common case is the one of a drug homogeneously dispersed inside a matrix, thus Fick's second law is subjected to the following initial and boundary conditions:

- the drug is initially uniformly distributed throughout the matrix;
- the initial drug concentration is below its solubility;
- the drug D is position and time independent;
- perfect sink conditions are maintained throughout the experiment.

The resulting release for slab and sphere are the following [104]:

$$\text{slab} \qquad \frac{M_t}{M_\infty} = 1 - \frac{8}{\pi^2}\sum_{n=0}^{\infty}\frac{1}{(2n+1)^2}exp\Big(-\frac{D(2n+1)^2\pi^2 t}{L^2}\Big) \tag{1.4}$$

$$\text{sphere} \qquad \frac{M_t}{M_\infty} = 1 - \frac{6}{\pi^2}\sum_{n=1}^{\infty}\frac{1}{n^2}exp\Big(-\frac{Dn^2\pi^2 t}{R^2}\Big) \tag{1.5}$$

where M_t and M_∞ represent the absolute cumulative amounts of drug released at time t and at infinite time, respectively; L the slab thickness and R the radius of the sphere.

Monolithic dispersion

Higuchi [105] considered the drug release from an ointment thin film into the skin, with the following conditions:

- the initial drug concentration within the system is much higher than the drug solubility within the matrix (i.e. pseudo-steady-state);

- the geometry of the carrier is that of a thin film with negligible edge effects (one-dimensional diffusion);
- the size of the suspended drug particles is much smaller than the film thickness;
- the carrier material does not swell or dissolve;
- the drug D is time and position independent;
- perfect sink conditions are maintained throughout the experiment.

With the aforementioned assumptions the rate of release follows a square-root time dependence:

$$M_t = A\sqrt{(2c_0 - c_s)c_s Dt} \tag{1.6}$$

where A the surface area of the film exposed to the release medium, c_0 and c_s the initial drug concentration and the solubility of the drug in the carrier material, respectively. The Higuchi equation was initially developed for a slab that releases the drug through one of the two faces: a prefactor 2 should be added if the release occurs through both sides of the thin film.

Baker and Lonsdale [106] presented an implicit mathematical equation to extend the Higuchi model to spherical dosage forms:

$$\left[1 - \left(1 - \frac{M_t}{M_\infty}\right)^{\frac{2}{3}}\right] - \frac{2}{3}\left(\frac{M_t}{M_\infty}\right) = 2\left(\frac{c_s}{c_0}\right)\frac{Dt}{R^2} \tag{1.7}$$

where R is the matrix radius. This equation can be used up to time $t = \frac{R^2}{6D} \cdot \frac{c_s}{c_0}$, that corresponds to the point when no more undissolved drug is present inside the device. Afterwards, the release should be described using the infinite series expression (Eq. 1.4), yet this accounts to the very last part of the release process (especially when $c_0 \gg c_s$) [102].

A very similar approach has been proposed by Koizumi and Panomsuk [107] to obtained an approximate equation that can be used when dealing with spherical devices. Eq. 1.8 has the advantage to be an explicit form, thus, it is easier to solve:

$$M_t = 4\pi d^2 \left[\sqrt{2c_s(c_0 - c_s)Dt} + \frac{4c_s}{9d} \left[\frac{c_s}{2c_0 - c_s} - 3 \right] Dt \right] \tag{1.8}$$

where d is the beads diameter. Obviously, also this model is only valid as long as the drug concentration in the matrix largely exceeds its solubility.

The square-root time dependence

The solution to Fick's law obtained in the form of a trigonometric series in the case of thin film (Eq. 1.4) can be rewritten in terms of an error function series, that is useful for interpretation of short time behaviour [108]:

$$\frac{M_t}{M_\infty} = 4\sqrt{\frac{Dt}{L^2}} \left(\frac{1}{\sqrt{\pi}} + 2 \sum_{n=1}^{\infty} (-1)^n \mathit{ierfc} \frac{nL}{2\sqrt{Dt}} \right) \tag{1.9}$$

where $\mathit{ierfc}(x)$ represents the integrated complementary error function of x.
For small times (i.e. $M_t/M_\infty < 0.60$) the second term in the brackets vanishes, so that the short time approximation can be written as:

$$\frac{M_t}{M_\infty} = 4\sqrt{\frac{Dt}{L^2}} \tag{1.10}$$

A proportionality between the cumulative amount of drug released and the square-root of time is obtained both when drug delivery is approached by the Higuchi equation (see Eq. 1.6) and by solving the Fick's low for a slab monolithic solution (see Eq. 1.10); this means that a square-root of time dependence of the drug transport can be based on very different physical circumstances (dispersions versus solutions). However, since the dominating release mechanism in both cases is diffusion, this proportionality is commonly regarded as an indicator for diffusion-controlled drug release. Yet, a square-root time kinetics does not necessarily mean that the underlying drug release mechanism is diffusion-limited, in fact the superposition of other physical-chemical phenomena (such as swelling, degradation, time- and position-dependent changes in the diffusion coefficients) might result in an apparent square-root of time kinetics [108, 109].

1.3.2 Empirical models

Despite mechanistic models make explicit connections between the drug release and the physico-chemical parameters of the system, their use is limited to those DDSs

that strictly fulfil the model requirements. For this reason empirical models are also widely used.

0^{th}-order model

When the drug diffused from the carrier at constant rate, its release is described by a 0^{th}-order kinetic; assuming that there is no drug dissolved at time t=0, the equation for 0^{th}-order release is:

$$M_t = kt \tag{1.11}$$

where k is a constant. In principle, this release profile leads to the best control of drug concentration, improves patient compliance and reduces the frequency of drug administration, so that 0^{th}-order release is the ultimate goal of many controlled-release drug delivery system.

1^{st}-order model

This model has been introduced by Noyes and Whitney [110] when studying the effect of concentration on the rate at which a solid substance dissolves in solution. In accordance with the laws of diffusion, it is proportional to the difference between the substance solubility and its concentration at time t; the mathematical expression is:

$$\frac{\partial c}{\partial t} = k(c_s - c) \tag{1.12}$$

where k the is the first order proportionality constant.
After integration:

$$c(t) = A(1 - e^{-kt}) \tag{1.13}$$

where A is a constant.

Nowadays this model is generally used to describe the pharmaceutical dosage forms which release the drug proportionally to the amount of drug remaining in its interior, so that the amount of drug released by unit of time decreases with time. Since it is difficult to conceptualize the underling mechanism on theoretical basis, it is classified as an empirical model [111, 112].

Power law model

To describe the first 60% of the fractional release from polymeric systems (with position and time independent D), Peppas and co-workers introduced a semi-empirical model, widely known as power law model [113]:

$$\frac{M_t}{M_\infty} = At^n \tag{1.14}$$

where A is a constant incorporating geometrical and structural characteristics of the system (drug and carrier) and n the release exponent, which might be indicative of the transport mechanism, as reported in table 1.1.

Tab. 1.1: Exponent of the power law and drug release mechanism from polymeric DDSs of different geometry.

Slab	Cylinder	Sphere	Drug release mechanism
0.5	0.45	0.43	Fickian diffusion
0.5<n<1	0.45<n<0.89	0.43<n<0.85	Anomalous transport
1	0.89	0.85	Polymer swelling

There are two extreme for the exponent n, whose values depend on the system geometry: if $n = n_{min}$ the dominating mechanism is fickian diffusion, while $n = n_{max}$ indicates a swelling-controlled drug release. Values of n between n_{min} and n_{max} can be regarded as an indicator for the superposition of both phenomena (anomalous transport).

Weibull model

The mathematical expression for the Weibull function (or stretched exponential) is:

$$\frac{M_t}{M_\infty} = 1 - e^{-at^b} \tag{1.15}$$

where a and b are constants.
Although this model is used to fit and characterize diffusion-controlled experimental data [114–117], it has two fundamental drawbacks. First of all, it does not capture the correct limits imposed by the diffusion equation for short and long times; secondly, although Papadopoulou et al. [118] developed a methodology to elucidate the release mechanisms based on the value of b, the empirical Weibull function is still

criticized because of the lack of a physical interpretation that could give a meaning to its fitting parameters in the context of diffusion-controlled release [119].

2 Porous silicon

2.1 Introduction to porous silicon

Porous silicon (Psi) is a nano- to micro-structured material accidentally discovered during electropolishing of c-Si by A. Uhlir in 1956 [120]. For decades it was considered a non-stoichiometric oxide, a sacrificial material obtained in corrosion processes. However, in 1990 the discovery of visible luminescence of Psi under UV illumination by Canham [121] attracts a large research interest related to the possibility to fabricate silicon-based active optoelectronic devices. Since then, Psi properties have been largely investigated: its controllable pore size, its convenient surface chemistry, the ability to modulate its refractive index as a function of porosity, its large surface area and its efficient visible light emission make Psi a suitable material for applications ranging from photonics and optoelectronic to biosensing and biomedicine.

2.1.1 Psi fabrication and morphology

Psi is fabricated by electrochemical process that allows for the production of very uniform porous layers with good reproducibility, without the need of complex set-up. To perform electrochemical etching, c-Si is oxidized in HF solution (see Fig. 2.1).

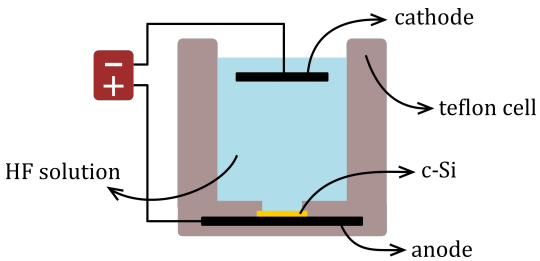

Fig. 2.1: Schematic of the electrochemical etching set-up: c-Si is in contact with HF solution and electrically contacted to an anode; a platinum cathode is immersed in the etching solution. Generally the electrochemical reaction is controlled by imposing the current density.

Both p-type (p-Si) and n-type (n-Si) silicon can be exploited to fabricate porous layers: the main difference relies on the fact that the semiconductor-electrolyte junction is polarised in the opposite way when donor or acceptor doping are used. Since the electrochemical etching is performed under anodic condition, p-Si is

polarised in forward bias, while n-Si in reverse bias (see Fig. 2.2).

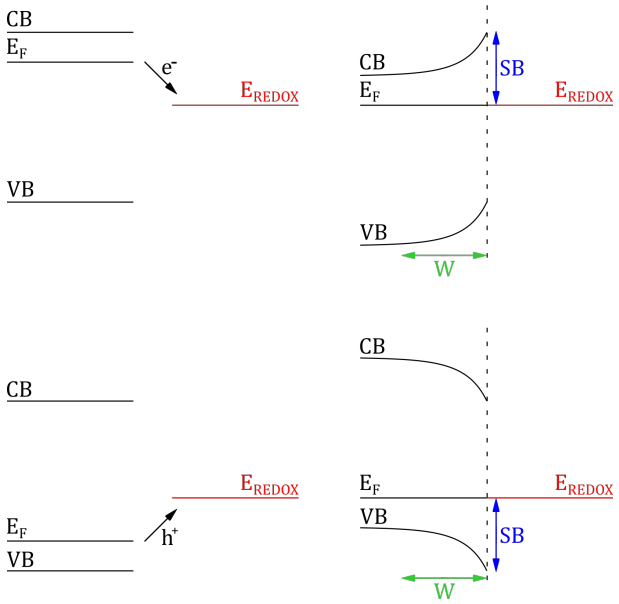

Fig. 2.2: The energetics of the semiconductor-electrolyte junction is determined by the relative position of the energy levels: Fermi level (E_F) for the semiconductor side and REDOX potential (E_{REDOX}) for the electrolyte side (VB and CB represent the semiconductor valence and conduction bands). When semiconductor and electrolyte are brought into contact, equilibrium is reached between the electrochemical potential of the two species. Since HF solutions are used, the E_F(Si) should be compared with the redox potential of F^-, because F^- is the oxidant specie. In the case of n-Si (upper panel), since E_F(n-Si)>E_{REDOX}(F^-), the electrons flow from the semiconductor to the solution; this creates a positively charged region ("space charge region" or "depletion layer", indicated as W) in the solid material near its surface. The resulting electric field is shown by the upward band-bending with respect to the level in the bulk semiconductor. In the case of p-Si (bottom panel) E_F(p-Si)<E_{REDOX}(F^-), yet a similar discussion can be done, considering holes instead of electrons: W is negatively charged and the bands are bent downward. In both cases, when equilibrium is reached, an energy barrier for the majority carriers is established in the junction (SB), that resembles the situation described in the Schottky-model for semiconductor-metal junction. The electrochemical etching is performed under anodic condition, that means reverse biasing for n-Si and forward biasing for p-Si.

Despite the exact chemistry that occurs at the silicon surface during the electrochemical etching is still pending, a schematic chemical dissolution reaction path has been proposed by Lehmann [122] to qualitatively describe the formation of pores under commonly used etching conditions (see Fig. 2.3).
The model assumes that, after native oxide dissolution, the semiconductor surface is covered by Si-H. A hole reaching the surface (either by diffusion or by an applied electric field) weakens the Si-H bond and eases the dissolution of superficial silicon atoms (the exact chemistry of the reaction products is still debated). The hydrogenated surface is attacked by the HF species, forming Si-F bonds and gaseous H_2 is generated. The ionic nature of the Si-F bond reduces the electron density of the Si-Si backbone atoms; these are sufficiently polarized to be broken by HF. The released

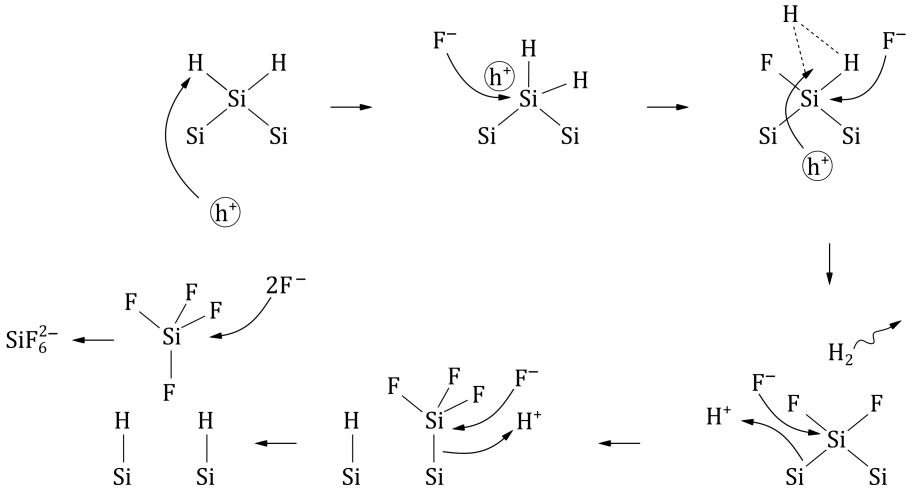

Fig. 2.3: Reaction model of the silicon oxidation (adapted from [123]). This scheme can be summarised by the following reactions: $Si+2F^{-}+2h^{+} \rightarrow SiF_2$ and $SiF_2+4F^{-}+2H^{+} \rightarrow SiF_6^{2-}+H_2$, where H represents a hydrogen atom and h stands for "hole".

gaseous SiF_4 reacts with HF to form SiF_6^{2-}. At the end of an HF etching, the Psi samples contain primarily Si-H, Si-H_2, and Si-H_3 surface groups and only traces of O and F [124–127]. This seems puzzling, considering that Si-F is thermodynamically the most stable bond of all silicon chemistry (the relative strength of bonds increases in the order Si-H<Si-O<Si-F [123]). Actually the hydrogen atom is much less electronegative than fluorine and a hydride-terminated surface is less susceptible to nucleophilic attack.

According to this model, holes are required at the semiconductor-electrolyte interface to weaken the superficial silicon atoms bonds, allowing the corrosion to occur. In n-Si the majority carriers are electrons, so that the holes should be artificially created in order to sustain the electrochemical etching (at least in lightly doped substrates, with resistivity higher than 0.1 Ωcm). This can be done by back illuminating the semiconductor and to force holes to drift towards the surface by applying an electric filed.

Despite being known since decades, silicon electrochemistry is still an active field of research. For example recently it has been demonstrated that the electrochemical corrosion occurs in highly doped n-Si also without illumination [128]. In this case the minority carrier concentration is not enough to explain why the corrosion reaction occurs and an alternative holes formation mechanism has been proposed [129]: holes can be generated at the surface by the tunneling of the valence band electron through the space charge layer into the conduction band; the fact that electrochemical corrosion of n-Si without illumination occurs only for high dopant concentrations is because this mechanism is possible only when the band bending is sufficiently large to make tunneling possible.

The Lehmann model does not take into account that the etching solution can contain nucleophilic species that can compete with fluorine ions; in this case not only

electrochemical but also chemical etching occurs. The chemical etching proceeds by the formation of an oxide that is dissolved either by HF or by hydrolysis [123]. However, the chemical etching can be neglected, unless significant quantities of Si-O species are formed; this happens when oxidants are added to the HF solution or when very high current density are used so that the HF diffusion to the silicon surface can not keep up with the rate of delivery of valence band holes (the so called "electropolishing").
The Psi formation region and the electropolishing regime can be clearly distinguished looking at a typical iV curve, as that reported in Fig. 2.4. For current densities below a certain threshold Psi is obtained. Above the so-called "electropolishing peak" the current density is so high that the silicon interface exposed to the acid is homogeneously and completely removed. The electropolishing can be exploited to lift-off the porous layer by applying a burst of current after its formation.

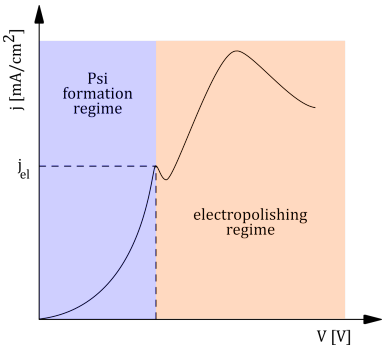

Fig. 2.4: Typical Psi iV curve: for current density below the electropolishing peak, the pores grow in a stable manner.

It is generally accepted that the initiation centres for the formation of the pores are the defects on silicon surface, where localized regions of large current density form. [130]. The high density of nucleation sites is reflected to the fact that the first few tens of nanometers of the superficial porous layer (called "transition layer") have a pore distribution that differs from the one representing the steady growth condition (see Fig. 2.5 taken from [131]). The superficial pores stop their growth because the larger ones collect more carriers than the smaller, increasing their growth rate. The depletion layer that forms around these larger pores collect all the carrier so that the smaller have no more holes available.

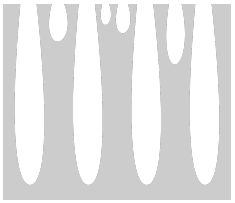

Fig. 2.5: Schematic of transition layer and steady growth condition.

The great control over porous structure enabled by electrochemical corrosion, makes Psi very advantageous compared to other porous materials. Of particular importance are the following parameters:

1. pores grow along selected crystalline directions;

2. the porosified layer is passivated against corrosion and an increase in etching time is reflected in porous layer thickening;

3. c-Si doping level determines the order of magnitude of the pore size; a finer control on pore dimensions can be achieved tuning the HF concentration and the value of the current density.

Once a pore begins to grow, the small radius of curvature at its bottom generates a region of enhanced electric field that attracts valence band holes: the dissolution occurs faster at the pore tip, creating a tubular structure that propagates along the high atomic density direction. Using (100) c-Si wafer orientation, the pores grow perpendicular to the substrate surface and run parallel one to each other; the pore branching is generally limited, unless high current densities are used (as discussed later on). Instead, with (110) and (111) c-Si orientations, the pores form a complex and three-dimensional network with quite well-organized pores, nevertheless their structure is less homogeneous and they have found limited use so far [132].
A peculiar aspect of Psi formation is that the porosified layer is passivated against further electrochemical etching: once formed, the pores do not redistribute or collapse and the porosity remains approximately constant over the whole layer [133]. In fact, when the depletion zones of two adjacent pores meet each other, the current flow is pinched off (since holes cannot reach the silicon surface) and further silicon dissolution is blocked. Thus the increase in etching time causes the porous layer to thicken and porosity variation is obtained using a time-dependent current profile (see Fig. 2.6).
Silicon doping level is used to select the average size of the pores: macropores (with diameters in the range of μm) are formed using lightly doped c-Si ($\rho \simeq 10$ Ωcm), mesopores (100's nm) with moderately doped substrates ($\rho \simeq 10^{-2}$ Ωcm) and nanopores in heavily doped c-Si ($\rho \simeq 10^{-3}$ Ωcm). Once the c-Si resistivity has been chosen, a finer control on the pore dimension can be achieved by tuning both the HF concentration and current density. The evidence that the increase in HF concentration causes the decrease in pore dimensions can be related to the fact that pore nucleation is a thermally activated process (activation energy of about 0.35 eV [122]). Thus, increasing HF concentration, the probability to activate a dissolution process on a certain point is increased too; as a consequence, more pores start to grow, causing the decrease in their average diameter. Considering the dependence of pore size on current density an opposite behaviour is observed.

In fact, if the current density is increased, the holes are not consumed at the pore tip and they can contribute to the pore enlargement; when the current assumes very high values, pore branching occurs, since the holes that are not completely consumed at the bottom of the pore diffuse towards the surface stimulating the etching along defined crystalline directions. As highlighted previously, when the current is further increased the holes density is so high that the silicon atoms are removed isotropically (electropolishing).

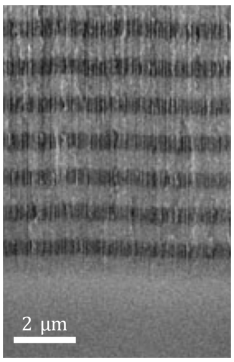

Fig. 2.6: Cross section SEM image of Psi sample obtained with a time-dependent current profile: high porosity regions are the darker layers, while the lighter bands correspond to low porosity layers. Pores maintain the same dimensions irrespectively of their depth, thus demonstrating the Psi passivation.

2.1.2 Estimation of Psi porosity

Porosity can be estimated from the Bruggeman effective medium theory using the formula [134, 135]:

$$f \cdot \frac{n_b^2 - n^2}{n_b^2 + 2n^2} + (1 - f) \cdot \frac{n_a^2 - n^2}{n_a^2 + 2n^2} = 0 \tag{2.1}$$

where f indicates the fraction of silicon in the porous layer, d and n are the layer thickness and refractive index respectively. n_a and n_b the air and silicon refractive index (in the IR region n_a=1 and n_b=3.4).
To obtain n one can exploit the fact that the porous layer can be seen as a dielectric mirror that creates interference effects, as shown in Fig. 2.7. When a light wave impinges on the Psi surface, the reflected spectrum is characterised by well known fringes. The quality of the interference of porous layer depends on the thickness of layers, their refractive index difference, the number of layers and smoothness of their interface. For a single thin layer, the interference pattern directly depends on n and d, so that if one of the two is known (for example d can be obtained from SEM analysis), the other can be calculated with the following expression [136]:

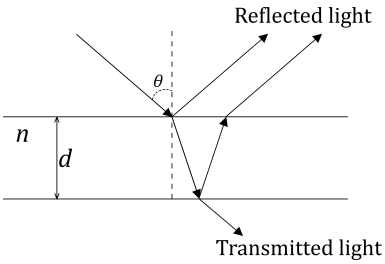

Fig. 2.7: Schematic of the light beam reflection when it hits a layer with thickness d and refractive index n with an incident angle θ.

$$d = \frac{N}{2 \cdot W \cdot \sqrt{n^2 - (sin\theta)^2}} \tag{2.2}$$

where θ the angle of incidence and N the number of periods observed within the wave-number region considered (W). When the incident angle θ is $0°$ (as in the case of the used micro-FTIR), Eq. 2.2 can be simplified to

$$nd \simeq \frac{N}{2 \cdot W} \tag{2.3}$$

Another strategy to estimate the porosity is the gravimetric measurement, yet this method is less accurate than the optical one, especially in the case of small samples.

2.1.3 Psi surface chemistry

The as-etched Psi spontaneously undergoes chemical modifications, thus a crucial step in the Psi fabrication is its surface stabilization. This is achieved by either oxidation or functionalization, as described below.

As-etched Psi and its surface oxidation

The limited stability of hydride species (Si-H$_x$) produces an unstable Psi surface that spontaneously oxidise. Samples stored in air are contaminated by chemical species (mainly oxygen and carbon), thus "aged" Psi contains a native oxide of highly variable composition, reflecting its storage conditions [137]. It has been demonstrated that the oxide growth on HF-treated silicon in air shows a logarithmic dependence on time with a rate of about 5 $\dot{A}$/decade (albeit initially the oxide formation is hindered and there is a largely varying lag-time that prevents a precise control over oxide thickness) [124]. The slow Psi surface oxidation by "ageing" may be accelerated by either thermal or wet oxidation (known also as chemical/liquid fase oxidation). These methods generate oxides with diverse structures, that are reflected for example,

in the oxide densities: 2.26-2.45 gr/cm^3 in the case of thermal oxide and 1.5 gr/cm^3 when it is formed in DI water (to be compared with 2.33 gr/cm^3 for silicon and 2.65 gr/cm^3 for bulk SiO_2). Also the oxide thickness is different: usually no more than few nm for native oxide and that formed in water, while thicker oxides can be formed by thermal oxidation (100's nm) [138]. Thermal and wet oxidation are widespread methods to obtain a hydrophilic and stable surface, since Si-O bonds strength is considerably greater than that of both Si-Si and Si-H bonds. However, despite the oxide layer enhances the surface stability, the Si-O bonds are susceptible to hydrolysis due to their high polarity.

Psi surface functionalization

Depending on the type of functionalization that has to be performed, both fresh and oxidized layers can be used (see Fig. 2.8).

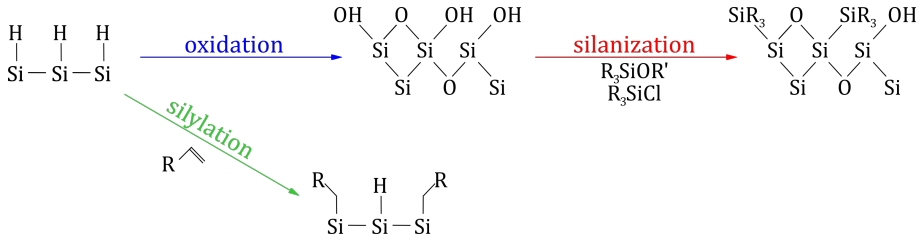

Fig. 2.8: Schematic of oxidation, silanization and silylation reactions: silanization requires oxidized Psi surface, while hydrogen terminated surface is necessary for silylation.

Silanization is used to attach organic species onto the oxide layer: the hydroxy-terminated surface undergoes a condensation reaction with alkoxy- or cloro-silanes to produce new Si-O-Si linkage (as reported in Fig. 2.8). To favour the condensation, the temperature can be increased (e.g. 60°C is used in this thesis).

Silylation consists in the substitution of a hydrogen atom by a silyl group (R_3Si) forming a Si-C bond. Although the Si-C bond strength is lower than Si-O, the non-polar nature of Si-C makes the carbonized surface even more stable. On the other hand this method does not produce a complete and uniform coverage and this fact can compromise the surface stability [139]. Photochemical and thermal promoted silylation have been demonstrated, using both alkenes and alkynes [140–142].

Once the Psi surface has been functionalized, further reactions can be used to impart specific interaction/recognition properties, by adding diverse and more specific chemical groups.

2.1.4 Psi photoluminescence

Photoluminescence (PL) in an indirect gap material such as silicon is a very inefficient mechanism; moreover, since silicon band gap energy is 1.12 eV, the emitted photons will be in the IR region. In nanomaterials the electrons are not free to move in the 3D space as when they are in bulk silicon and due to this spatial confinement, the potential to which the particles (electrons and holes) are subjected can be approximated by a quantum well. The energy of the band gap is inversely proportional to the potential well width [121], so that E_g(c-Si) $< E_g$(Psi); furthermore the smaller nanostructures are characterized by a larger band gap energy (see Fig. 2.9).

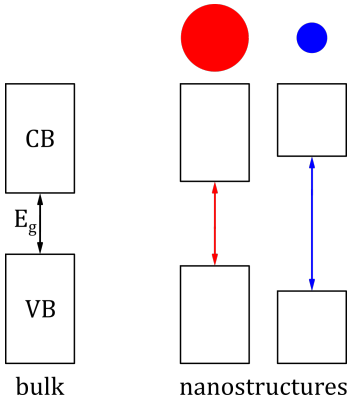

Fig. 2.9: Schematic showing how Psi nanostructures affects PL.

The introduction of non-radiative surface states (silicon dangling bonds) or radiative recombination centres quench the PL; this happens for example when the nanostructures are capped by an oxide layer [137].
Due to its visible PL, Psi became an attractive material in the field of electronics and optoelectronics [133], since an efficiency up to 5% can be reached under UV illumination at room temperature [140]. Electrically excited visible PL has been studied for decades, but no breakthrough has been demonstrated [143]. Actually Psi nanostructures have been reported to be luminescent across the entire UV-VIS and near-IR spectra, although in these cases the origin of these luminescence bands can not be explain with the quantum confinement model. The UV band [144] and the blue-green luminescent emission [145, 146] have been observed only in oxidized silicon nanomaterials and probably arise from contaminated or defective silicon oxide, while the origin of IR emission radiation can be related to dangling bonds, although no direct correlation has yet been demonstrated [147].
The fact the Psi is a photoluminescent material makes it a suitable material for simultaneous imaging and drug delivery to the disease site. It has been demonstrated that, upon proper functionalization, the intrinsic luminescence of Psi is preserved inside the cells, allowing the microparticle tracking without using molecular tags [148].

2.1.5 Psi biocompatibility

When dealing with inorganic materials for biomedical applications, one of the main concerns is related to their possible toxicity. Regarding this issue, Psi offers promising features for biological compatibility, making this material an interesting candidate for DD applications. In aqueous environment, silicon undergoes hydrolysis forming $Si(OH)_4$ (orthosilicic acid), that is the natural bioavailable form of silicon and can be simply excreted via the kidneys [149]. Fresh Psi can produce reactive oxygen species (ROS), which result harmful for healthy biological tissues. However, the ROS generation is an effect related to Psi surface chemistry, therefore a proper surface functionalization can prevent this issue [150]. Studies involving intravenous injection in mice reported that Psi is rapidly removed from the circulatory system [151]; another work demonstrates that Psi microparticles are internalized by human dendritic cells, without showing any toxic effect even at a concentration of 1 mg/mL [148]. Concerning Psi for oral DD applications, it has been demonstrated that Psi particles are stable even in the low pH of the stomach and that do not show any uptake within the intestinal cell layer [152, 153].

2.2 Results on BC release from Psi

2.2.1 Characterization of Psi samples

To study the BC release from Psi, I use two diverse Psi etching conditions, as reported in Tab. 2.1.

Tab. 2.1: Etching conditions used for Psi-A and Psi-B fabrication.

	Psi-A	**Psi-B**
Si wafer (n-type)	0.02 Ωcm	0.01 Ωcm
etching solution	16% HF, 16% H_2O in ETOH	5.5% HF in DI H_2O +1 mL Triton X-100
current density [mA/cm^2]	82	53

The obtained Psi morphologies are shown in Fig. 2.10. In the first case the pores are branched, while the second type of Psi show pores with smoother surfaces. In both cases the pores are not interconnected and their size is much larger than the BC dimensions. Knowing the etching time, from the SEM cross sectional images I obtain the etching rate. In Fig. 2.11 the cross sections of Psi-A etched for 900 sec and Psi-B etched for 350 sec are reported: etching rates are 0.052 and 0.022 μm/sec, respectively. As reported in Sec. 2.1.2, once the Psi layer thickness is known, from the FTIR measurements (see Fig. 2.12) it is possible to estimate the layer refractive index, that is the parameter used in the Bruggeman formula (see Eq. 2.1) to estimate

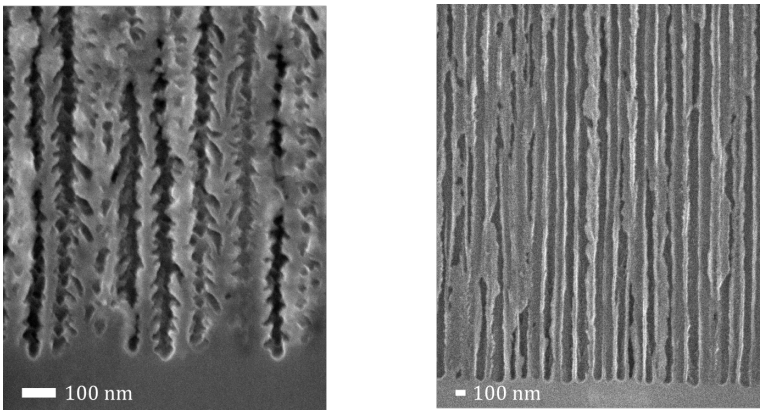

Fig. 2.10: Psi-A (left) and Psi-B (right) SEM cross sectional images that highlight the different pore shapes.

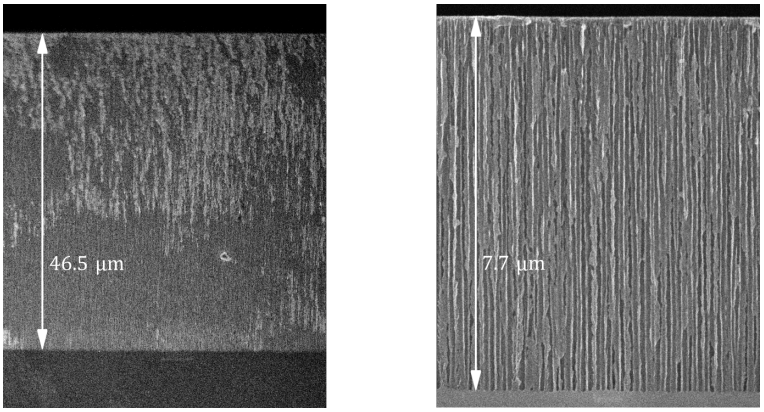

Fig. 2.11: Psi-A (left) and Psi-B (right) SEM cross sectional images.

the porosity. According to Eq. 2.1 and Eq. 2.3, Psi-A has n=2.2 and a porosity of about 45%; while in the case of Psi-B I obtain n=2, that correspond to a porosity of of about 55%.

2.2.2 Psi loaded by immersion method

In some cases, DDSs require the addition of drug during their synthesis (incorporation method), but when dealing with Psi carriers the drug loading is performed after the carrier fabrication (adsorption-absorption method). This process has several advantages such as: the loading can be performed at room temperature, the compounds to be loaded are not exposed to harsh chemical environment, the maximum loading capacity is determined by the Psi carrier porosity and not by stoichiometry or other parameters of the synthesis of the carriers.
Among the adsorption-absorption methods, one distinguishes between immersion and impregnation (also referred as incipient-wetness method). With immersion a known amount of the drug is dissolved in the desired solvent and the carriers are immersed in this solution. After the equilibrium is reached, the loaded carriers are

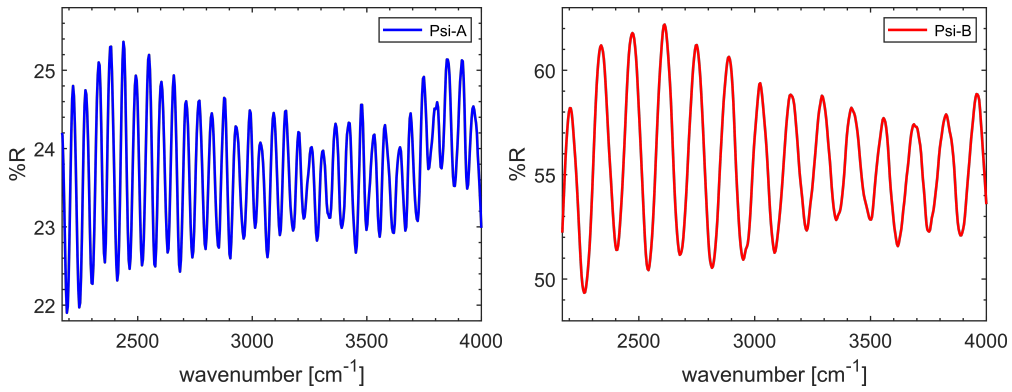

Fig. 2.12: FTIR reflectance spectra for Psi-A (left) etched for 900 sec, that correspond to a layer thickness of 46.5 μm and Psi-B (right) etched for 1200 sec, that correspond to a layer thickness of 26.5 μm; the typical fringes are clearly visible.

separated from the solution. In the impregnation procedure a controlled amount of drug solution is added to the carriers and allowed to infuse through capillary forces into the pores. Drugs are dried within the pores during solvent evaporation [72].
In this section I report the results obtained with the immersion method using Psi-B samples. The empty volume in each Psi chip is about 25 μL, that has been estimated knowing the etched area (A=0.28 cm^2), the layer thickness (h$\simeq$16 μm) and porosity (P$\simeq$55%). I used PSi samples both as-etched ($\mathrm{Psi_{as\text{-}etched}}$) and oxidised ($\mathrm{Psi_{ox}}$) to test if a different surface chemistry (hydrophobic vs hydrophilic) affects the amount of loaded drug. Samples have been thermally oxidised by placing $\mathrm{Psi_{as\text{-}etched}}$ on hot plate at 200° for 4 h and then dipped in H_2O_2 (30% w/w in H_2O) for 24 h. The low temperature stabilization has been chosen to keep the oxidation process compatible with highly porous nanostructures that tend to collapse into bulk silica upon high temperature treatment. The samples are loaded by submerging them in 1.5 mL of BC solutions in tetrahydrofuran (THF) at known concentrations for 24 h (0.32, 0.38, 0.77, 0.88, 1.60, 2.80 and 3.22 mg/mL for $\mathrm{Psi_{as\text{-}etched}}$; 0.32, 0.38, 0.77, 0.88, 1.89, 2.80 and 3.76 mg/mL for $\mathrm{Psi_{ox}}$). The non-porous surface of each chip has been rinsed with THF from the loading solution before placing the sample in 1 mL THF for the BC release. After 30 min, the released solutions have been spectrophotometrically analysed to quantify the amount of BC loaded in each sample (the BC absorption coefficient in THF is ϵ=144000 L·mol^{-1}cm^{-1}). Each experiment have been performed in triplicate.
By knowing both the BC concentration in the loading solutions and the empty volume of the Psi samples, I calculate the amount of BC loaded (neglecting surface adsorption). Fig. 2.13 reports the quantity of BC released as a function of the estimated amount that should have been loaded inside the pore.
Neglecting surface adsorption, the data are expected to be on the bisector (orange line in Fig. 2.13); instead the results show that the released BC is 5 to 20 times larger than the theoretical concentration of BC within pores. The experiments performed on both hydrophilic and hydrophobic surfaces show no macroscopic differences on the

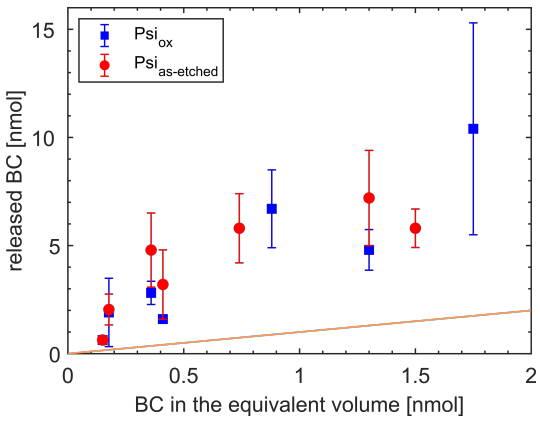

Fig. 2.13: Quantity of released BC vs the estimated BC amount inside the pores: the blue-squares show the release from hydrophilic Psi, whereas the red-circles are the data of hydrophobic PSi. Orange line is the bisector.

amount of BC trapped inside the pores. Furthermore, the standard deviations (SD) of the amount of BC released are very large. The comparison of these results with those reported in the next section (see Sec. 2.2.6 for details), suggests that the large irreproducibility obtained using the immersion methods is due to heterogeneous nucleation (see Appendix for the basic concepts about nucleation).

2.2.3 Psi loaded by impregnation method

The large irreproducibility of the immersion method prevents its use for precise delivery of known amount of drugs, thus I investigate if the impregnation method produces better results.
Unless otherwise specified, the following procedure has been used for all the experiments: soon after the etching, the sample has been loaded with a known volume of BC solution at known concentration in THF. At time t=0 min, the loaded samples are immersed in a cuvette with 3 mL of ethanol (ETOH) with a magnetic stirrer (to mix the solutions and keep the perfect sink conditions). At predetermined time intervals, the entire release volume is spectrophotometrically analysed to quantify the BC concentration (the BC ϵ in ETOH is equal to 144000 L·mol^{-1}cm^{-1}). I normalize the release curves according to the absorbance value of a reference solution obtained by diluting the same amount of the loading solution used to impregnate the Psi samples in 3 mL of ETOH. All release studies are carried out in triplicate.

Release from Psi with different morphologies and thickness

Even if pore size (about 100 nm) is much larger than BC dimensions, rough and smooth pore surfaces might influence the BC released kinetics. To investigate this aspect I fabricate Psi-A and Psi-B with an estimated thickness of 23 μm and 26 μm,

respectively and I load them with 13 μL of 0.3 mg/mL BC in THF.
According to the normalized data reported in Fig. 2.14 (left panel), the different Psi morphologies do not influence the BC released kinetics.
When using Psi layer with pores size in the nanometer range, the loading is not uniform and several BC aggregates form on its surface, as can be seen in Fig. 2.14 (right panel). When dealing with truly nanopores (i.e. <10 nm), extremely diluted loading solutions should be used to minimize the surface crystallization of the drug, yet a very low amount of drug can be loaded in this way.

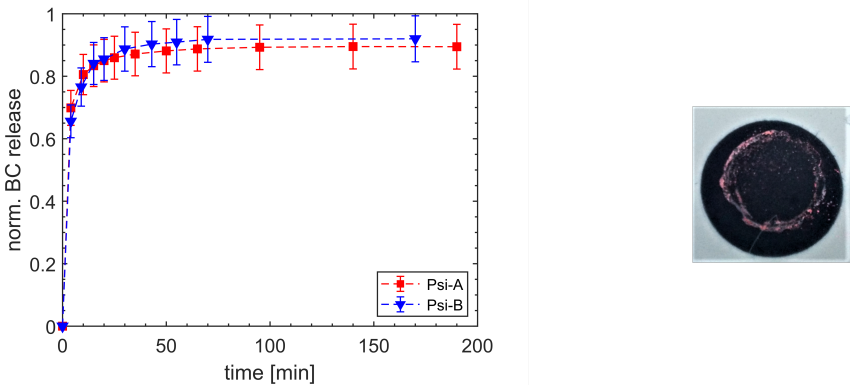

Fig. 2.14: Left panel reports the normalised BC release profiles from Psi-A (red-squares) and Psi-B (blue-triangles); lines are guides to the eyes. Right panel shows a picture of truly nano-Psi, where the macroaggregates at the coffee-stain edge are clearly visible.

Given the similarity of the releases from the two type of Psi, I investigate the relation between the Psi layer thickness and the release kinetics. I fabricate Psi-A with an estimated layer thickness of 46 μm and 23 μm and the samples have been loaded with 13 μL of 0.3 mg/mL BC in THF.
Comparing the released curve obtained (see Fig. 2.15), a significant variation in the BC released rate is observed: by increasing the layer thickness, the saturation is retarded (i.e. at about 50 min using the thinner Psi, at about 100 min with thicker Psi). This fact was expected as the molecules need to diffuse for longer length on the most thick sample, but it suggests that, using this loading condition, BC molecules are adsorbed quite homogeneously along the whole Psi walls.
I fit the data (Psi-A 46 μm, Psi-A 23 μm and Psi-B 26 μm) with both the mechanistic model for slab (see Eq. 1.4) and the empirical 1^{st}-order model (see Eq. 1.13); Fig. 2.16 show the fitted curves and Tab. 2.2 and Tab. 2.3 report the values of the parameters.

I use 50 terms in the summation of the mechanistic model and I verify that the fit accuracy is not limited by such approximation. All parameters (M_{inf}, L, D and k) in both the models are left free during the fitting. Looking at Fig. 2.16 there is no significant difference between the two models. According to Tab. 2.2, L values are very close to the thickness of the samples and the order of magnitude of Ds is the same for liquid in liquid diffusion (10^{-5} cm^2/s), while for high weight

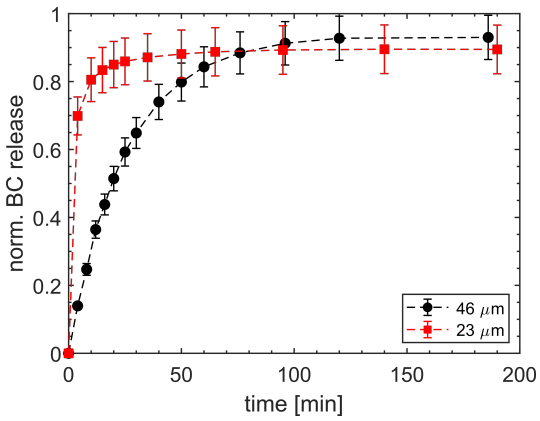

Fig. 2.15: Normalised BC release profiles from Psi-A with different thickness: 46 μm (black-circles) and 23 μm (red-squares); lines are guides to the eyes.

Tab. 2.2: Values of fitting parameters and R^2 obtained using the mechanistic model for slab.

	Psi-A 46 μm	**Psi-A 23 μm**	**Psi-B 26 μm**
M_∞	9.6	8.7	8.9
L [μm]	48	23	24
D [cm^2/s]	$4 \cdot 10^{-6}$	$1 \cdot 10^{-5}$	$8 \cdot 10^{-6}$
R^2	0.984	0.992	0.990

Tab. 2.3: Values of fitting parameters and R^2 obtained using the empirical 1^{st}-order model.

	Psi-A 46 μm	**Psi-A 23 μm**	**Psi-B 26 μm**
M_∞	9.6	8.7	8.9
k [min^{-1}]	0.04	0.4	0.3
R^2	0.999	0.991	0.986

molecules D can be 100 times slower [154]. Even if the fit converges always to the same parameters values (irrespectively from the initial guesses supplied to the algorithm), the prediction intervals obtained for D and L are huge (10^7). On the other hand, the 1^{st}-order model produces much narrower prediction intervals (of few %).

2.2.4 Layer-by-Layer on Psi

The PSi used in this work is characterised by large pores, which allow to load high amount of drug, but there is the need for a strategy to avoid the initial burst release and slow down the release kinetics. For this reason, I try to fabricate a multilayer coating on the porous surface using Layer-By-Layer (LBL) assembly. This method allows to deposit films on the substrate surface through the alternating adsorption of oppositely charged polyelectrolytes from aqueous solutions via electrostatic interactions [155].
In this thesis Poly(diallyldimethylammonium chloride) (PDADMAC) and Poly(sodium 4-styrenesulfonate) (PSS) with average molecular weights of 450 and 1000 kDa

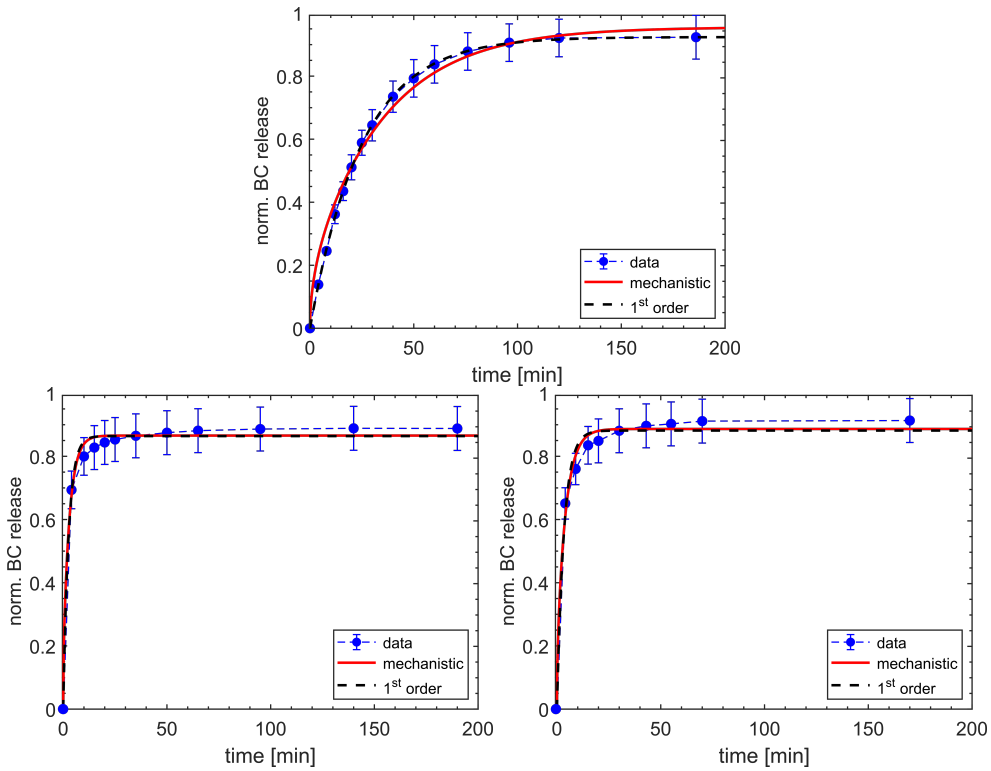

Fig. 2.16: Mechanistic model for slab (red continuous line) and empirical 1^{st}-order model (black-dotted line) are used to fit the normalised BC release form Psi-A 46 μm (upper panel), Psi-A 23 μm (bottom left panel) and Psi-B 26 μm (bottom right panel).

have been chosen as positively and negatively charged strong polyelectrolytes. As an alternative, I use laponite (LAP), a crystalline layered silicate that, when dispersed in water, forms a colloid constituted by nanosized disc-shaped lamellae of about 30 nm in diameter and 1 nm thick. The edge of these platelets is positively charged, while the surfaces are negative [156, 157]. The polyelectrolytes softness opposed to the stiffness of LAP could give rise to different efficiency in pore sealing, reflecting in diverse release kinetics.

ζ-potential analysis on Psi microparticles

In this section I report the ζ-potential measurements performed on Psi microparticles in collaboration with Prof. Alessandra M. Bossi of the Department of Biotechnology of the University of Verona. The obtained ζ-potentials are approximately corrected values, that allow a semi-quantitative comparison among the various samples. For each type of sample, if not otherwise specified, the measurements are performed in triplicate.

Psi microparticles are obtained by grinding the Psi-A chips, followed by ultrasound sonication for few minutes in 1:1=H_2O:ETOH. The particles are left in this solution for some hours to start their oxidation and ease their dispersion in water (as ETOH increase the particle wettability in aqueous solutions). Then they are centrifuged

(about 5000 g for 5 min) and dispersed in 30% H_2O_2 for 24 h to complete the oxidation process. Oxidised microparticles are centrifuged and dispersed in 3 different buffer solutions to verify their charge and stability at different pH. As reported in Tab. 2.4 oxidised particles are negatively charged and their ζ-potential modulus is sufficiently large to consider them as stable suspensions and to allow the deposition of the first polymeric layer.

Tab. 2.4: ζ-potential values for oxidised microparticles at different pH.

Buffer	ζ-potential [mV]
buffer ph 4,7 (sodium acetate)	-22±2
buffer ph 7,4 (TRIS-acetate)	-27±2
buffer ph 9.8 (CAPSO)	-33±2

To create the first positive layer, the oxidised Psi particles are immersed in a PDADMAC solution at pH=7 and placed for 30 min on a shaker. I prepared various samples that differ for Psi and PDADMAC concentrations; moreover I deposit the layers with and without NaCl (0.5 M), since it has been reported that the presence of NaCl increases both film thickness and its surface roughness [158, 159]. Details about sample preparation conditions are shown in Tab. 2.5.

Tab. 2.5: Sample preparation conditions used to deposit the PDADMAC layer on oxidised microparticles and the corresponding average ζ-potential values and SD.

Psi 1.25 mg/mL		Psi 0.16 mg/mL	
PDADMAC (mg/mL)	ζ-potential (mV)	PDADMAC (mg/mL)	ζ-potential (mV)
5	31±2	5	32±3
1	28±2	1	32±2
5 with NaCl	32±2	5 with NaCl	31±2
1 with NaCl	30±2	1 with NaCl	27±2

After 3 rinses, the microparticles are dispersed in water. I dilute the PSi 1.25 mg/mL suspensions to reach about the same concentration of the more dilute one (Psi 0.16 mg/mL), to have similar scattering from all solutions. The rinsing efficiency is confirmed by conductivity measurements (0.030 ± 0.003 mS/cm in oxidised Psi-A and 0.027 ± 0.005 mS/cm in Psi-PDADMAC). According to the ζ-potential averages reported in Tab. 2.5, it is evident that the first positive layer has been formed on Psi microparticles, but no significant difference emerges when comparing the different fabrication conditions. For further analysis I choose 0.16 mg/mL of Psi-A and 1 mg/mL of PDADMC.

Before depositing the second layer, I investigate the Psi-PDADMAC microparticles stability in various buffers (see Tab. 2.6): the ζ-potentials remain positive at different pH and their moduli are slightly larger than those of naked oxidised powders.

Tab. 2.6: ζ-potential values for PDADMAC-particles at different pH.

Buffer	ζ-potential [mV]
buffer ph 4,7 (sodium acetate)	38±2
buffer ph 7,4 (TRIS-acetate)	32±2
buffer ph 9.8 (CAPSO)	26±2

To deposit the second negative layer, the PDADMAC-particles are suspended in buffer at pH=7 with either LAP or PSS and placed for 30 min on a shaker. The tested LAP concentrations are 0.5, 1 and 5 mg/mL, while in case of PSS I use 1 and 5 mg/mL. After 3 rinses, the microparticles are dispersed in water; the measured ζ-potentials are reported in Tab. 2.7 and Tab. 2.8 together with the number of tested samples. The fact that the ζ-potentials of microparticles dispersed in LAP suspensions are positive, indicates that the second layer does not formed. Concerning the PSS layer, negative ζ-potentials have been obtained only in 9 out of 15 samples. Given the poor reproducibility of the PSS second layer (LBL formation occurs only in 60% of the attempts), I do not proceed for subsequent layers.

Tab. 2.7: Sample preparation conditions used to deposit the LAP layer on PDADMAC-particles, number of tested samples, corresponding average ζ-potential values and SD.

LAP concentration (mg/mL)	N° of tested samples	ζ-potential [mV]
0.5	3	7±1
1	3	34±4
5	6	26±4

Tab. 2.8: Sample preparation conditions used to deposit the PSS layer on PDADMAC-particles with the ζ-potential values obtained for each sample.

PSS concentration (mg/mL)	ζ-potential [mV]
1 mg/mL	-3.57 -3.51 -2.21 15.7 19.9 21.4
5 mg/mL	-21.8 -21.2 -20.9 -20.9 -20.3 -19.4 14.7 16.6 17.9

Release from Psi covered with LBL

To study the effectiveness of PDADMAC-PSS LBL in tuning drug release, I use oxidised Psi-A samples 45 μm in thickness. Each Psi_{ox} has been loaded with 20 μL

of 0.3 mg/mL BC in THF; the BC used for experiments reported in this section has ϵ=100000 L·mol^{-1}cm^{-1} (this reduced value is due to a partial degradation of the BC: see Sec. 2.2.7 for a detailed discussion about how it affects the release from Psi). After the loading the Psi_{ox} samples have been subjected to either of the following procedures:

- they are immediately placed in ETOH to monitor the BC release;
- they are placed in a PDADMAC solution (5 mg/mL in buffer at pH=7) for 30 min and then (after the rinsing in DI H_2O) in a PSS solution (5 mg/mL in buffer at pH=7) for 30 min. Before monitoring the BC release, the samples are rinsed in DI H_2O (denoted as PSi_{LBL}).

The normalized release curves are reported in Fig. 2.17.

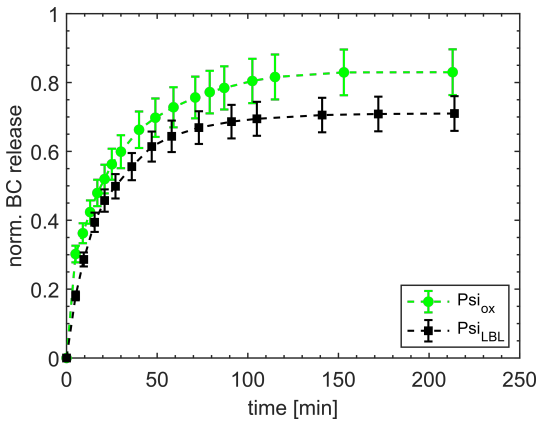

Fig. 2.17: Normalised BC release profiles from PSi_{ox} (green-circles) and PSi_{LBL} (black-squares); lines are guides to the eyes.

The amount of BC molecules released from PSi_{ox} is 80% of the loaded BC, while that released from PSi_{LBL} is about 70%. The lower amount of BC spectrophotometrically detected in the release media of PSi_{LBL}, can be due to the fact that, once loaded, these chips have been placed in H_2O that can partially oxidised the BC in the pores, thus reducing its absorbance (as reported in Appendix). To verify this hypothesis, I immerse the loaded PSi samples in H_2O for 1 h (denoted as PSi_{aq}) before monitoring the BC release. The data reported in Fig. 2.18 confirm the hypothesis, since the amount of BC released is about 70%.

2.2.5 Formation of BC aggregates on Psi surface during the release in ETOH

Although in the previous experiments Psi samples have been loaded with small amount of BC (few nanomoles), Psi is well known for its high loading capacity.

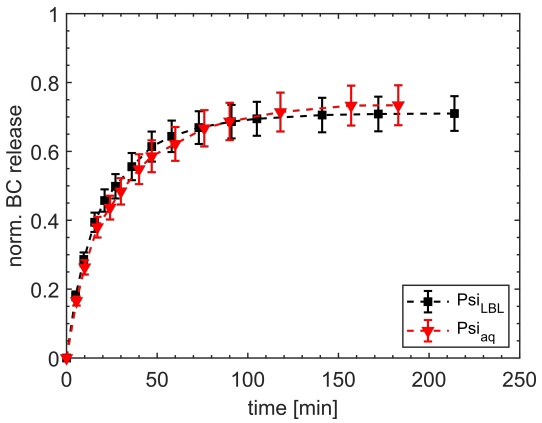

Fig. 2.18: Normalised BC release profiles from PSi_{LBL} (black-squares) and PSi_{aq} (red-triangles); lines are guides to the eyes.

When I try to increase the quantity of molecules loaded, I observe that, during the release, BC forms aggregates on Psi surface giving rise to unreproducible experiments. For this reason I investigate how loading conditions, surface chemistry and BC extent of degradation affect the BC heterogeneous nucleation (see Appendix for the basic concepts about nucleation). The Psi samples used for the following experiments are Psi-A, 45 μm thick.

Aggregates formation dependence on BC concentration in the loading solution

To load the as-etched Psi samples I prepare THF solutions of BC at different concentrations: 1.5, 0.3 and 0.17 mg/mL. Psi samples are impregnated with diverse volumes of these solutions, so that different amounts of BC are loaded, as reported in Tab. 2.9.

Tab. 2.9: Amount of BC loaded in Psi samples using loading solutions with different BC concentrations.

loading solution [mg/mL]	**loaded BC [μg]**			
1.5	3.8	7.5	10.5	
0.3	3.8	7.5	10.5	12
0.17		6.8	10.2	13.6

The porous chips are immersed in ETOH to monitor the BC release and during the first few minutes of the release (about 3-15 min) in some of the samples I observe the formation of BC macroscopic aggregates on the Psi surface (an example is shown in Fig. 2.19, where the arrows point to the BC aggregates).

To note that during the loading such aggregates are not visible; moreover, in all the experiments the release media are well stirred and the BC final concentrations are much lower than the BC solubility in ETOH (i.e. when loading 3.8 or 13.6 μg, the BC final concentrations are about 23 and 6 times lower than BC solubility [160]).

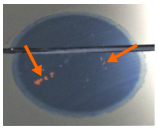

Fig. 2.19: During the first few minutes of the release in ETOH, BC aggregates are clearly visible on the surface of some Psi samples.

In Tab. 2.9, the loading conditions at which the aggregates are clearly visible on the Psi surface are highlighted: by decreasing the BC concentration of the loading solutions, larger amount of drug can be loaded without aggregates formation during the release. Kinetics of BC release are reported in Fig. 2.20 and looking at these data, the following considerations can be done:

- when no macroaggregates are visible, about 90% of the loaded BC is released and the SD among different release experiments are less than 10% ;
- if macroaggregates form, only 40 to 60% of the loaded BC is released and the SD increase substantially, up to about 30%.

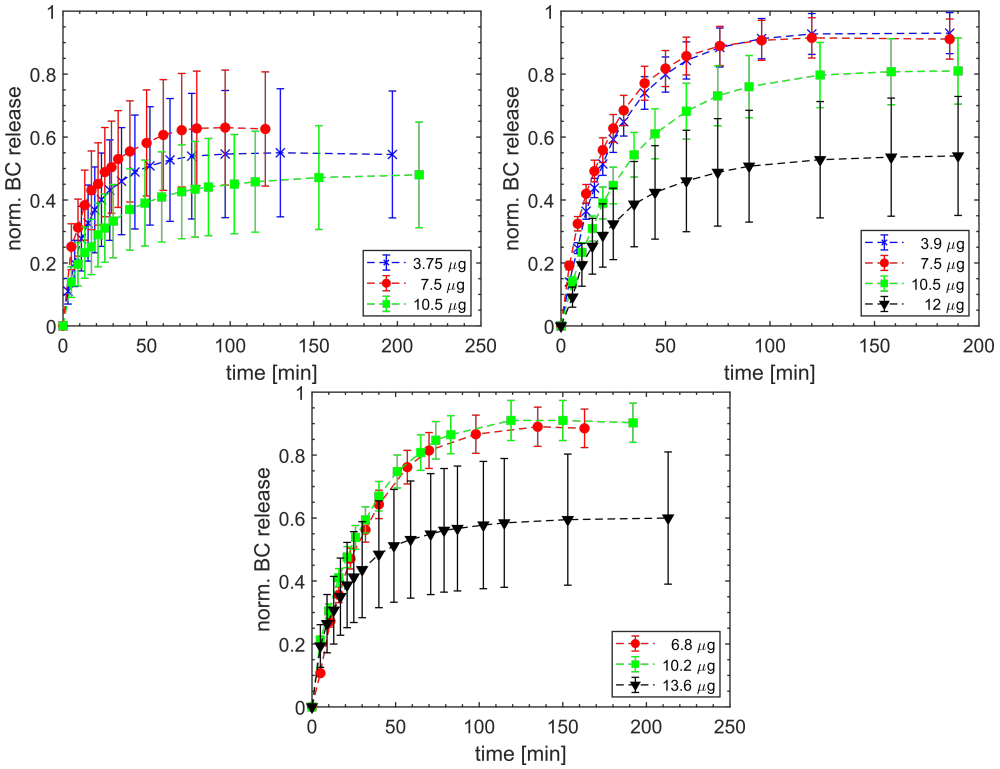

Fig. 2.20: Normalised BC release profiles from PSi loaded with different amount of BC using loading solutions with BC concentrations of 1.5 mg/mL (upper left panel), 0.3 mg/mL (upper right panel) and 0.17 mg/mL (bottom panel): (about 4 μg blue-crosses, 8 μg red-circles, 10 μg green-squares and 13 μg black-triangles); lines are guides to the eyes.

To note that the solubility of these macroaggregates is extremely slow and variable: they need from 24 h up to 35 h to completely dissolve.

The experimental outcomes can be interpreted by assuming the poor reproducibility to be due to heterogeneous nucleation, that produces a broad distribution of aggregates reflected into broader release kinetics and increased SD.
To quantify this effect I define the figure-of-merit (FOM) as the ratio between the normalised released BC and the SD: loading conditions for which the BC release is nearly complete and reproducible give rise to high FOM. According to the data reported in Fig. 2.21, it is evident that the aggregates formation does not depend only on the amount of BC loaded, but also on the BC concentration of the loading solution. In fact, aggregates are clearly visible when only 3.8 μg of BC are loaded using 1.5 mg/mL, while if I use 0.3 mg/mL their formation is evident when I load at least 12 μg of BC. The samples loaded with 10.5 μg of BC using the 0.3 mg/mL solution have a FOM$\simeq$8 and do not form macroaggregates, however they release slightly less BC, compared to the samples loaded with smaller BC amount (about 80% vs 90%) and its SD is a bit larger. Qualitatively, 10.5 μg might be the limiting amount of BC that can be loaded using a 0.3 mg/mL solution without macroaggregates formation.

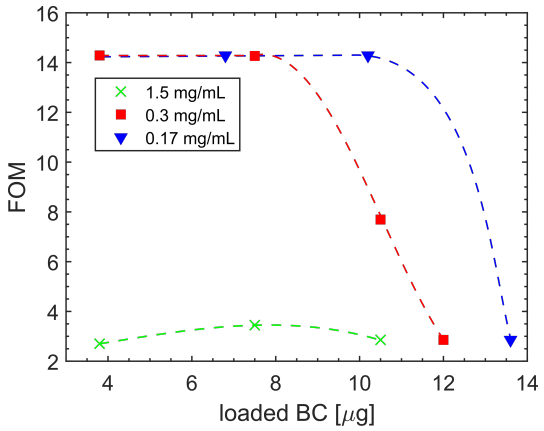

Fig. 2.21: F.O.M as a function of the amount of loaded BC. When using the 1.5 mg/mL loading solution (green-crosses) the F.O.M assumes always low values, irrespectively on the amount of BC loaded; on the other hand when the more diluted loading solutions are used (red-squares and blue-triangles), F.O.M values are high for low amount of BC loaded and decrease for greater BC quantities. Lines are guides to the eyes.

If the release is performed in a much better solvent, such as THF (using the same loading conditions), aggregates do not form and all the Psi samples released about 90% of the loaded BC (but in this case BC release is too fast to be monitored).
The results of this section demonstrate that, although the BC final concentrations in ETOH are below its solubility limit, some loading conditions favour the occurrence of supersaturated BC regions (both inside the pores and at pore openings) in which heterogeneous nucleation occurs.

Aggregates formation dependence on PSi surface chemistry

To investigate if there is a relationship between the aggregates formation and the Psi surface chemistry, I compare the results obtained loading $Psi_{as\text{-}etched}$ and Psi_{ox} with 7.5 and 12 μg of BC using a loading solution of 0.3 mg/mL. Since $Psi_{as\text{-}etched}$ has hydrophobic surface, while that of Psi_{ox} is hydrophilic, different interactions between the BC molecules and the Psi surface are expected. According to the data shown in Fig. 2.22 there is no significant difference: when 7.5 μg of BC are loaded both Psi samples release almost all the molecules, while by increasing the BC amount, aggregates form.

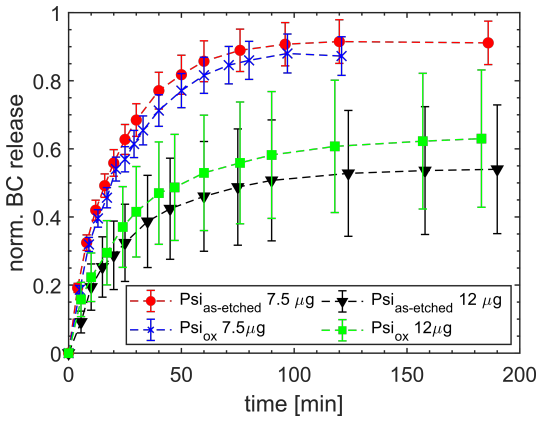

Fig. 2.22: Normalised BC release profiles from PSi with either hydrophilic or hydrophobic surfaces loaded with different amount of BC (7.5 and 12 μg) using 0.3 mg/mL loading solution; lines are guides to the eyes.

These experiments suggest that the BC nucleation-aggregation phenomenon on Psi is mainly ruled by the surface energy due to the surface nanostructuring while it is weakly related to the substrate surface chemistry.

Aggregates formation at the coffee-stain edges on bulk-Si

As a reference I perform a similar experiment by dropping a BC solution on a bulk-Si sample: the coffee-stain effect leads to BC macroaggregates formation at the drop edge. Although these aggregates seem very similar to that formed on Psi surface during the release, the dynamics of dissolution demonstrate that the two aggregation processes are different.

I create coffee-stain induced BC macroaggregates by dropping 20 μL of 1.5 mg/mL BC solution in THF (4 drops of 5 μL each one). After solvent evaporation, I monitor the BC dissolution in ETOH and the normalized data are reported in Fig. 2.23.

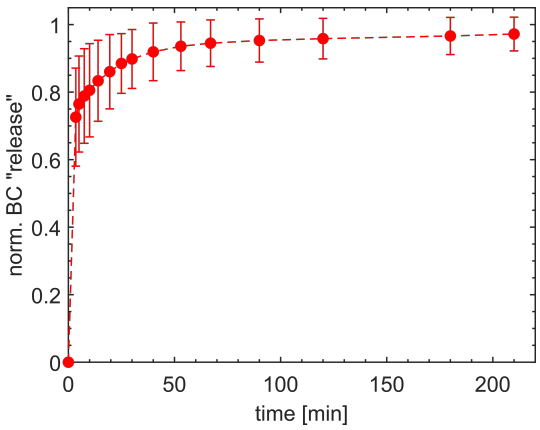

Fig. 2.23: Normalised BC dissolution profiles from bulk-Si; lines are guides to the eyes.

BC is quantitatively dissolved in ETOH in less than 100 min. At the beginning the SD are high, since diverse BC depositions give rise to BC aggregates with various dimensions, which dissolve with different kinetics; but, at the end of the dissolution, the variations in the amount of BC dissolved are small. I try to investigate the different structure of these two type of macroaggregates by x-ray diffraction, unfortunately the sensitivity of the instruments are not enough to collect a detectable signal from BC crystals/amorphous aggregates.

Aggregates formation dependence on BC degradation extent

The fact that the dissolution of aggregates formed either during the release from Psi or by the coffee-stain phenomenon on bulk-Si is different suggests to investigate if the state of BC oxidation might have a role in the formation of different polymorphs that dissolve at different rates.
I used BC with ϵ=70000 L·mol^{-1}cm^{-1} and I load as-etched Psi with 40 μg or 35 μg using either 2 mg/mL or 3.5 mg/mL BC solution. Both experiments have been performed in 5 mL of ETOH, to be far from the limit of BC solubility in ETOH: once all the molecules have been released, the BC concentration is about 4 times lower than its solubility (0.03 mg/mL). The normalised release curves are reported in Fig. 2.24. When BC 3.5 mg/mL is used, I observe the aggregates formation on the porous surface during the molecule release, the decrease in the released BC percentage (about 35% of the loaded BC) and the increase in the SD. On the other hand, using the 2 mg/mL solution, no aggregates form, the released BC is about 70% of the loaded one and the SD are less than 10%. The small SD obtained, lead to exclude that the lower release percentage is due to the aggregates formation. The reduced BC released might be due to partial degradation of the drug as described in Sec. 2.2.7.

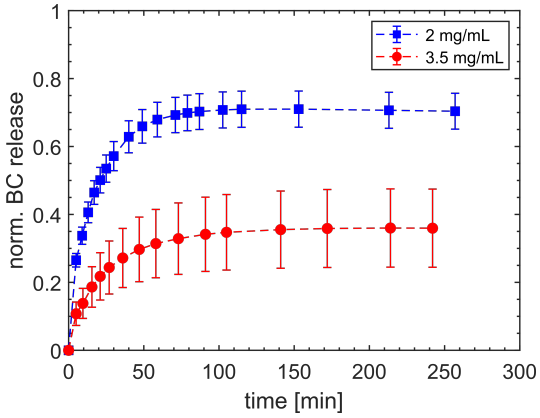

Fig. 2.24: Normalised BC release profiles from Psi loaded with degraded BC using loading solutions of 2 mg/mL (blue-squares) and 3.5 mg/mL (red-circles); lines are guides to the eyes.

According to these data, when using degraded BC, the formation of macroaggregates requires larger BC concentration in the loading solution than when non-degraded BC is used. This is probably related to the presence of oxidised functional groups on a substantial fraction of BC, which hinder its crystallization on the Psi surface (probably due to the fact that the oxidised BC molecules are more hydrophilic).

2.2.6 Comparison between immersion and impregnation method

By comparing the results between immersion and impregnation method, I note a fundamental difference: assuming that the Psi, loaded using the immersion method, releases the BC quantitatively (as the release has been performed in THF), I compare it with the impregnation experiment with similar amount of BC loaded.
In average the samples loaded with the immersion method release about 5 nmol of BC and the SD average value is 30%. With the impregnation method, I can load more than 5 nmol without forming aggregate and obtaining SD less than 10% (e.g. sample loaded with 3.8 mg using 0.3 mg/mL). This comparison suggests that the high SDs obtained in most of the immersion experiments are due to aggregates formed inside the pores, even if BC is loaded at concentrations lower than its solubility in THF (10 mg/mL). The long time given to BC to arrange under equilibrium condition can account for the aggregates formation. Since large SD are present only in immersion experiments, they cannot be ascribed to non-specific absorption, otherwise I should see similar SDs from impregnation releases, too.

2.2.7 Release from Psi with different surface chemistry

The extreme hydrophobicity of BC is of interest to understand how it interacts with either hydrophilic and hydrophibic surfaces. Thus, I fabricate a set of Psi-A samples (45 μm in thickness), some of them are used as-etched to test a hydrophobic surface, while others are oxidized, using different receipts, to obtain hydrophilic surfaces:

1. PSi_{th} (thermal oxidation): the $Psi_{as\text{-}etched}$ have been placed on hot plate at 200° for 4 h;

2. PSi_{APTES} (thermal oxidation + APTES functionalization): after the thermal oxidation, the Psi have been immersed in (3-Aminopropyl)triethoxysilane (APTES) solution (1:100=APTES:toluene) on hot plate at 60° for 15 min.

3. $PSi_{H_2O_2}$ (thermal + wet oxidation): after the thermal oxidation, the Psi have been placed in H_2O_2 (30% w/w in H_2O) for 24 h;

I rinse the oxidised/functionalized PSi with ETOH, before loading them with 20 μL of 0.3 mg/mL of BC solution in THF. The release kinetics have been monitored by immersing the loaded samples in ETOH. Fig. 2.25A reports the normalized release data, while Fig. 2.25B show typical BC absorption spectra, acquired at the end of the release.

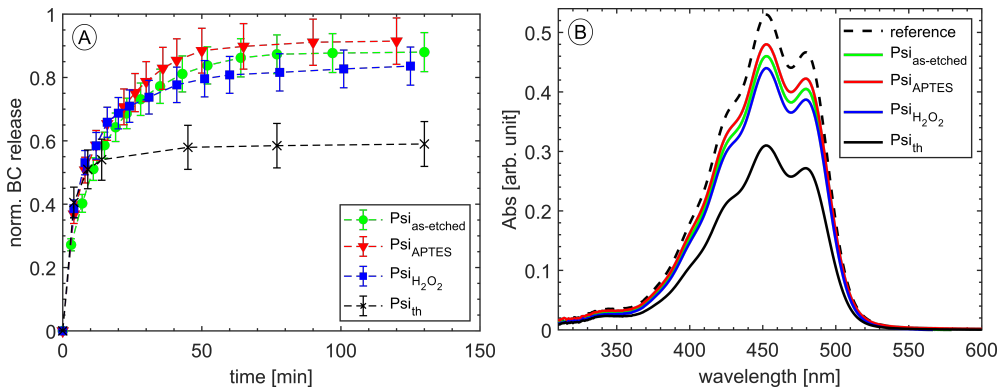

Fig. 2.25: A) Normalised BC release profiles from $PSi_{as\text{-}etched}$ (green-circles), PSi_{APTES} (red-triangles), $PSi_{H_2O_2}$ (blue-squares) and PSi_{th} (black-crosses); lines are guides to the eyes. B) BC typical absorption spectra, acquired at the end of the release from the different Psi samples (continuous lines) and reference BC spectrum (black dotted line).

To note that:

- PSi_{th} is the sample that release the smaller amount of BC (less than 60% of the loaded one), while all the other samples release nearly completely the loaded molecules; the small SD (about 10%) allows to exclude that the observed

decrease in the release for the PSi_{th} is due to aggregates formation on Psi surface.

- the UV tails of the spectra do not increase on samples with smaller released amount of BC (see Fig.2.25B), suggesting that the π-coniugated structure of a single BC molecule is not broken locally (e.g. by insertion of a single functional group), otherwise absorbance spectra would shift as predicted by the empirical Fieser-Kuhn rules for conjugated polyenes [161].

I try to recover the BC retained within the pores by immersing the PSi_{th} (after the release) in THF and by disintegrating the porous layer using an ultrasonic treatment; Psi micropartcicles are removed from the surnatant through a centrifuging (about 7000 g for 5 min). In the absorption spectrum of the surnatant there is no signal in the BC region. This fact suggests that the 40% of the loaded BC in PSi_{th} has been somehow degraded.
To understand whether the degraded BC molecules remain inside the porous layer (adsorbed or chemically bound) or are released in the solvent, I can not relay on spectrophotometic measurements, because the degraded BC molecules do not absorb visible light. For this reason I perform NMR analyses, using stabilized $CDCl_3$ as solvent for both loading solution and release media. I load 6 $Psi_{as\text{-}etched}$ and 6 Psi_{th} with 10 μL of BC (1.5 mg/mL) in $CDCl_3$, the release media obtained from these two sets of samples have been concentrated to a final volume of 630 μL to increase the molecules concentration to obtain a good S/N ratio in the NMR measurements. The acquired data are reported in Fig. 2.26.

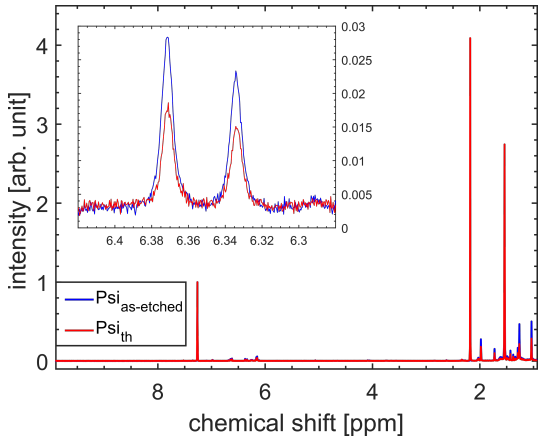

Fig. 2.26: NMR spectra of BC released from $Psi_{as\text{-}etched}$ (blue line) and Psi_{th} (red line), normalized to the $CHCl_3$ peak. The inset shows a zoom of the peaks at 6.33 and 6.37 ppm, used to quantify BC.

Both spectra show the typical, sharp peaks of molecular BC and there is no evidence of BC degradation (e.g peak broadening or peaks related to oxidised species), suggesting that no BC-polymer is present in the release media. However, the NMR signals of BC released from Psi_{th} have a significantly reduced intensity with respect

to those of BC released from $Psi_{as\text{-}etched}$. The two peaks at 6.33 and 6.37 ppm (due to protons bound to C12) can be used to estimate the difference in the amount of BC present in the two media by calculating their integral ratio: setting the value of the integral for the BC released from $Psi_{as\text{-}etched}$ to 100%, the integral of the BC released from Psi_{th} is 63%. This value is very similar with the one obtained from spectroscopic measurements (as shown in Fig. 2.25). Thus I conclude that Psi_{th} heavily degrades the BC and it keeps the oxidized molecules inside the porous layer (either adsorbed or chemically bound).
I try to get clues from the defects sensitivity to light by comparing samples which are kept in the dark, under ambient light and more energetic radiation (UV light). I load Psi_{th} with 20 μL of 0.3 mg/mL of BC solution in THF and I store the samples for 2 h either in the dark or under ambient light: the samples release 40%$\pm$6% and 43%$\pm$7% of the loaded BC, respectively. These values are lower than those obtained when the release is performed immediately after the loading, suggesting that even 2 h of storage in Psi_{th} substantially degrades BC and that visible light does not influence the result. I do not perform the same experiments under UV light, since I observe a very fast degradation of BC powder under this radiation (by illuminating the BC powder for 1.5 h with a UV-LED light at 160 mW/cm^2 I obtain ϵ=135000 L·mol^{-1}cm^{-1}, while after 2 h in ambient light ϵ is still equal to 144000 L·mol^{-1}cm^{-1}). To test if UV light induces defects able to interact with BC, I illuminate Psi_{th} with UV light for 2 h, then I load the sample with 20 μL of 0.3 mg/mL of BC solution in THF and I perform the release in THF. The released BC is 55%$\pm$7% of the loaded one, so that the UV light irradiation does not have any significant effect on BC degradation.

In the following experiments I compare the results obtained loading both $Psi_{as\text{-}etched}$ and Psi_{th} with BC characterised by different degradation extent (ϵ=140000, 100000 and 70000 L·mol^{-1}cm^{-1}). I load the porous layers with 20 μL of 0.3 mg/mL BC in THF and I acquire the spectra at the end of the release. The data reported in Fig. 2.27 show that when the Psi samples are loaded with degraded BC, the release percentage is smaller than that obtained for non-degraded BC: the lower is the BC ϵ, the more Psi degrades the BC molecules (both $Psi_{as\text{-}etched}$ and Psi_{th}). This fact, despite it is not a proof, suggests that BC degradation that occurs inside Psi might be due to radical reactions.

2.2.8 Storage of BC in Psi

Although Psi_{th} fastens the degradation of partially oxidized BC (as it decreases the ϵ of degraded BC in less than 2 h, the duration of a release experiment), when stabilised Psi is loaded with non-degraded BC, its release is almost quantitative. Considering the fact that Psi is opaque I think it might work as a protective carrier

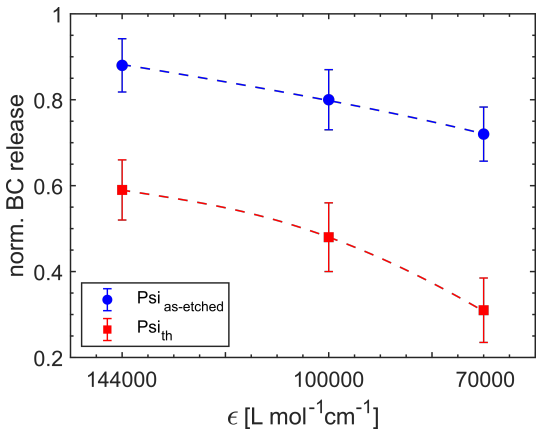

Fig. 2.27: Amount of BC released (normalized to the reference solution) from $Psi_{as\text{-}etched}$ (blue-circles) and Psi_{th} (red-squares) as a function of the loaded BC ϵ; lines are guides to the eyes.

for drug molecules. Furthermore, when Psi surface is covered by hydrogen it is easily oxidized, thus (despite it is not suitable to protect drugs that can be reduced, as reported in [162]) $Psi_{as\text{-}etched}$ might be used as a sacrificial material to prevent molecule oxidation.

To test these hypotheses I compared BC degradation of BC powder left in air, in THF and loaded within Psi samples. A 0.3 mg/mL BC solution in THF has been prepared to impregnate both $Psi_{as\text{-}etched}$ and Psi_{APTES} with 10 μL. I keep the BC powder, the loading solution and the loaded samples in the dark at room temperature for 2 weeks. After 15 days, I prepare a 0.3 mg/mL BC solution in THF using BC stored in air and I estimate an ϵ of about 117000 L·mol^{-1}cm^{-1}. BC degradation is even more consistent for BC stored in THF that has ϵ=77000 L·mol^{-1}cm^{-1}. Finally I perform the BC release from the loaded Psi chips in THF: the amount of BC released from $Psi_{as\text{-}etched}$ and Psi_{APTES} is 15%±4% and 40%±7% of the loaded one, respectively. The absorbance SDs are small, suggesting that no aggregates are formed, thus the decrease in absorbance is due to BC degradation.

These experiments highlight that Psi, even if its surface has been properly stabilized, degrades delicate molecules. In particular the stability of the drugs has to be evaluated on a reasonably long time scale, as the degradation reactions can be rather slow.

3 Nanocellulose

3.1 Introduction to nanocellulose

In recent years, the demand for products made from renewable and sustainable resources increases the interest for cellulose-based materials. Cellulose is the most abundant organic polymer on Earth; it is mainly present inside the plant cell walls, but it is also secreted by tunicates (sea animals) and it can be found in some algae and bacteria. This material is renewable, biodegradable as well as non-toxic; furthermore it is highly sustainable since the traditional cellulose industry produces a large quantity of cellulose wastes. Cellulose has been used for millennia in the form of wood and plant fibres for building materials and for clothing. Recently, a deeper knowledge of its properties and the ability to modify some of its characteristics (e.g. functionalizing it to obtain high added value derivatives) enable to create cellulose-based materials for coatings, membranes, pharmaceuticals and foodstuff. Moreover, there is an explosive interest in isolating cellulosic materials with one dimension in the nanometer range, since they combine important cellulose features with the specific characteristics of nanoscale materials, such as: impressive mechanical properties, tunable wettability, broad chemical modification capacity and reinforcing capability.

3.1.1 Cellulose structure

Structurally, cellulose is a high molecular weight polysaccharide, constituted by the linear repetition of anhydroglucose rings covalently linked together between the oxygen bonded to C1 of one glucose and C4 of the adjoint ring (the so called glycosidic bond), as shown in Fig. 3.1. Two anhydroglucose rings linked together by glycosidic bond are called cellobiose and it is considered the unit of the cellulose chain. Its chemical formula is $(C_6H_{10}O_5)_n$, where the number of repeated units (n) is in the range 10000-15000 [163], depending on the cellulose source material. The two rings forming the cellobiose do not lie exactly in the plane of the structure: they have a chair conformation with adjoining glucose molecules rotated through an angle of 180° about the molecular axis and hydroxyl groups are in an equatorial position. In nature, cellulose is a material with a hierarchical structure: it is found as assemblies of single cellulose chain, forming fibres, that are brought together

through intra- and inter- molecular hydrogen bonds among the hydroxyl groups and Van der Waals forces (see Fig. 3.2).

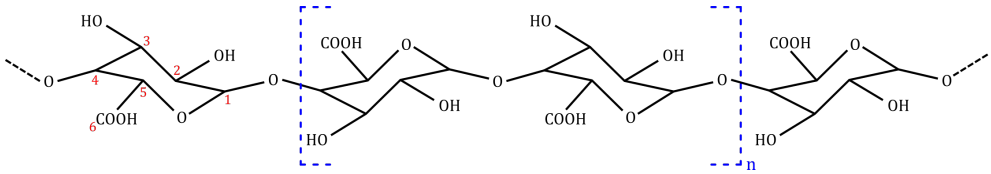

Fig. 3.1: Schematic of a single cellulose chain, showing the fundamental unit.

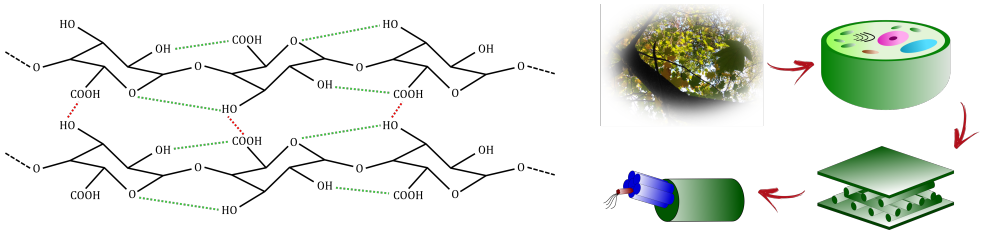

Fig. 3.2: Left panel shows the intra- (green lines) and inter- (red lines) chains hydrogen bonding pattern in cellulose; right panel reports the schematic of the cellulose structure, from leaves to molecules.

3.1.2 Cellulose biosynthesis

The multi-step process to synthesise cellulose is highly dependent on the source considered; generally, inside the vegetable cell walls there are the so called terminal enzyme complexes (TECs), from which cellulose is extruded. Each TEC is composed of identical subunits and every subunit contains multiple catalytic sites. The resulting cellulose fibril structure is strongly dependent on the catalytic sites, subunits and TECs configurations. For cellulose produced by trees, each TEC is constituted by 6 subunits organized into six-membered rosettes and each subunit contains 6 catalytic sites. Each catalytic site polymerizes a single chain of cellulose and the first step of cellulose crystallization is the formation of a "mini-sheet" by self-assembling the 6 cellulose chains; then the 6 "mini-sheets" extruded by the subunits are self-assembled in the so called "elementary fibril". The elementary fibril produced by each TEC is constituted by 36 cellulose chains and it has a square cross section 3-5 nm in size. Along a fibril there highly crystalline regions and amorphous domains with strikingly different properties (see Fig.3.3, left panel). The elementary fibrils produced by 6 TECs are further assembled into the so called microfibril and a bundle of microfibrils constitute the cellulose fibre (see Fig.3.3, right panel) [164–166].

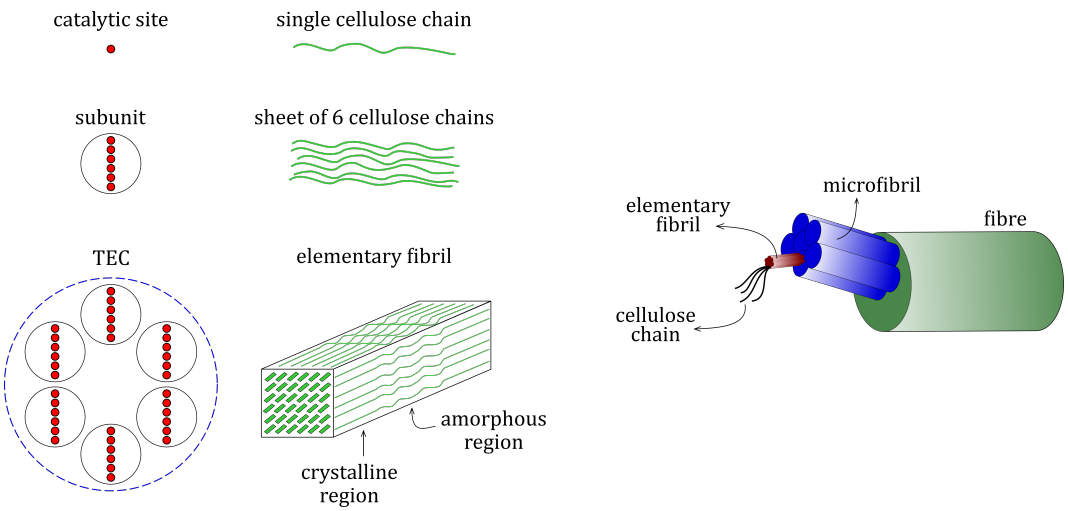

Fig. 3.3: Left panel reports the schematic of the steps that lead to wood elementary fibril synthesis; right panel shows the schematic of the cellulose fibre hierarchical structure.

3.1.3 Crystalline cellulose

Crystalline cellulose produced in nature is called Cellulose I or "natural cellulose". It can be found in two polymorphs: a triclinic (I_a) and a monoclinic structure (I_b), that coexist in diverse proportions depending on the cellulose source [163, 167, 168]. Since Cellulose I has a structure that is thermodynamically metastable, it can be converted in other polymorphs of technical relevance [167].
To date, the most accurate I_a and I_b lattice structures characterization has been provided by Nishiyama and co-workers [169, 170]. The crystal structures of I_a and I_b are reported in Fig. 3.4. When viewed along the cellulose chain axis, the I_a and I_b show a nearly identical molecular arrangement and their unit cells have a parallelogram shape (Fig. 3.4 A and B). The main difference between the two polymorphs can be seen by looking along the direction indicated by the orange arrow in Fig. 3.4 A and B. I_a and I_b show a different relative displacement of cellulose sheets: for I_a there is a relative displacement of c/4 between each subsequent sheet (Fig. C), while for I_b the displacement alternates between c/4 and -c/4 (Fig. D)[170, 171]. I_a and I_b share the so called "parallel up" configuration, meaning that all cellulose chains are arranged in the positive c-axis direction of the unit cell, in such a way that the C1→C4 link points in that direction [164].

3.1.4 Cellulose particle extraction

The isolation of cellulose micro and nanocomponents from the various cellulose source materials is a two steps process. First of all the source material should be purified and homogenized; depending on the cellulose origin different pretreatment methods are adopted. As an example, when dealing with wood and plant cellulose,

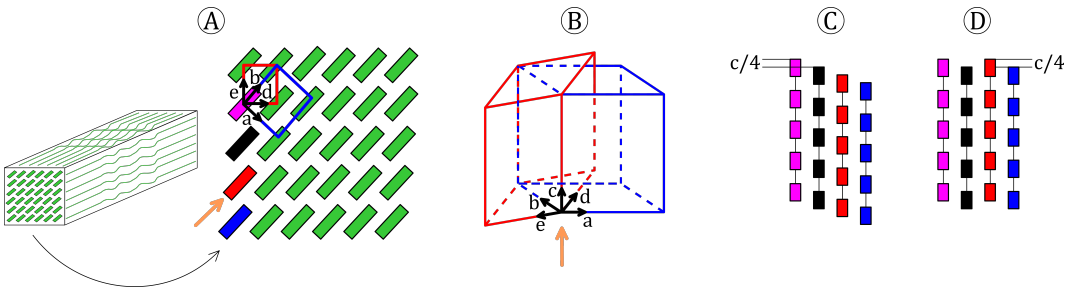

Fig. 3.4: A) Cellulose I crystal and its cross sectional view; superimposed on the Cellulose I lattice there are I_a and I_b unit cells, both with a parallelogram shape when looking down along the chain direction (adapted from [172]). B) relative configuration of I_a with respect to I_b unit cell, when viewed along the direction indicated by the orange arrow in Fig. A (adapted from [171]). C and D) the displacement of the sheets for I_a of $+c/4$ (C) and I_b alternating $+c/4$ and $-c/4$(D) (adapted from [172]).

the pretreatment involves the removal of matrix materials (e.g hemicellulose and lignin), producing bleached Kraft pulps (that is the starting cellulose material used in this thesis). In the second stage the "purified" cellulose is separated into micro- and nanoparticles. There are three approaches usually exploited to isolate cellulose particles: mechanical treatment, acid hydrolysis and enzymatic hydrolysis [164].
To mechanically extract cellulose fibrils high-pressure homogenizers, grinders and ultrasonic treatments have been used. The high shear produced in these treatments causes the cleavage of the cellulose structure, resulting in the extraction of long cellulose fibrils, the so called microfibrillated cellulose (MFC). These are reminiscences of microfibrils. A filtration step is used to remove the larger unfibrillated and partially fibrillated fractions.
The numerous hydrogen bonds are the main obstacle to separate cellulose microfibrils into thinner/shorter particles. To obtain smaller cellulose components the use of never dried source materials [173] and chemical treatments [174–176] are used. The never dried material is required as, upon drying, the spaces among microfibrils is reduced and numerous hydrogen bonds are formed making the separation of these aggregates even harder ("hornification"). After rehydration, most of these hydrogen bonds remain, so that the reswelling does not produce the same "weakening" effect obtained when using never dried cellulose. Moreover, to increase the interfibrillar repulsive forces, it is possible to impart a charge to the surface of the never dried cellulose. This can be done either through oxidation [174] or by functionalization (e.g. carboxymethyl cellulose treatment [176]). Recently a pretreatment that has received much attention is the so called 2,2,6,6-tetramethyl-piperidinyl-1-oxyl radical region selective oxidation (in short TEMPO-oxidation). It is cost-effective, "green" and simple to implement, as so it is the pretreatment of choice for this work. Oxidized NC is easily disrupted and transformed into its nanoscale building blocks via mechanical treatment, as sketched in Fig. 3.5 (left panel).
Several cellulose micro and nano-derivatives are obtained depending on: cellulose source (biosynthesis), type and severity of the processes used for the extraction.

Given such large flexibility, literature data are scattered (broad distributions of lengths, widths and crystallinity) and even the nomenclature of these nanocomponents has not been standardized yet [164]. Generally, the microfibrillated cellulose correspond to the microfibrills, the nanofibrillated particles to the elementary fibrils and the cellulose nanocrystals (CNC) to the crystalline regions (see Fig. 3.5, right panel).

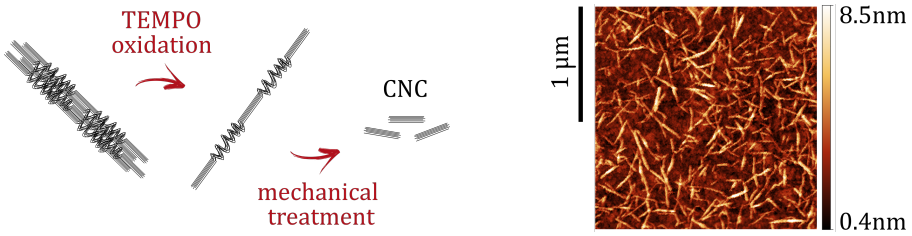

Fig. 3.5: Left panel show a schematic of CNC extraction through TEMPO-oxidation follow by mechanical treatment; right panel reports an AFM images of CNC.

3.1.5 TEMPO-oxidation

Despite the oxidation of alcohols by TEMPO has been known since the eighties [177], only recently this approach has been exploited prior to the mechanical process to facilitate the nanocellulose extraction [178]. TEMPO-oxidation is a method to selectively convert the C6 hydroxyl groups of cellulose to aldehydes and subsequently to carboxyl groups. Crystalline regions are not affected by this reaction because their high packing density render them impermeable. The actual oxidant is the nitrosonium ion ($TEMPO^+$), which is reduced to hydroxyamine (TEMPO-OH) during NC oxidation (see Fig. 3.6).

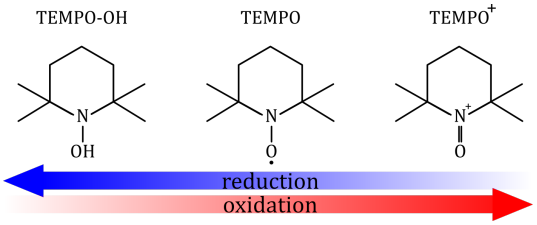

Fig. 3.6: TEMPO oxidation-reduction mechanism.

The four methyl groups in TEMPO sterically blocks its access to the secondary alcohols, so that only primary alcohols are efficienty converted to carboxyl gropus [179]. The oxidation of secondary alcohols by hypobromite is relatively low, so that this competiting reaction can be neglected [180]. TEMPO penetrate the amorphous regions to oxidised the cellulose chains, but it is unable to enter the crystalline regions of cellulose, so that this oxidation method does not cause any changes in the crystalline structure of the cellulose polymorphs I_a and I_b [181] and only the primary alcohols on the surface of the crystallites are available for oxidation [182]. The catalist TEMPO and the cocatalist NaBr are dissolved with cellulose pulp at

pH=10 and the oxidation starts by the addition of the primary oxidant, NaClO; the reaction scheme of the alkaline TEMPO/NaClO/NaBr system is reported in Fig. 3.7. Adding NaClO, TEMPO is oxidized to $TEMPO^+$ by NaBrO (red and blue arrows).

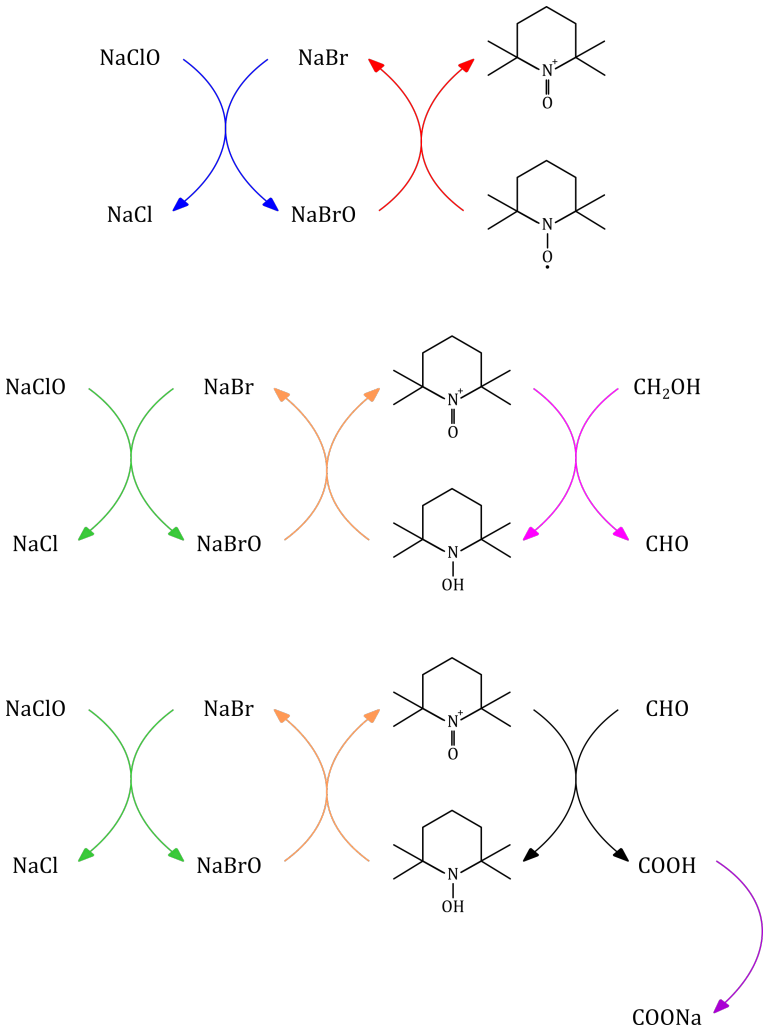

Fig. 3.7: Reaction scheme of TEMPO-oxidation of primary hydroxyls to carboxyl groups via aldehides (adapted from [183]).

$TEMPO^+$ turns to TEMPO-OH by oxidising the alcohol group to aldehyde (magenta arrows). Another $TEMPO^+$ is consumed to convert the aldehide group to the carboxylic group (black arrows). The two $TEMPO^+$ are regenerated from the hydroxylamine through the reduction of NaBrO to NaBr, then OBr^- is reformed thanks to hypochlorite ClO^- (green and orange arrows). Since the pH is around 10, there is an exchange between H^+ and Na^+, turning COOH into COONa (purple arrow). As the reaction proceed, the pH of the suspension decreses, so that NaOH is continuosly added to mantain the pH at a constant value. When either all the primary oxidant has been consumed (various oxidation degrees can be obtained using different amount of NaClO [184]) or all the accessible primary alcohols have been oxidised, the pH becomes stable. The pH is kept around 10 since reaction rate reach its maximum at this pH value and it readily decelerates as the pH decreases.

Higher pH are not used since the oxidised cellulose is prone to degradation (in alkaline conditions the aldehyde groups are prone to β-elimination [185]). The rate constant for hydroxyl oxidation to aldehyde is smaller than the rate constant for the oxidation of aldehide to carboxy group, which leads to the conclusion that in almost all cases the oxidised samples contain more carboxy groups than aldehides [179].
The TEMPO-mediated oxidised pulp maintains an entangled fibrous form, so that it is easy to wash the material removing the excess of chemicals [186].

3.2 Introduction to hydrogels

Hydrogels are solid-liquid systems in which a matrix (usually, but not necessary, polymeric) is loosely cross-linked to form a three-dimensional network, which swells when immersed in water but does not dissolved in it. The ability of hydrogels to absorb water is attributed to the presence of hydrophilic groups (-OH,-SO_3H, -CONH-, -$CONH_2$-, -COOH) in the matrix structure, while their resistance to dissolution arises from cross-links between network chains.
Hydrogels are receiving a great attention in several fields, such as water purification, wound dressing, food additives and pharmaceuticals, drug delivery systems and regenerative medicines, sealing and barrier materials (a complete review is [187]).
The hydrogel matrix is constituted by either **natural** or **synthetic polymers**. Synthetic polymers (such as poly(ethylene glycol), poly(vinyl alcohol), poly(amidoamine), poly(N-isopropylacrylamide), polyacrylamide and poly(acrylic acid) and their copolymers) give hydrogels interesting properties, yet there is a strong effort to replace them with natural alternatives to increase degradability and biocompatibility [188]. Natural polymers used to fabricate hydrogels are hyaluronate, alginate, starch, gelatin, gellan gum, chitosan, pectin, dextran and cellulose and their derivatives.
The hydrogels can be classified on the basis of the cross-linking method into **chemical gels** and **physical gels**: in the former case, the internal network is stabilized by convalent bonds, while in the latter weak intermolecular forces (hydrogen bonds, dipole-dipole, van der Waals forces) strengthen the network. Chemical gels are usually prepared either using cross-linking reagents or by radical cross-linking. Because of the toxicity of many cross-linkers, radical procedure permits the synthesis of safer hydrogels. Radicals are often created at will during the synthesis by UV light [189], ultrasound treatment [190] and ionizing radiation (electron beam or gamma rays) [191, 192]. Physically cross-linked hydrogels are formed spontaneously under appropriate conditions that can be achieved changing parameters such as temperature, pH and salt concentration.
Both cellulose and its derivatives are used to form either chemical and physical hydrogels. Concerning those fabricated with native cellulose, the main difficulty is

its low solubility, due to the strong hydrogen bonds network and the highly knotted fibres. Some particular solvents help to reduce this limit [193], but the most investigated strategy is to substitute the native cellulose hydroxyl groups by methyl groups or hydroxylpropyl groups, so that some hydrogen bonds are prevented and the resultant derivatives (e.g. methyl cellulose (MC), hydroxypropyl cellulose (HPC), hydroxypropylmethyl cellulose (HPMC), and carboxymethyl cellulose (CMC)) become water soluble. Although chemical gels can be fabricated [194], several efforts have been made to produce physical gels, which require easier preparations and are often safer. Relaying on temperature variations, it has been demonstrated that physical gels can be obtained from either native cellulose or its derivatives [195, 196], yet cellulose-derived nanostrucutres are currently investigated for their possibility to form physical gels through ionotropic gelation mechanism. The term ionotropy (ions = ion, trepein = turn) has been introduced as a special case of gelation to describe an unexpected behaviour of alginate that, in contact with a Cu^{2+} solution, formed a hydrogel with parallel aligned, channel-like pores [197]. This process exploits the ability of the carboxyl groups of alginate to chelate divalent ions, leading to the formation of rigid three-dimensional lattices [198], as shown in Fig. 3.8.

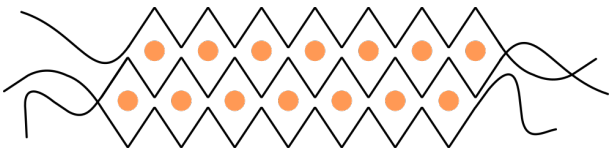

Fig. 3.8: Schematic of the "egg-box" model for alginate gel formation: black lines represent the alginate chains that are coordinated by the ions, depicted as orange circles (adapted from [198]).

Since this first demonstration, ionotropic gelation has been exploited to fabricate hydrogels using polymers other than alginate and also CNC. In particular, the TEMPO-oxidized cellulose nanocrystals, contain both carboxyl and hydroxyl groups that can be cross-linked by cations. The hydrogels characteristics can be tuned using mono- di- or trivalent cations (e.g. Na^{+}, Ca^{2+}, Al^{3+}), as the resulting gel stiffness is proportional to the ratio between the valence and the radius of the cation. [199]. Hydrogel beads are fabricated by dropping either the polymeric solution or the nanocellulose suspension into aqueous solution of polyvalent cations; since cations diffuse into the polymeric drops, the three dimensional ionically cross-linked network is formed (see Fig. 3.9). This method is widely used due to its simplicity; furthermore it allows microencapsulation (active ingredients and cells, food and cosmetics) without using toxic ingredients and with negligible products degradation, since the encapsulation of those materials is performed under mild environment.

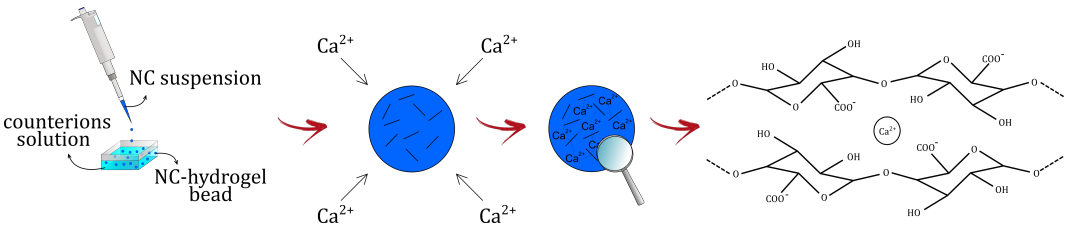

Fig. 3.9: Schematic of the NC hydrogels formation through ionotropic gelation: the beads are formed by dropping the NC suspension in a salty aqueous solution; the electrostatic interactions between negatively charged NC and the salt cations allow the formation of NC hydrogels.

3.3 Results on CFZ and BC release from NC hydrogels

3.3.1 Preparation of NC suspension and NC hydrogels fabrication

I prepare NC suspensions by slightly modifying the procedure proposed in [186]. NC is oxidized at alkaline pH and room temperature: 1 g of never dried cellulose pulp is suspended in 100 mL H_2O and stirred for 1h; then 0.1 g of NaBr, 3 mL of 1.75 M NaClO (3.5 mmol per gram of cellulose) and 16 mg TEMPO are added to the slurry under vigorous stirring. I maintain the pH of the solution in the interval 10.5-11 by adding 1 M NaOH until pH stabilises to a constant value. Then I thoroughly wash the slurry with DI H_2O, to bring it to neutral pH. Using an ultrasonic tip, I sonicate 50 mL of the slurry at 20 kHz and 100 W for 15 min (Bandelin Sonopuls HD2200, tip with a diameter of 13 mm in diameter). Finally, I concentrate the sonicated solution with a rotary evaporator (Heidolph, Schwaback Germany) to a final concentration of TEMPO-oxidized NC of 10 mg/mL.

I prepare different dispersions of CFZ and BC using either TW20 or TW80 surfactants (composition details are given in the following sections). These dispersions are homogenized using a vortexer, then 1.5 mL of NC suspension (10 mg/mL) are added to each dispersion and mixed again.

I fabricate the gels by ionotropic gelation: the beads are formed by dropping the dispersions in aqueous solution of 1M $CaCl_2$ or 1M $AlCl_3$. Since I know the dispersions composition and I weight the extruded dispersions (using an analytical balance), I calculate the amount of the various components in each bead.

I monitor the release either in H_2O or in ETOH. Albeit water is the biologically relevant solvent, the release kinetics cannot be easily monitored at sink conditions in it (due to extremely low molecule solubility). Thus I perform the experiments in water to demonstrate that surfactant co-loading is a successful strategy to increase the drugs solubility; yet I used ETOH as model solvent as it allows to monitor the dynamic of both CFZ and BC release on a reasonable time scale, with good S/N

ratio and at sink conditions. In fact, ETOH is moderately polar and it exchanges easily with the H_2O in the hydrogels and both molecules are soluble in it (CFZ 0.2 mg/mL and BC 0.03 mg/mL).
To monitor the molecule release, at time t=0, 5 loaded beads are immersed in a known amount of solvent (ETOH or H_2O at pH=6.5) in a plastic tube and placed on a shaker.
The solubility of both CFZ and BC in the two investigated solvents differ by orders of magnitudes, so that I have to adopt two diverse strategies to monitor their release:

- in ETOH: at predetermined time intervals I substitute the entire volume of the release medium and I analyse spectrophotometrically the amount withdrawn;

- in H_2O : the limited solubility prevents to perform the experiments at sink conditions. Thus I record the release within a finite release volume (4 mL), up to saturation (at specified time intervals I analyse spectrophotometrically an aliquot of the released medium and then I placed it again in the tube).

All the experiments have been performed at least in triplicate.

3.3.2 Release of CFZ from NC hydrogels

Here below I report the results obtained investigating the CFZ release from NC hydrogels both in ETOH and H_2O. Since I note that CFZ shows complex spectral behaviour in presence of cations, before describing the release experiments, I clarify how this molecule interacts with salts and how the CFZ absorption spectra are affected by such interactions.
Finally, I evaluate the ex-vivo CFZ permeability, using freshly excised rat intestinal mucosa as a model membrane (this work has been done in collaboration with the group of Prof. Andreas Bernkop-Schnürch of the University of Innsbruck).

Interactions of CFZ with cations

During the release experiments I notice that the CFZ spectra show a significant drift that needs to be controlled, thus I investigate the reason of this spectral shape dynamic and the results are reported in this section.
To perform CFZ release in ETOH, I prepare gels with different amount of CFZ per bead, as reported in Tab. 3.1.

The spectrum of pure CFZ dissolved in ETOH is shown with dotted line in Fig. 3.10A. The spectra of the CFZ released from diluted samples (A,B and C) have a red-shifted lineshape with the maximum that moves from 451 to 484 nm (as an

Tab. 3.1: Hydrogels compositions for CFZ release experiments in ETOH.

Sample	CFZ per bead [nmol]	CFZ [mg]	ETOH [μL]	TW20 [mg]
A	10	0.24	150	100
B	55	1.19	150	100
C	490	10.67	150	100
C_0	480	10.2	240	0
D	2935	65	150	100

Sample A and B are obtained by dilution from sample C.

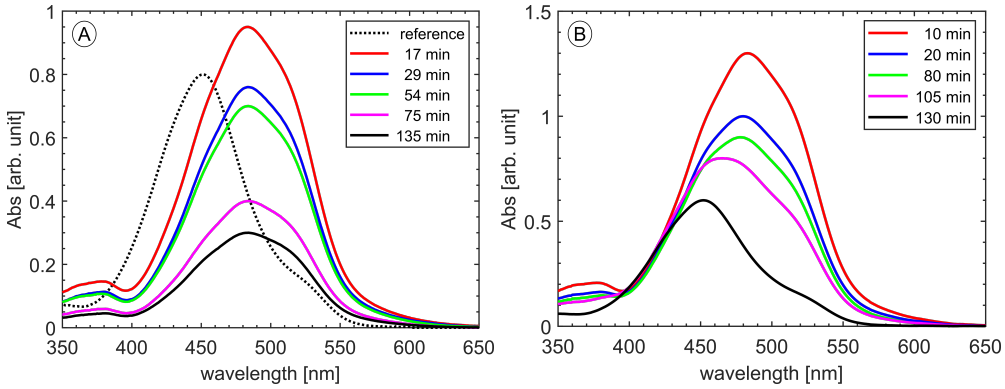

Fig. 3.10: A) Absorption spectrum of CFZ dissolved in ETOH (dotted line) and CFZ relese spectra from sample C acquired at different time (continuous lines); B) CFZ released spectra from sample D acquired at different time.

example, continuous lines of Fig. 3.10A reports the spectra obtained from sample C at different times during the CFZ release). On the other hand the spectrum of CFZ released from the most concentrated sample (D) is characterized by a spectral dynamics that modifies the CFZ spectra with time: as reported in Fig. 3.10B the spectrum starts from a red-shifted and broadened shape and then it recovers that of the pure CFZ dissolved in ETOH. I can exclude any role of the surfactant in this spectral modification, in fact the CFZ released from gels prepared without TW20 (sample C_0) shows the same color-changing phenomenon while the spectrum of CFZ dissolved in ETOH and TW20 does not.
I perform two experiments in solution (i.e without the hydrogels) to further investigate this color-changing phenomenon.

- I prepare a solution of 9.3 μM CFZ with 9.3 μM $CaCl_2$ solution in ETOH and I monitor over time its spectral shape. As reported in Fig. 3.11, initially the spectrum has the same shape as that of CFZ in ETOH (absorption maximum at 451 nm); then it bathochromically shifts. An isosbestic point is clearly evident at 470 nm and after 48 h (i.e. at equilibrium) the absorption maximum is detected at 481 nm.

- I prepare 47 μM CFZ in 2:100=H_2O:ETOH solutions with different salt concentrations in the range from 19.6 nM to 19.6 mM, using both $CaCl_2$ and $AlCl_3$. I wait 50 h to allow each CFZ solutions to equilibrate. The acquired data are

reported in Fig. 3.12: lineshape varies accordingly to salt concentration and presents an isosbestic point at 470 nm.

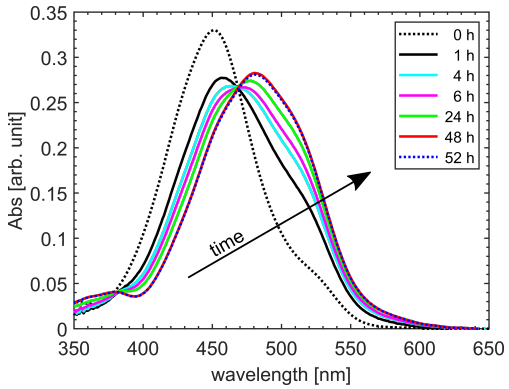

Fig. 3.11: Absorption spectra of CFZ dissolved in ETOH with $CaCl_2$ acquired at different time; the spectra overlap at the isosbestic point (at 470 nm).

CFZ is a weak base and, in aqueous environment, exists under two forms: cationic at low pH and unprotonated at higher pH. The two forms have different absorption spectra and the system presents a clear isosbestic point at about 470 nm [25, 200, 201]. I note that the spectral shape of the cationic CFZ in aqueous medium is the same of CFZ in ETOH added with $CaCl_2$/$AlCl_3$, while the spectrum of the uncharged CFZ in aqueous solution resembles that of CFZ dissolved in ETOH. As reported in [202], a similar spectral modification is observed by adding glacial acetic acid to a CFZ solution in $CHCl_3$.

A plausible hypothesis is that the observed spectral variation is due to coordination between CFZ and cations. I try to obtain the CFZ-cations association/dissociation constants, following the approach used in [203], but the complex dynamics of solvation prevents me from obtaining the equilibrium constant between the CFZ

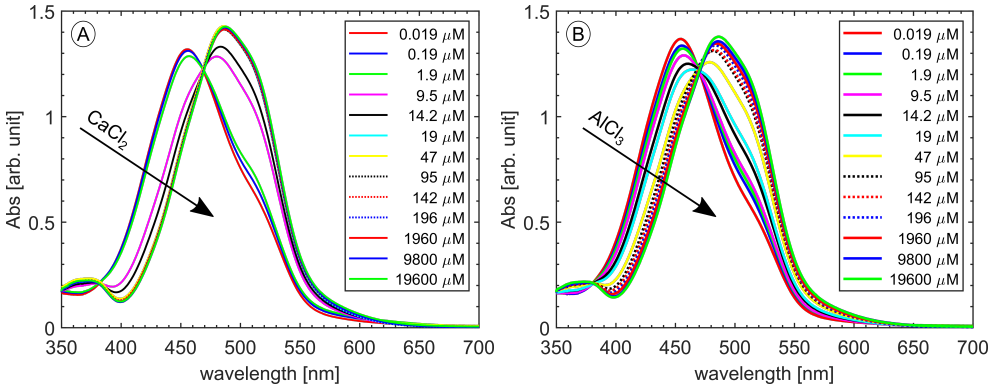

Fig. 3.12: Spectra of CFZ dissolved in ETOH with different amount of A) $CaCl_2$ and B) $AlCl_3$; the spectra overlap at the isosbestic point (at 470 nm).

and the ions. Thus I estimate the CFZ-cations $K_{0.5}$ constants, defined as the salt concentration inducing the 50% of the spectral variation.
I perform this analysis for both Ca^{2+} and Al^{3+}; I correct each spectrum by removing the baseline using a spline function and I fit it with two gaussian functions using the following formula:

$$y = A_1 \cdot e^{-\left(\frac{w-c_1}{d_1}\right)^2} + A_2 \cdot e^{-\left(\frac{w-c_2}{d_2}\right)^2} \tag{3.1}$$

where y is the measured Abs, w the wavelength, while A, c and d are usual gaussian parameters (amplitude, center and width; these parameters are treated as free during the fit). Two examples of this analysis performed with Al^{3+} are reported in Fig. 3.13.

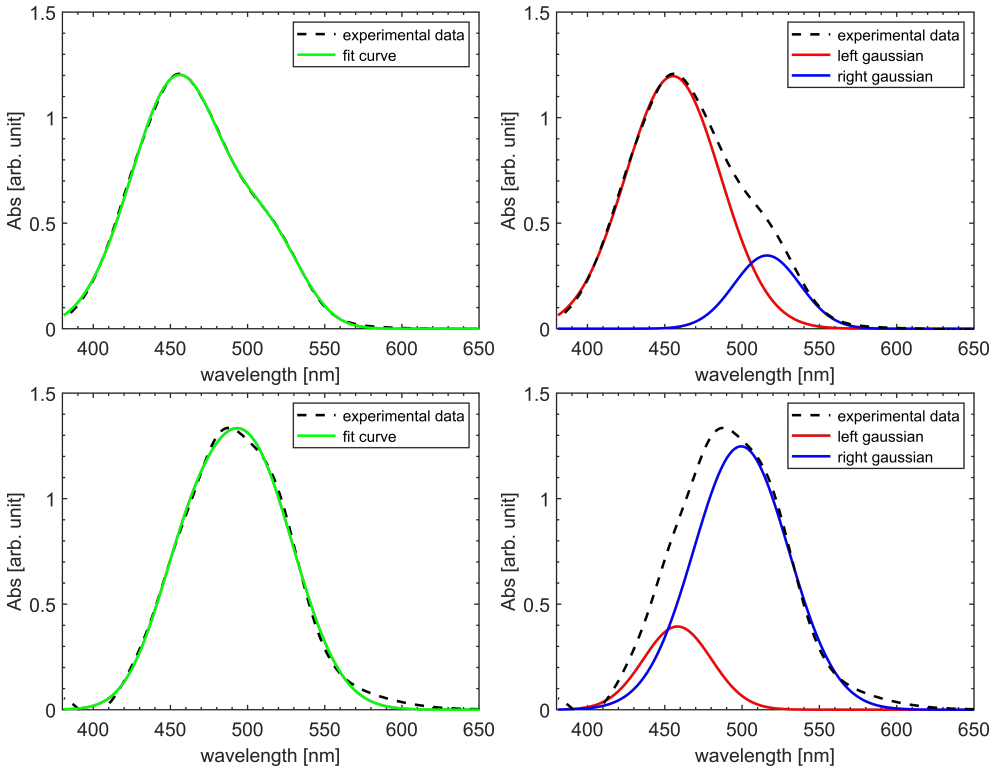

Fig. 3.13: Spectrum of CFZ in 19.6 nM (top panel) and 19.6 mM of $AlCl_3$ (bottom panel). Left panels report the experimental data (black dotted line) with the fit curve (green line); right panels show the two gaussian contributions (red and blue lines) superimposed to the experimental data (black dotted line).

Fig. 3.14 shows the normalized amplitude (A) of the two gaussian functions versus the $\log_{10}$ of the salt concentration. The $K_{0.5}$ values for $AlCl_3$ and $CaCl_2$ are about 10 and 200 μM, respectively. The same values are obtained considering either the decrease in amplitude of the left gaussian or the increase of the right one. Since the spectra acquired at salt concentration greater than 9800 μM have the same spectral shape in both salts, I assume that, at this concentration, CFZ is fully solvated by

both cations. Using 47 μM concentrated CFZ solutions this saturation happens at about 20 μM and 10000 μM in the case of $AlCl_3$ and $CaCl_2$, respectively. Since the CFZ-cations interactions are electrostatic and characterized by a limited chemical specificity, it is reasonable to assume that more Ca^{2+} ions are needed to solvate a single CFZ, while one Al^{3+} interacts with more CFZ molecules.

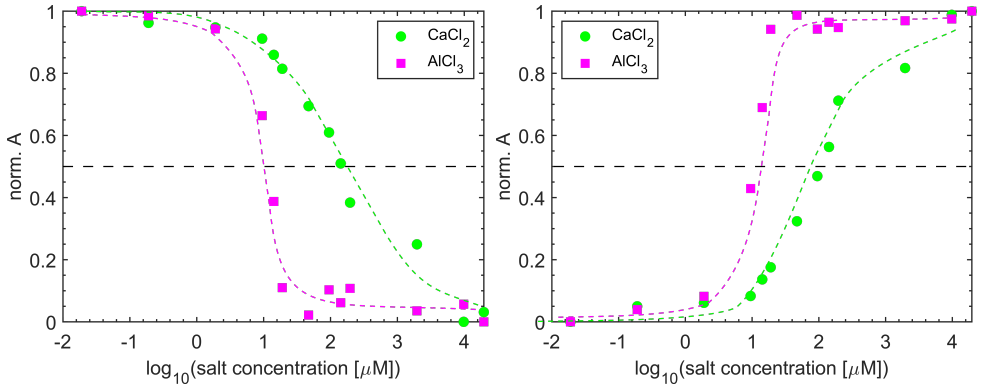

Fig. 3.14: Normalized amplitude (A) of the gaussian function centered around 455 nm (left panel) and 510 nm (right panel) versus the $\log_{10}$ of the salt concentration for both $AlCl_3$ (magenta-squares) and $CaCl_2$ (green-circles); lines are guide for the eyes.

The dynamic of the CFZ spectra reported in Fig. 3.10 can be described considering that inside the as-formed gel beads there is an excess of salts [204]. Thus in samples with lower CFZ concentration (A, B and C), all the released molecules are coordinated to $CaCl_2$; on the other hand for sample D, the loaded CFZ concentration is so high that the excess of salt inside the gels is not enough to coordinate all the loaded molecules. In this case the first released CFZ are coordinated to the ions (red line in fig. 3.10B), but as time goes by, more and more CFZ are released unbound and the spectra of the released molecules revert to that of the CFZ in pure ETOH (black line in fig. 3.10B).

Kinetics of CFZ released in ETOH

CFZ release experiments in ETOH have been performed using the same samples reported in Tab. 3.1 and, if not otherwise specified, the gels have been fabricated with $CaCl_2$. The fact that, in presence of salts, CFZ exists under two forms (coordinated and uncoordinated), allows to quantify the total amount of released CFZ using the isosbestic point, whatever the form present in solution [25]. From the data shown in Fig. 3.11, I calculate the molar absorption coefficient at the isosbestic point, that is 25900 $L \cdot mol^{-1} \cdot cm^{-1}$.

Fig. 3.15A shows the normalized release profiles fitted with the the empirical 1^{st}-order model (see Eq. 1.13). This model fits rather well the experimental data (with R^2 of 0.998, 0.995, 0.996 and 0.988 for samples A, B, C and D, respectively).

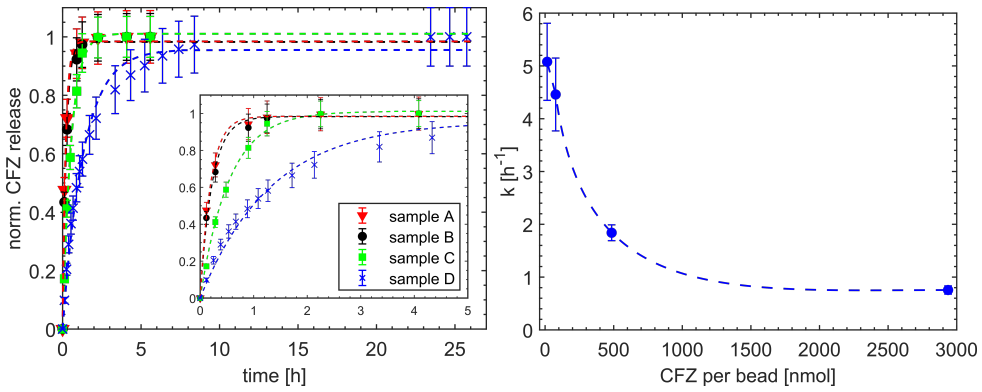

Fig. 3.15: A) Normalised CFZ release profiles in ETOH from sample A (red-triangles), B (black-circles), C (green-squares) and D (blue-crosses) fitted with the empirical 1^{st}-order model (dotted lines); the inset shows a zoom up to 5 h. B) k coefficient values as a function of the amount of CFZ per bead; errorbars are prediction bounds and line is a guide to the eyes.

Looking at the value of the k coefficients (see Fig. 3.15B) it seems that an increase in the amount of loaded CFZ, gives rise to slower release kinetics. Actually, it should be remembered that k is expressed in $time^{-1}$ [h^{-1}], so that it does not give information about the molecular flux (unless the beads have the same size and shape and are loaded with the same amount of drug). Such information can be obtained looking at the absolute values of the release (see Fig. 3.16, left panel) and their 1^{st} order derivative (see Fig. 3.16, right panel): the higher the loading values, the larger the molecular flux, meaning that the limiting step for the CFZ release is not the molecular diffusion from the bead surface to the solvent. To better understand the parameters that play a role in the CFZ kinetics, I compare the release from sample C (about 485 nmol per bead, green dotted line in Fig. 3.17, left panel) with the release of the last 485 nmol from sample D (red continuous line in Fig. 3.17, left panel). Assuming the drug homogeneously dispersed in the gel beads and the same dynamic of CFZ aggregates dissolution, I would have expected the same release profile. Actually, as reported in the inset, despite the amount of CFZ per bead is the same, different kinetics are observed; in particular the release of the last CFZ

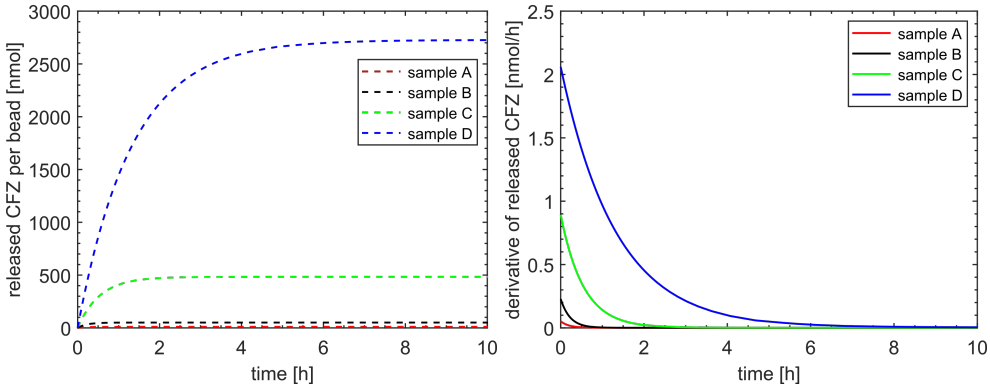

Fig. 3.16: Left panel shows the fit curves obtained with the empirical 1^{st} order model as a function of time; right panel reports the 1^{st} order derivative of the fit curves.

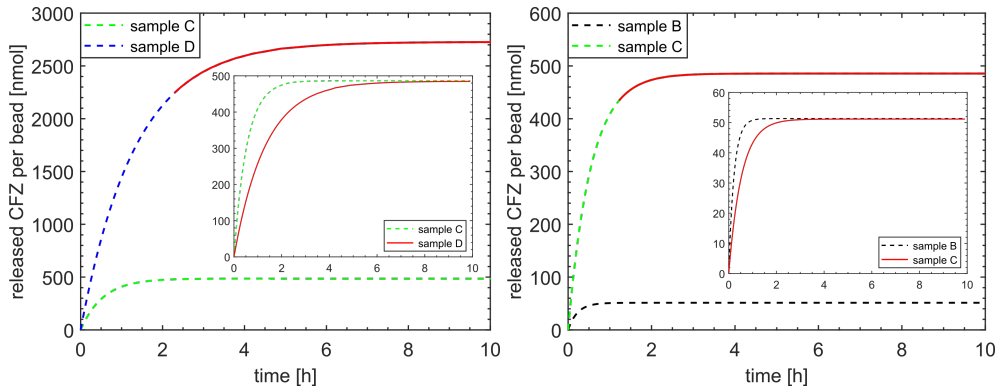

Fig. 3.17: Left panel reports the fit curves of sample C (green dotted line) and D (blue dotted line); red continuous line highlights the last part of the release from sample D, to be compared with the release from sample C, as reported in the inset. Right panel shows the fit curves of sample B (black dotted line) and C (green dotted line); red continuous line highlights the last part of the release from sample C, to be compared with the release from sample B, as reported in the inset.

molecules from sample D is slower with respect to the same amount of CFZ from sample C. I obtain an analogous result when comparing the release from sample B (black dotted line in Fig. 3.17, right panel) with the last part of the release from sample C (red continuous line in Fig. 3.17, right panel). These different kinetics can be due to a non homogeneous CFZ distribution inside the gels when considering the last part of the release (e.g. the external shell of the bead of sample D has a lower CFZ concentration with respect to that of sample C), but also to the formation of different aggregates distribution (i.e. the number of aggregates and their dimensions can change as a function of the drug loading).

To confirm the fact that the CFZ release is not diffusion limited, I use the well-known power law model (see Eq. 1.14), taking into account the first 60% of the released process: I find values of the exponent n (from 0.44 to 0.9) always greater than the one predicted for fickian (i.e. diffusion limited) release from spherical beads (n=0.43)[205]; moreover there is no clear dependence of n values from the amount of CFZ initially loaded.

Since I believe that the presence of CFZ aggregates within the hydrogel and the dynamics of their dissolution play an important role in the release kinetics, I try to use also the model that consider suspensions (see Eq. 1.8). All the parameters in Eq. 1.8 are known, except D and c_s. Considering a fast exchange between ETOH and H_2O (qualitatively demonstrated in Fig. 3.18), I assume that the liquid phase is constituted by pure ETOH, thus the only free parameter is D. This model is valid as long as the drug concentration in the matrix largely exceeds its solubility. For this reason, among the four tested samples, I can use only the two most concentrated, since they have a reasonable amount of data to be fitted. The results are shown in Fig. 3.19: red data are discarded from the fit, as for these points, the concentration is below the CFZ solubility. Despite the model fits rather well sample C, it is evident that it can not be generalised to higher concentrations (as it badly reproduces the

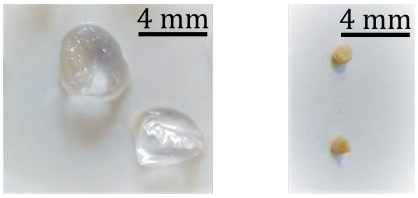

Fig. 3.18: Pictures of NC gels after being immersed for 20 min in H_2O (left panel) and ETOH (right panel) and then drying in air for some hours. The fact that ETOH exchanges easily with H_2O is demonstrated by the shrinking of the beads once they are left to dry in air.

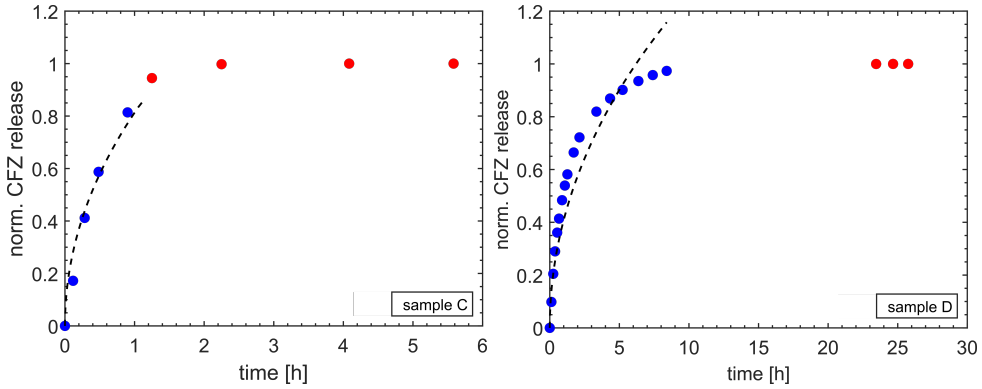

Fig. 3.19: Normalised CFZ release profiles in ETOH from sample C (left panel) and D (right panel) fitted with the model that consider diffusion from suspensions (black dotted lines); red data are discarded from the fit.

data of sample D). Since the experiments have been performed at sink conditions, the saturation of the solution can not be the reason why this model does not describe the CFZ release kinetics. I believe that mechanical/structural modifications in the gels (e.g. swelling induced by the solvent exchange or inhomogeneous gel environment) that give rise to a time- and space-dependent D.

The amount of CFZ estimated from absorbance measurements is compatible within 5% with the amount loaded into the beads, thus I demonstrate a quantitative release of CFZ from NC hydrogels.

To obtain rate-controlled DDSs an interesting strategy is given by the use of hydrogels with different mechanical characteristics. This can be achieved by tuning hydrogels stiffness using different multivalent cations as crosslinkers during ionotropic gelation [206]. I prepare gels using the same composition of sample C and either $CaCl_2$ or $AlCl_3$ as crosslinker; then I monitor the drug release kinetics in ETOH. Fig. 3.20 reports the normalized release profiles fitted with the the empirical 1^{st}-order model (see Eq. 1.13). This experiment has been performed with gel beads containing the same amount of CFZ, so that (differently from the dataset shown in Fig. 3.15) the k values give information about the molecular flux. I find that the ratio k_{Al}/k_{Ca} is equal to 0.6: since Al-based hydrogels are stiffer than those formed using Ca^{2+}, the NC hydrogels formed using $AlCl_3$ release the drug more slowly than $CaCl_2$ gels.

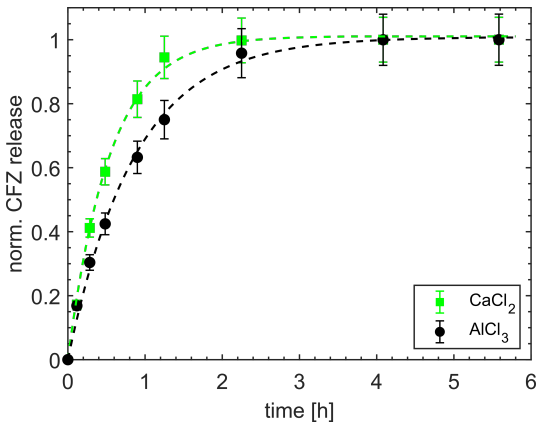

Fig. 3.20: Normalized CFZ release profiles in ETOH from $CaCl_2$ (green-squares) and $AlCl_3$ gels (black-circles), fitted with 1^{st} order model (dotted lines). The values obtained for k are k_{Al}= 1.1±0.1 h^{-1} and k_{Ca}= 1.8±0.2 h^{-1} (errors are prediction bounds).

Kinetics of CFZ released in water

In this section I demonstrate the use of NC hydrogel to increase the CFZ solubility in water. To do so, I prepare gels with the same amount of CFZ (490 nmol for each bead) that differ for both type and amount of surfactant, as reported in Tab. 3.2 (the label assigned to these samples are (type of TW)-(amount of TW per beads [mg])).

Tab. 3.2: Hydrogels compositions for CFZ release experiments in H_2O.

Sample	**CFZ [mg]**	**ETOH [μL]**	**TW20 [mg]**
TW20-0	11.12	240	0
TW20-0.7	11.23	208	35
TW20-2.4	11.25	137	114
TW20-3.3	11.15	93	162
Sample	**CFZ [mg]**	**ETOH [μL]**	**TW80 [mg]**
TW80-3.3	11.09	92	158

The absorption spectra acquired for the different samples and at different time have the same spectral shape (an example is reported in Fig. 3.21, continuous blue line) with an absorption maximum at 492 nm. The red-shift can be due to either CFZ coordinated to $CaCl_2$ or protonated CFZ (since the $pH_{\text{aqueous media}} < pKa_{\text{CFZ}}$=8.51 [24]). The facts that the spectra of CFZ released from gels with and without TW have the same spectral shape and the absence of scattering suggest that TW is able to solubilize CFZ without forming large micelles.
Fig. 3.22A shows the amount of released CFZ, that has been quantified using the absorbance value at the isosbestic point.

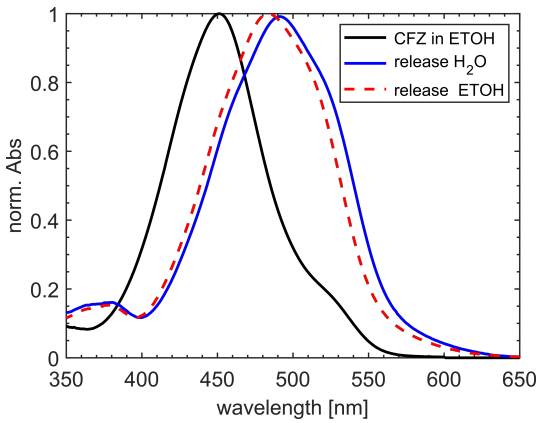

Fig. 3.21: Normalised spectrum of CFZ dissolved in ETOH (continuous black line) compared to the normalized spectra of CFZ acquired during the release of CFZ in H_2O (continuous blue line) or in ETOH (dotted red line).

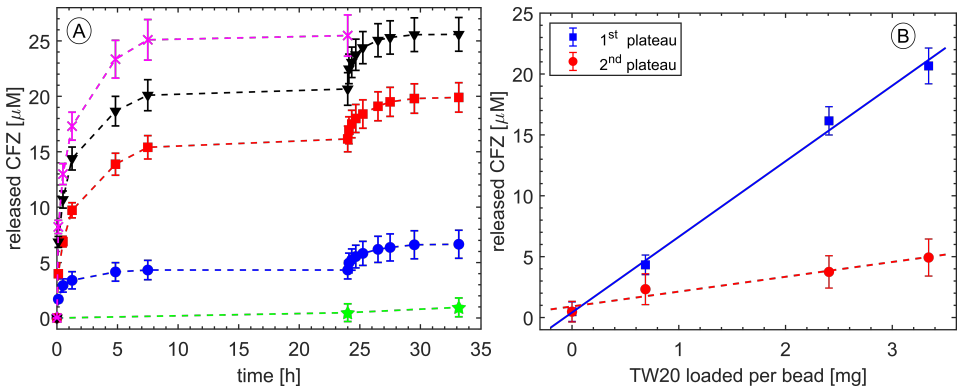

Fig. 3.22: A) CFZ release profiles in H_2O from T-0 (green-stars), TW20-0.7 (blue-circles), TW20-2.4 (red-squares), TW20-3.3 (black-triangles) and TW80-3.3 (magenta-crosses); lines are guide to the eyes. B) Linear relationship between the amount of CFZ released at the plateaus and TW20 content per bead (the first saturation plateau is indicated by the blue continuous line, the second one by the red dotted line).

After 24 h a plateau is reached and the concentration of CFZ released from hydrogels without TW is only 0.48 μM (green-stars in Fig. 3.22A). On the other hand, gels with TW20 release an amount of CFZ proportional to the surfactant concentration, as reported in Fig. 3.22B (blue line). In the case of TW20-3.3, CFZ concentration reached 20.7 μM, i.e. the H_2O solubility of CFZ is increased by 43 times (black-triangles in Fig. 3.22A). Using the same amount of surfactant, but substituting TW20 with TW80, the CFZ concentration can be further increase to 25.5 μM, i.e. 53 times the CFZ H_2O solubility (magenta-crosses in Fig. 3.22A).
After 24 h I substitute the release media and the CFZ restarts to diffuse from hydrogels until another saturation is reached (this experiment has not been performed using TW80). Also in this case the amount of CFZ released at plateau (at 33 h) and the quantity of TW20 loaded correlate linearly, as reported in Fig. 3.22B (red line). Furthermore, the CFZ concentrations in the release media are much higher than its solubility, suggesting that after 24 h inside the gels there are still TW20 molecules. These two observations lead to the following alternative hypotheses:

1. the presence of the plateaus is due to the fact that the maximum CFZ solubility in a solution with TW20 is reached: by increasing the TW20 content inside the gels, more TW20 will be present in the released media at equilibrium, so that more CFZ is solubilized;

2. the presence of TW20 within the gels has an active role in increasing the mass transport of CFZ from the gel to the aqueous solution.

Here below, I firstly report a simple model that supports the second hypothesis, and then I will describe the experiment carried out to exclude the first one.
Assuming TW20 is free to diffuse, after 24 h it equilibrates both inside the gels and in solution, thus hindering the release of other CFZ molecules; once the release medium is substituted, TW20 restarts to diffuse from the gels and it solubilises other CFZ molecules.
According to this simple model, I estimate the ratios TW/CFZ. I know that 5 gel beads of the sample TW20-0.7, TW20-2.4 and TW20-3.3 contain 2800, 9800 and 13600 nmol of TW20, respectively. Each bead has a spherical shape (0.6 cm in diameter), so the volume occupied by the 5 beads is 1.88 cm^3. The first release has been performed in 4 mL and, assuming the TW20 is free to diffuse, at equilibrium (after 24 h) it will have the same concentration both in the gels and in the release medium (1.88+4=5.88 mL). Since the volume of the release media is the 68% of the total volume, the equilibrium concentrations of TW20 in the release media are 480, 1670 and 2310 μM. The same estimation can be done for the second release, that has been performed with 5 beads in 3 mL: in this case the solvent volume is 61% of the total volume and the TW20 concentrations in the release media, at equilibrium, are 180, 640 and 890 μM. In Fig. 3.23 I report the released amount of CFZ versus that of TW20 for the first and the second release and I fit the data with a linear model (the black line is the fit of the first saturation, while the data of the second plateau are fitted by the green line). The TW20/CFZ ratio in the release media at equilibrium is given by the inverse of the slope: I find values of 111 (first release) and 218 (second release). Performing the same calculation for the gels containing TW80 (considering the plateau reached after 24 h) I obtained that TW80 concentration at equilibrium is 2130 μM, thus the TW80/CFZ ratio is given by 2130/25.5=84.
To validate this simple model, I prepare saturated CFZ solutions in 23, 230, 1150 and 2300 μM of TW20 and 2100 μM of TW80. I mix them with a vortexer and, after some hours, I centrifuge them (at about 15000 g for 5 min) to acquire the surnatants absorption spectra. The CFZ concentrations (estimated at the isosbestic point) as a function of surfactant concentrations are reported in Fig. 3.24. The amount of CFZ in the surnatants containing 2300 μM of TW20 and 2100 μM of TW80 are 19.8 and 24.8 μM, respectively. These values are very close to the quantity of CFZ released from the gels after 24 h (i.e. 20.7 and 25.5 μM). Furthermore, I fit the TW20 data

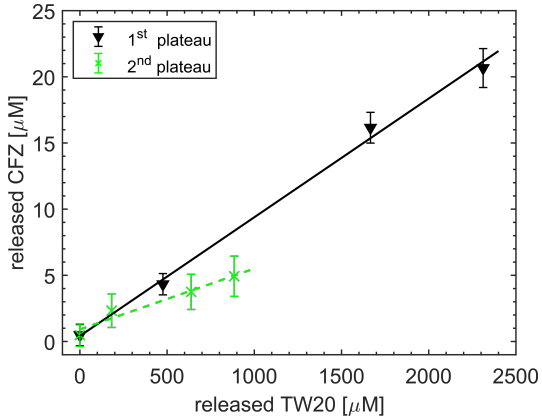

Fig. 3.23: CFZ released after 24 h (black-triangles) and after 33 h (green-crosses) versus estimated TW20 concentration at equilibrium; the black continuous line is the linear fit for the first plateau, while that of the second saturation is the green dotted line.

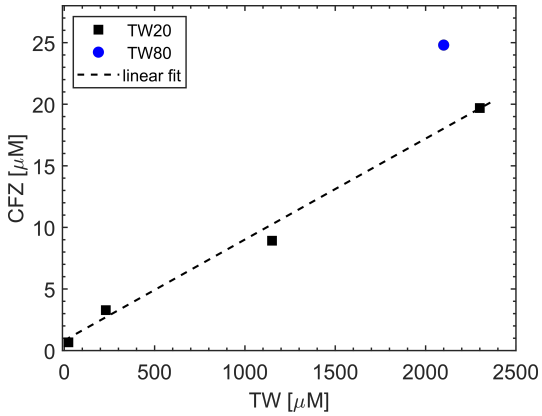

Fig. 3.24: Amount of solubilised CFZ as a function of surfactant concentration (TW20 black-squares and TW80 blue-circle) concentrations. The black dotted line is the linear fit of the data obtained using TW20.

with a linear curve (red line in Fig. 3.24): from the inverse of the slope, I obtain the ratio TW20/CFZ equal to 123. This value has to be compared with 111, obtained from Fig. 3.23. Although the surfactant aggregation number strongly depends on pH, ionic strength, presence of solvents and molecules inside the micelles, all the obtained estimations are of the same order of magnitude (roughly 100) of TW20 and TW80 aggregation numbers in H_2O [207–209].

At this point, I show the result that permits to exclude the hypothesis that the plateau is due to the saturation of the CFZ-TW20 aqueous solution. In fact, I would have expected that using gels without surfactant (i.e. TW20-0) and performing the release in water containing 2300 μM of TW20, the amount of CFZ in the release media would be about 20 μM. Actually, the CFZ concentration after 24 h is only 2.6 μM; this very low value confirms that the surfactant diffusion from the gels is the driving force for the CFZ delivery, as described in the model above.

Permeability study of CFZ across rat intestinal membrane

The promising results obtained from the CFZ release in H_2O suggest a possible application of NC hydrogels as DDS. To verify this possibility I tried to evaluate the CFZ permeability ex-vivo, using the rat intestinal mucosa as a model membrane and EtOH as a model solvent. Initially I try to evaluate the permeation of CFZ released in water from the gels, but the CFZ signal is below the instrumental detection limit, even using the most concentrated solutions. For this reason I prepare CFZ alcoholic solutions with and without TW20 (0.16 mg/mL CFZ + 3 mg/mL TW20 in EtOH and 0.16 mg/mL CFZ in EtOH) in order to evaluate the potential permeation-enhancing effect of TW20 solvated CFZ through freshly excised intestinal mucosa. A piece of intestine is mounted on Ussing-type chambers (Warner Instruments, LLC; 1125 Dixwell Avenue; Hamden, CT 06514, USA) with a surface area of 0.64 cm^2 (see Fig. 3.25). After an incubation of 15 min with PBS at pH=6.8 to properly wash the intestine piece (as required by the typical protocol used pharmacists) I substitute the PBS with ETOH in the acceptor compartment and I fill the donor chamber with CFZ solution. At predetermined time points (0, 30, 60, 90, 180 and 360 min) I remove 100 μL from the acceptor and I immediately replaced them with fresh medium. I use a multifunctional microplate reader (TECAN SPARK, Tecan Austria GmbH, Grödig, Austria) to spectrophotometrically quantify the amount of permeated CFZ: I measure the absorbance of the withdrawn samples at 470 nm considering the molar absorption coeff at the isosbestic point.

The comparison of the drug permeation of solutions with and without surfactant is reported in Fig. 3.26.

According to the acquired data the presence of TW20 increases by a factor 2 the CFZ permeability. This result is very promising, since it demonstrates that the surfactant co-loading increases both the CFZ H_2O solubility and its permeability through the intestinal membrane.

The permeability quantification of such insoluble molecule using the aqueous release media requires optimize experiments that will be the subject of future investigations.

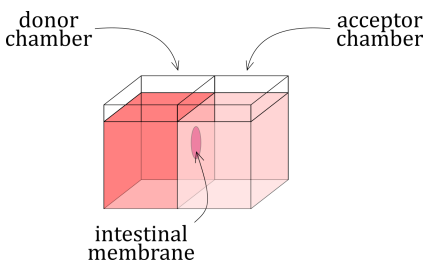

Fig. 3.25: Schematic of the Ussing-type chamber.

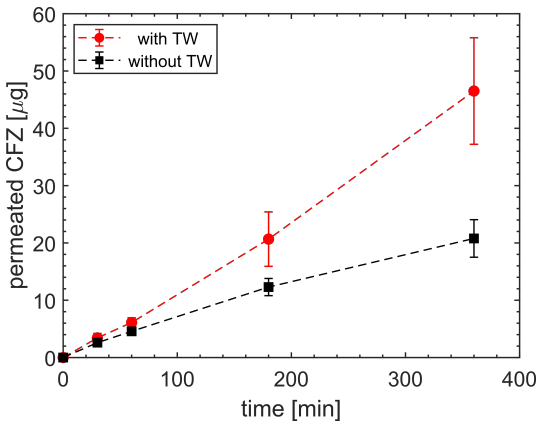

Fig. 3.26: Ex-vivo CFZ permeation across intestinal mucosa during 6 h using solution with (red-circles) and without (black-squares) TW20; lines are guide to the eyes.

3.3.3 Release of BC from NC hydrogels

Considering the good results obtained by the release of CFZ from NC hydrogels, I performed similar experiments using BC, too. In this section I report the results obtained using both ETOH and H_2O as release media.

Kinetics of BC released in ETOH

Tab 3.3 reports the composition of the different prepared gels.

Tab. 3.3: Hydrogels compositions for BC release experiments in ETOH.

Sample	BC per bead [nmol]	BC [mg]	ETOH [μL]	TW20 [mg]
A	10	0.27	148	100
B	55	1.35	148	100
C	460	11.68	148	100

Sample A and B are obtained by dilution from sample C.

The spectra of BC released from the gels have the same shape as that of BC dissolved in ETOH. Differently from the CFZ, BC molecules do not interact with cations, as there are no spectral variation in solutions with and without salts dissolved. To quantify the total amount of released BC, I use the value of the absorbance maximum in ETOH (452 nm) and a molar absorption coefficient of 144000 L·mol^{-1}·cm^{-1}. The normalized release profiles fitted with the empirical 1^{st}-order model (see Eq. 1.13) are shown in Fig. 3.27. The amount of released BC estimated from spectrophotometric measurements and that loaded into the beads are compatible within 6%, thus a quantitative release of BC from NC hydrogels is demonstrated.

Since the beads are not loaded with the same amount of BC, the k coefficients give no information about the molecular flux, but I can compare these k values with those obtained from gels loaded with the same CFZ concentration. As reported in Tab. 3.4 it is evident that the BC kinetics are much slower than those of CFZ. The slower

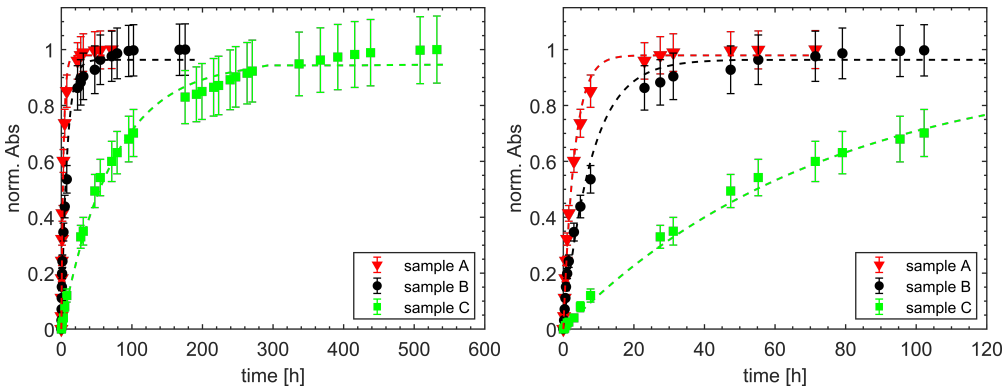

Fig. 3.27: Left panel shows the normalised BC release profiles in ETOH from sample A (red-triangles), B (black-circles) and C (green-squares) fitted with the empirical 1^{st}-order model (dotted lines); right panel reports a zoom up to 120 h.

BC kinetic does not depend on its lower solubility in the release medium (in ETOH the solubility of BC is 0.03 mg/mL vs 0.2 mg/mL of CFZ). In fact, I perform releases of BC in acetone (BC solubility = 0.2 mg/mL) and I compare the obtained release kinetic with that of CFZ in ETOH (see Fig. 3.28). To quantify the amount of released BC I use the maximum absorbace value (at 454 nm) and ϵ=140000 L·mol^{-1}cm^{-1}. Although BC in acetone and CFZ in ETOH have the same solubility and about the same molecular weight (537 vs 473 gr/mol), their very different shapes (see Fig. 1.2), the fact that they interact differently with the gel components and the different solvent viscosity give rise to diverse rate releases ($k_{CFZ\text{-}ETOH} = 1.8 \pm 0.2$ h^{-1} vs $k_{BC\text{-}acetone} = 0.15 \pm 0.02$ h^{-1}).

Tab. 3.4: k coefficients obtained fitting the data of CFZ and BC release in ETOH; errors are prediction bounds.

CFZ per bead [nmol]	BC per bead [nmol]	k_{CFZ} [h^{-1}]	k_{BC} [h^{-1}]
10	10	5.1±0.7	0.32±0.03
55	55	4.5±0.7	0.13±0.02
490	460	1.8±0.2	0.014±0.001

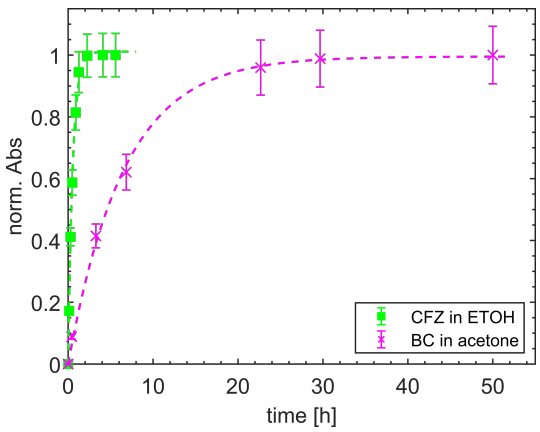

Fig. 3.28: Normalised CFZ release profile in ETOH (green-crosses) fitted with the empirical 1^{st}-order model (dotted lines).

Kinetics of BC released in water

To demonstrate that the co-loading of BC and surfactants inside the NC hydrogels is a successful strategy to increase the BC solubility in water, I prepare gels with the same amount of BC (430 nmol for each bead) containing either TW20 or TW80 (details about compositions are given in Tab. 3.5).

Tab. 3.5: Hydrogels compositions for BC release experiments in H_2O.

Sample	**BC [mg]**	**ETOH [μL]**	**TW20 [mg]**
TW20-BC	11.01	93	162
Sample	**BC [mg]**	**ETOH [μL]**	**TW80 [mg]**
TW80-BC	11.24	88	162

Absorption spectra have all the same spectral shape (an example is shown in Fig. 3.29A), with an increasing contribution due to scattering at wavelengths below 500 nm. To quantify the amount of BC released, I used the peak at 458 nm (assuming ϵ=144000 L·mol^{-1}cm^{-1} and a negligible scattering at this wavelength) and the data are reported in Fig. 3.29B. A control experiment with BC-hydrogels without surfactants (11 mg BC and 153 μL ETOH) shows no signal in the region characteristic of BC after 24 h of release time.

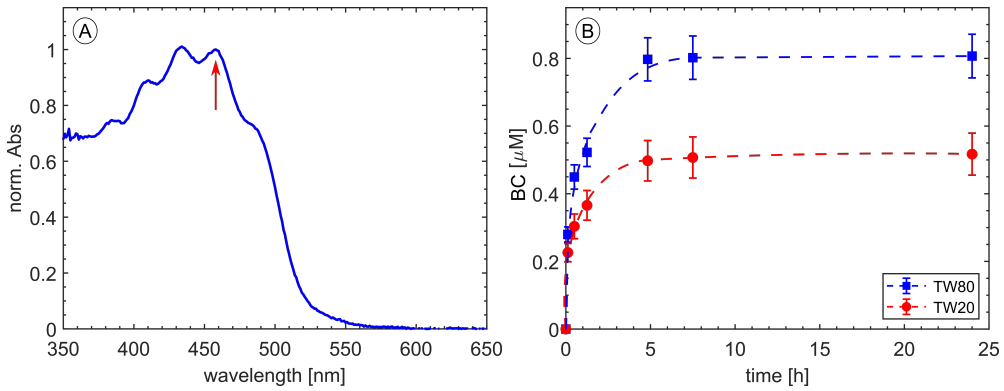

Fig. 3.29: A) Normalised BC spectrum acquired during the release of BC in H_2O; red arrow indicates the peak at 458 nm. B) BC release profiles in H_2O from TW20-BC (red-circles) and TW80-BC (blue-squares); lines are guide to the eyes.

To investigate the reason of the scattering in the UV part of the spectrum, I prepare aqueous solution of TW20 and TW80 at concentration higher than their critical micelles concentration. Since the acquired spectra are flat, I hypothesize that the scattering is due to larger surfactant micelles containing BC. To verify this hypothesis I have to destabilize the micelles and extract the BC using the solvent extraction method (to note that such experiment requires a large number of different samples

as, for each release point, 3 samples are needed to perform the experiments in triplicate). At predetermined time, 1 mL of each release medium is added to 2 mL of hexane (BC solubility: 0.6 mg/mL [160]). To extract the BC, I mix the solutions with a vortexer and I use an ultrasound treatment to disrupt the micelles (5 min at 400 W), finally I centrifuge (at about 5200 g for 3 min) to separate the two phases. The absorption spectra of the aqueous phase do not show any signal in the BC region; on the other hand, the absorption spectrum of the organic phase (reported in Fig. 3.30A), clearly shows the typical BC spectrum. The amount of BC in this phase (estimated using the maximum absorbance value at 450 nm and ϵ=140000 L·mol^{-1}cm^{-1}) is reported in Fig. 3.30B. To note that the scattering is highly reduced in these surnatants, supporting the idea that BC is contained within micelles disrupted upon sonication. From both analyses (see Fig. 3.29B and 3.30B) the amount of BC released from gels containing TW80 is higher with respect to that release when TW20 is used. The high SD in the BC concentrations obtained using the solvent extraction method are due to the fact that the different components of the suspensions (BC, H_2O, hexane and surfactant) do not always mix in the same manner (as an example, I can not exclude that either some hexane is entrapped in surfactant micelles in H_2O, leading to an effective increase in the amount of BC released or some BC remains inside the micelles in H_2O, so that the quantity of BC is underestimated).

As in the case of CFZ, I try to form BC-TW micelles in H_2O preparing saturated solutions of BC in either 2300 μM or 2100 μM of TW20 and TW80. I mix them with a vortexer and sonicate (up to several minutes at 400W). Finally, I centrifuge (about 15000 g for 5 min) them to acquire the surnatants absorption spectra; in none of the cases I see the BC absorption spectra, not even by adding ETOH and NC to these saturated solutions.

These results are quite surprising, as they suggest that the BC released from the gels is entrapped in micelles that form only thanks to NC hydrogels. Probably, when both BC and TW are loaded within the hydrogels they are forced to orient themselves in

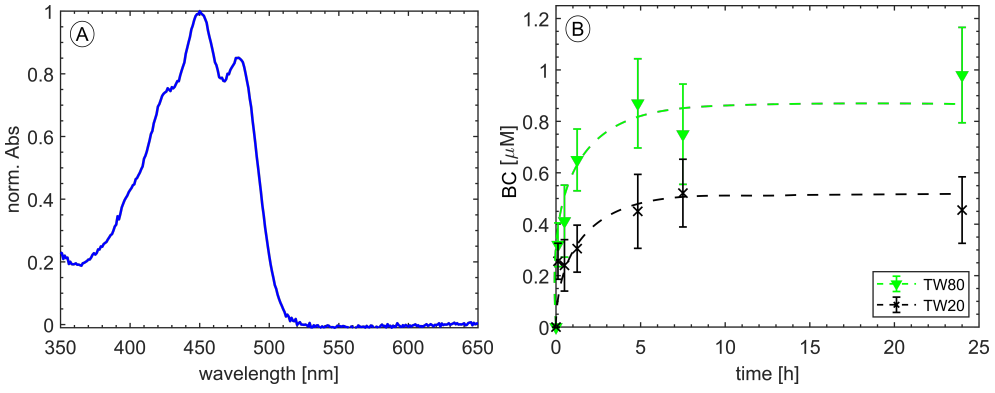

Fig. 3.30: A) Normalised spectrum of the BC in the organic phase. B) Amount of BC released in H_2O from gels with TW20 (black-crosses) and TW80 (green-triangles) estimated by the solvent extraction method; lines are guide to the eyes.

such a way that eases the formation of TW micelles entrapping BC, while when TW molecules are free to move in the aqueous environment, the formation of micelles without BC is favoured.
With these experiments I demonstrate that the co-loading of BC and surfactants is a successful strategy to solubilize BC in H_2O and that the formation of solid dispersion in the NC hydrogels is crucial to obtain BC-TW micelles.

3.3.4 Storage of CFZ and BC in NC hydrogels

The promising results obtained releasing both the hydrophobic molecules in H_2O suggest to verify if the NC hydrogels carriers protect the molecules from degradation, too.
I prepare both CFZ and BC loaded hydrogels using TW20 and TW80 (details about composition are given in Tab. 3.6).

Tab. 3.6: Hydrogels compositions used in the storage experiment.

Sample	CFZ/BC [mg]	ETOH [μL]	TW20/TW80 [mg]
TW20-CFZ	5.3	61	196
TW80-CFZ	5.3	60	192
TW20-BC	5.3	61	196
TW80-BC	5.2	60	192

The loaded beads have been stored in plastic tubes in the dark at room temperature for 45 days and then I perform the release in ETOH.
The quantity of released CFZ from gels quantified from spectrophotometric measurements is 98%$\pm$6 (TW20) and 105%$\pm$6 (TW80) of that loaded into the beads, thus I demonstrate that a quantitative release of CFZ from NC hydrogels can be obtained even after 45 days. Surprisingly, the amount of BC released from the NC hydrogels after 45 days of storage is 86%$\pm$5% and 92%$\pm$6% of the loaded one, in the case of TW20 and TW80, respectively. Thus, despite BC loaded into the gels is immersed in aqueous environment, the surfactant protects this delicate drug from degradation over quite long time scale. Tab. 3.7 compares these results with those reported in Sec. 2.2.8 and in Appendix; it demonstrates that NC beads are very promising BC carriers able to protect this delicate molecule and they heavily slow down its degradation.

Tab. 3.7: Amount of non-degraded BC (relative to that at t=0) after 15 and 45 days under various conditions; all samples have been kept in the dark and, unless otherwise specified, at room temperature.

storage time [days]	storage condition	% recovered BC
15	$PSi_{as\text{-}etched}$	15±4
	PSi_{APTES}	40±7
	THF, dark	53*
	air	81*
45	freezer	78*
	gels with TW20	86±5
	gels with TW80	92±6

* These data are reported without errors since they are the results of solution absorbance measurements and the errors are negligible.

4 Conclusions

In this thesis I investigated the use of two nanostructured materials as carriers for hydrophobic drugs. The interest in these molecules is related to the fact that an estimated 40% of approved active compounds and nearly 90% of the developmental pipeline drugs are poorly water soluble and they need special care both to design carriers able to load and release them, as well as strategies to overcome biological barriers and to render these ingredients bioavailable.
In this work I used BC and CFZ, which are two of the most difficult molecules to solubilize in water [210]. I chose BC for its truly non polar structure that permits to build a model system to investigate non polar interactions between the carrier surface and the drug. CFZ has been used as an alternative hydrophobic molecule: it is more chemically stable and slightly more soluble than BC in water.
In literature there is a plethora of publications on DDSs for hydrophobic molecules, but the large amount of different drug, types of carriers and release media make difficult a direct comparison between the results obtained in this thesis with those published. Regarding the choice of the release medium, the tests are often carried out in simulated fluids (whose composition varies from work to work [211]) and there are also researches in which the solubility in water is actually evaluated with a non negligible alcohol percentage [32]. I used either ETOH or water as release medium and I did not perform the experiments in buffers, since the solubility of the molecules (in particular when ionizable groups are present) and the carriers behaviour (e.g. gel swelling) are affected by pH and ionic strength, so that I decide not to introduce such parameters in these preliminary studies.

Initially I investigated the use of Psi as nanoporous carrier. This material is actively studied for DD applications as demonstrated by the bibliometric data reported in Fig. 4.1 showing the steady increase in both citations and publications. The interest in Psi as DDS arises from the several favourable characteristics it owns, in fact Psi:

1. can be prepared with huge specific area and porosity, thus it can load large amount of active compounds compared to its weight;

2. is biodegraded by the human body and shows no toxic effects;

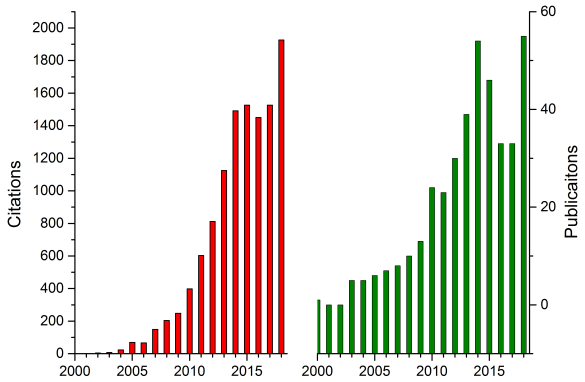

Fig. 4.1: Bibliometrics of Psi used as DDS.

3. its surface chemistry is (quite) well known and it allows for a large number of functionalization methods that are exploited to optimize its use and to render it compatible with the cargo;

4. might protect the loaded compounds against photo-degradation (as it highly absorbs UV-VIS radiation)

5. its pores can be closed (after the loading) to create core-shell devices preventing an untimely release of the cargo; furthermore the core-shell structure can be designed to obtain stimuli-responsive materials;

6. can be reduced to microparticles that are readily uptaken by human cells without adverse effects, thus the drugs can be effectively released within cells;

7. is a photoluminescent material, allowing the microparticles tracking inside the cells without the need of molecular tags.

There are plenty of nanoporous materials to which Psi can be compared to: from polymers to metal-organic-framework, from carbon to semiconductors based. Most of these materials either are based on fancy, not-too-common elements, or they are not bio-compatible (e.g. Materials Institute Lavoisier (MIL)-100 and MIL-101 have a huge surface area but contain toxic Cr ions). Thus, the comparison with porous carriers state-of-art for DD is then limited to silica-based material, as they are among the inorganic materials with the largest possibility to end up in real DD applications. Silica-based carrier have high chemical stability and good biocompatibility; their well known chemistry permits to tune their synthesis to fabricate well controlled and hierarchical structured porous carriers. The most commonly investigated are based on MCM-41, MCM-48, SBA-15, SBA-16 and on mesoporous silica nanopar-

ticles (MSN). After the seminal work on the use of MCM-41 to release ibuprofen [212], several of publications reported on the advances of using this platform for DD. Despite their different structures, in some works Psi and MSN achieve a similar drug loading efficiency of up to 30 % w/w, even when dealing with hydrophobic compounds [213, 214]. In other publications much larger loading capacities are reported (greater than 50% w/w) [215].
I loaded Psi with about 6 mg/g of drug per mass of Psi, that corresponds to 0.6% w/w, a value that is orders of magnitude lower with respect to that reported in the previous cited works. Actually, since I was interested in investigating the surface interactions between BC and the pores surface, the structure of Psi samples was not optimize to load large amount of drugs. Thus, a comparison with the state-of-art results of Psi DDs is not fair and an order of magnitude improvement is foreseen by simply optimizing the samples porosity and by using poorly soluble molecules with polar groups. Moreover, given the non polar structure of BC, the drug loading efficiency (that is often considered as one of the key parameter of DDSs) would not give a real indication of the Psi DDS performance. Furthermore, despite the large number of previously mentioned advantages, I discovered that Psi does not perform well as carrier for hydrophobic molecule such as BC. The experiments demonstrated that Psi stimulates BC degradation (rather than prevents it) even if its surface is carefully passivated. Although I could not unveil the chemical paths of these reactions, I observed that BC degradation is faster within Psi than in air or in liquid solvents. Probably, its chemical degradation is due to interface redox reactions that oxidize BC. Furthermore I noticed that, during the release experiments, BC tends to nucleate on Psi surface forming aggregates whose dissolution is much slower than the BC molecules release, thus they negatively impact on the control over the drug release. The nucleation event is not influenced by the chemical state of the Psi surface (as it happens on both hydride and oxide terminated samples), but it strongly depends on the details of the loading process. I hypothesized that these BC aggregates are the result of heterogeneous nucleation promoted by the large surface energy of silicon nanostructures. Since I found that the SDs of the release experiments precisely correlates with the aggregates formation, I proposed to use the SD as a method to determine the formation of heterogeneous nuclei on nanostructured surfaces, in alternative to the commonly used "induction time".

During the last year of the PhD, I started to investigate a different type of carrier: NC hydrogels. To the best of my knowledge, this is the first work on pure NC hydrogels for BC and CFZ release.
The use of NC for the release of hydrophobic compounds is an unexplored research field: there are only two publications on the use of modified CNC [216, 217] and no work has been published about pure NC hydrogels. Even if considering hydrogels in general (i.e. not necessarily made of NC) there are few publications about their

use to deliver hydrophobic therapeutics (only about 250 works are listed in "Scopus" database using the keywords "hydrogel" and "hydrophobic drug"); this is due to their high water content that hinders the encapsulation of poorly soluble molecules. To overcome this limit, the drug is often encapsulated in nanocarriers such as liposomes or polymer nanoparticles, which are then incorporated into hydrogels. This method is quite time consuming (some carriers preparations need up to few days [218]) and the release is seldom complete, possibly due to the entrapment of the nanocarriers within the hydrogels [219].

In this thesis I demonstrated that BC and CFZ can be loaded in NC hydrogels using a very fast method (i.e. ionotropic gelation). Initially I studied how CFZ is released from NC gels in ETOH. Although CFZ shows complex interactions with cations and its spectrum changes substantially upon solvation in salty solutions, the presence of a clear isosbestic point allowed me to quantify the amount of molecules released whatever the CFZ form present in solution. I obtained promising results as I was able to load up to 30% w/w (on dry basis) of CFZ within NC gels beads and to release it quantitatively. A similar CFZ loading efficiency has been obtained using hypromellose acetate succinate nanoparticles [27]. To note that drug loading capacities up to about 70% have been reported for non NC-based hydrogels loaded with curcumin and doxorubicin [220, 221]. Furthermore, I showed that NC hydrogels do not pose heavy issues to the release of lipophilic drugs, provided that a suitable surfactant (I used TW20 and TW80) mediates the molecule solvation and its subsequent release into aqueous media. The use of TW20 inside chitosan gels has been very recently reported to increase the curcumin solubility in simulated gastric medium [8] (there are no publications about CFZ relelase from hydrogels to compare with); the authors demonstrated that the release of curcumin increased from 0.21% to 54.85% by increasing the TW20 concentration. These results are difficult to compare with those obtained by me, both because the tested molecule, release medium and hydrogels composition are different and because I did not optimize the amount of CFZ loaded within the gels (which is in large excess) vs the amount of surfactant. Yet I demonstrated that, with the investigated gel compositions, the CFZ water solublity increases by 43 and 53 times using gels with TW20 and TW80, respectively. Finally, I tried to quantify the permeability of the CFZ released from NC gels through animal intestine membranes, but its quantity was below the instrumental detection limit; such characterization requires the design of *ad-hoc* experiments and might be a matter of further investigation.

Considering the good results obtained using CFZ, I investigated also the possibility to release BC from the same type of hydrogels. I found that it can be quantitatively released from gels in ETOH and, more interestingly, the BC solubility in water can be increased if it is released in aqueous media from hydrogels (reaching concentrations of 0.27 μg/mL and 0.43 μg/mL using TW20 and TW80, respectively). In fact control experiments made by direct dissolution of BC in water with surfactants produced no BC solvation. These results suggest that BC is efficiently solvated by

the surfactant within the hydrogel and before its release. Finally, I noticed that NC gels protect this delicate molecule from degradation much better than its storage in freezer or in organic solvent, making these carriers interesting for DD.
As far as I know, this is the first work that investigate hydrogels for CFZ release, while concerning BC hydrogels, only a BC nanoemulsion encapsulation in alginate-based hydrogel beads has been reported so far [222]. The authors demonstrate that the BC stability is enhanced when the nanoemulsion is encapsulated in 500 μm hydrogel beads, yet its biodisponibility decreases.
The results I obtained are very promising and encourage the NC hydrogel optimization to further improve the performance of this type of carrier. In particular a finer optimization of the hydrogels composition could lead to a quantitative drug release also in aqueous media as well as to increase the water solubility of these compounds, possibly to achieve results similar of those reported with other type of carriers. For instance, BC solubility can reach 100 μgr/mL encapsulating BC in lipid nanoparticles [223] and a further improvement can be obtained with BC emulsions (up to 0,3 mg/mL) [224]. Concerning CFZ, it has been reported that the use of hypromellose acetate succinate, lecithin and zein nanoparticles allows to increase from 50 to 90 times the CFZ solubility in gastric fluid [27]. Try to achieve these higher solubility values using the NC hydrogels can be fruitful since the fabrication of these carriers is easy, fast, cheap and does not require the use of complicated set-up.

Appendix

Homogeneous and heterogeneous nucleation

Nucleation is the first thermodynamically driven step that led to the formation of a new phase with lower free energy. There are two types of nucleation: in the homogeneous one the nucleus is formed in solution, while heterogeneous nucleation occurs at preferential sites, such as phase boundaries, surfaces or impurities. In this section I briefly report the thermodynamic basis of both homogeneous [225] and heterogeneous nucleations [226].

Homogeneous nucleation

According to the classical nucleation theory (that treats the microscopic nucleus as if it is a macroscopic droplet), the free energy (ΔG_{hom}) of the new phase can be written as the sum of a term proportional to its volume and a term proportional to its surface area. Considering a spherical nucleus with radius r, the free energy is given by:

$$\Delta G_{hom} = \frac{4}{3}\pi r^3 \Delta G_V + 4\pi r^2 \sigma \tag{4.1}$$

where ΔG_V is the difference in free energy per unit volume between the thermodynamic phase in which the nucleation is occurring and the nucleating phase, while σ is the surface tension of the interface between the particle and its surroundings. Since the first term is negative and scales with r^3, while the second is positive and proportional to r^2, for small r the surface term dominates, while at larger r the volume term is predominant and the total free energy becomes negative (see Fig. 4.2).
At an intermediate value of r, the so called "critical radius" (r*), the free energy goes through a maximum: the nucleus with a radius of r* is the least-probable, but the addition of new molecules decreases the overall system free energy. Thus, thermodynamic fluctuations (perhaps near or above supersaturation regimes) might promote the formation of stable nuclei.

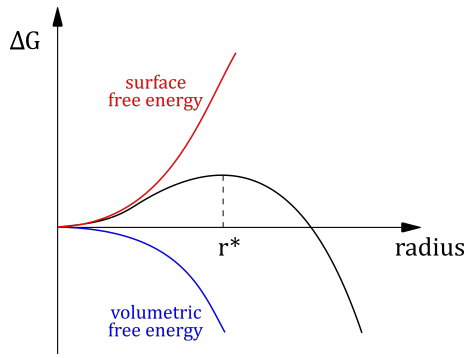

Fig. 4.2: Total free energy for homogeneous nucleation as a function of radius (black line): it is a sum of the volumetric (blue line) and the surface free energy (red line).

Heterogeneous nucleation

Heterogeneous nucleation is more common than homogeneous, since the nucleus formation on a surface often decreases the nucleation barrier with respect to homogeneous nucleation (see left panel in Fig. 4.3). As schematically depicted in Fig. 4.3 (right panel), in this case there are 3 different phases (α, β and δ) and all interactions α-β, α-δ and β-δ have to be considered.

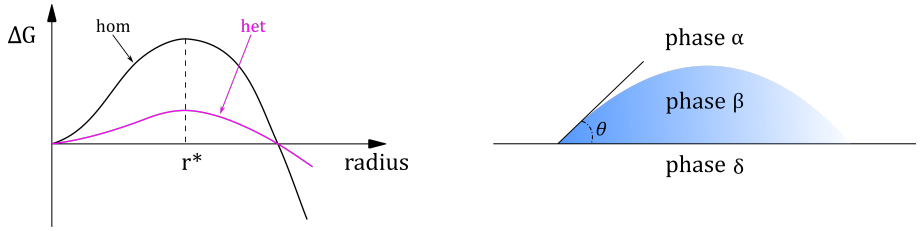

Fig. 4.3: Left panel reports comparison of total free energy as a function of particle radius between homogeneous (black line) and heterogeneous (magenta line) nucleation. Right panel shows a schematic of the three phases of interest for heterogeneous nucleation; θ is the contact angle.

Also in this case, the total free energy (ΔG_{het}) can be written as the sum of the volumetric free energy and the surface free energy:

$$\Delta G_{het}(r) = \frac{43}{\pi} r^3 \Delta G_V + A_{\alpha\beta}\gamma_{\alpha\beta} + A_{\beta\delta}(\gamma_{\beta\delta} - \gamma_{\alpha\delta}) \tag{4.2}$$

where ΔG_V is the difference in free energy per unit volume between the two phases, $A_{\alpha\beta}$ and $A_{\beta\delta}$ are the areas of $\alpha\beta$ and $\beta\delta$ interfaces, while $\gamma_{\alpha\beta}$, $\gamma_{\alpha\delta}$ and $\gamma_{\beta\delta}$ are the surface tensions of the interface between the different phases.

Eq. 4.2 can be written in terms of the contact angle θ:

$$\Delta G_{het}(r) = \frac{\pi r^3}{3}[2 - 3cos\theta + cos^3\theta]\Delta G_V + 2\pi r^2(1 - cos\theta)\gamma_{\alpha\beta} + \pi r^2 sin^2\theta(\gamma_{\beta\delta} - \gamma_{\alpha\delta}) \tag{4.3}$$

Considering a droplet on a flat surface with fixed volume, the term $\gamma_{\beta\delta} - \gamma_{\alpha\delta}$ is equal to $cos\theta \cdot \gamma_{\alpha\beta}$ and Eq. 4.3 becomes

$$\Delta G_{het}(r) = [\frac{4}{3}\pi r^3 \Delta G_V + 4\pi r^2 \gamma_{\alpha\beta}] \cdot [\frac{2 - 3cos\theta + cos^3\theta}{4}] \tag{4.4}$$

Since first term in parenthesis is the ΔG_{hom} for homogeneous nucleation, then Eq. 4.4 can be rewritten as

$$\Delta G_{het}(r) = \Delta G_{hom}(r) \cdot f(\theta) \tag{4.5}$$

where

$$f(\theta) = \frac{2 - 3cos\theta + cos^3\theta}{4} \tag{4.6}$$

To note that $0 \leq f(\theta) \leq 1$ and in particular if $\theta = \pi$ ($f(\theta) = 1$) there is no surface wetting, falling in the case of homogeneous nucleation and if $\theta = 0$ ($f(\theta) = 0$), the wetting is maximum and there is no barrier for nucleation. As for homogeneous nucleation, $\Delta G_{het}(r)$ should pass through to a maximum: the critical radius can be calculated by imposing $\frac{d\Delta G_{het}(r)}{dr} = 0$. According to this simple model, r* remains unchanged for heterogeneous and homogeneous nucleation, while the volume (due to the wetting angle affecting the shape of the nucleus) can be significantly less in the case of heterogeneous nucleation. In the theory described so far, the surface on which the nucleus grows is smooth; yet the critical size of the nucleus and the energy barrier for its formation are influenced by surface roughness (e.g. various studies demonstrate that fractal surfaces decrease the energy required for nucleation to occur [227, 228]). Despite it is generally accepted that the energy barrier for heterogeneous nucleation is lower with respect to homogeneous one, in many practical cases, the mechanisms by which heterogeneous agents promote the nucleation are still unclear [229].

BC degradation

During the thesis work I observe that, despite stored as powder in freezer and in the dark, BC quickly degrades. In the following sections I report the analyses performed to try to investigate its degradation. Since I note a decrease of its absorption coefficient with time (as reported in Fig. 4.4), I use ϵ to indicate the extent of degradation.

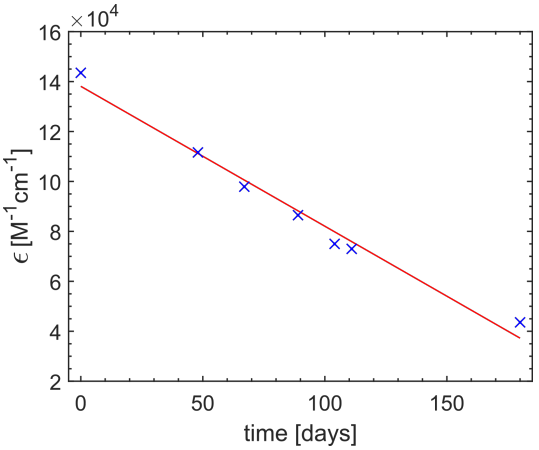

Fig. 4.4: BC absorption coefficient as a function of time, fitted with a linear curve (red line).

The data in Fig. 4.4 are obtained by dissolving a known amount of BC in THF and diluting 10 μl of this solution in 3 ml of ETOH; from the values of the absorbance maximum (at 452 nm) I calculate the ϵ using the well known Lambert-Beer relation.

In the first section I report the analyses performed on BC powders with different degradation extent, while in the second section I show the results of BC degradation in two of the most used solvent for BC extraction (i.e. $CHCl_3$ and THF).

BC stored as powder

I try to investigate BC powders with different degradation extent relaying on UV-VIS, FTIR, RAMAN, NMR, HPLC and MALDI-TOF analyses. Despite the determination of the products and reactions paths to them are out of the scope of this work, the acquired data support the conclusions reported in [230].
NMR and HPLC analyses have been done in collaboration with Prof. Graziano Guella at the Bioorganic Chemistry Laboratory of the Department of Physics, while MALDI-TOF in collaboration with Prof. Giorgio Arrigoni at the Department of Biomedical Sciences of the University of Padova.

UV-VIS analysis Fig. 4.5 show the UV-VIS spectra of BC in ETOH (0.009 mg/mL) with ϵ=144000, 30000 and 3500 L·mol^{-1}cm^{-1}. I exclude that the strong absorbance decrease is due to the break of the π-coniugated BC structure, otherwise absorbance spectra would shift to lower wavelength, as predicted by the empirical Fieser-Kuhn rules for conjugated polyenes [161].

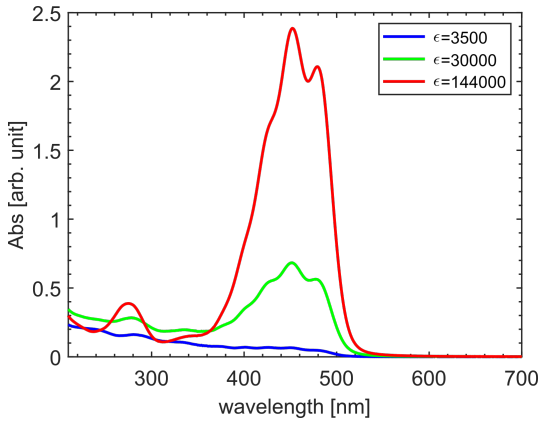

Fig. 4.5: UV-VIS spectra of BC at different degradation extent.

FTIR analysis The FTIR spectra of BC powder with ϵ=144000 and 3500 L·mol^{-1}cm^{-1} are reported in Fig. 4.6. In the FTIR spectra of degraded BC there is a strong absorption band around 3500 cm^{-1} (consistent with the presence of hydroxyl group). In the C-H stretching range (2800-3000 cm^{-1}) and fingerprint region the peaks in the degraded samples are very broad, hindering a fine spectral analysis. However, in the degraded BC a signal at 1728 cm^{-1} is evident and it is compatible with the C=O stretching.

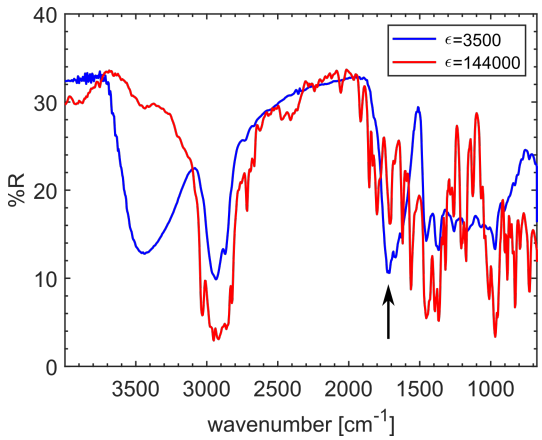

Fig. 4.6: FTIR spectra of BC; the black arrow indicates the peak compatible with the C=O stretching.

RAMAN analysis I acquire the Raman spectra of BC powder with ϵ=144000 and 3500 L·mol^{-1}cm^{-1}; despite their very different extent of degradation, the acquired

Raman spectra show no substantial differences (see Fig. 4.7). As reported in [231–233], the dominant Raman modes of carotenoids are in the range 800-1800 cm^{-1}: the peaks detected at 1008, 1156 and 1515 cm^{-1} can be assigned to in-plane rocking modes of CH_3 groups attached to the polyene chain coupled with C-C bonds, stretching vibrations of C-C and C=C in the polyene chain, respectively. Concerning the sample with ϵ=3500 $L{\cdot}mol^{-1}cm^{-1}$, the absence of the peak associated to the vibration of the C=O bond around 1700 cm^{-1} is probably due to the fact that its Raman intensity is below the detection limit.

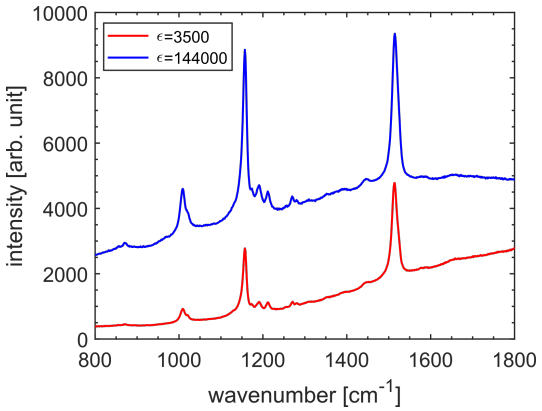

Fig. 4.7: Raw Raman spectra of BC.

NMR analysis The NMR spectra (normalized with respect to the $CHCl_3$ signal) of 20 mM BC solution in $CDCl_3$ using BC with ϵ=144000, 30000 and 3500 $L{\cdot}mol^{-1}cm^{-1}$ are reported in Fig. 4.8. Degraded BC spectra show very broad signals, while sharp peaks are present in the spectra of unaltered BC. This inhomogeneous broadening can be due to oligomerization/polymerization reactions among BC molecules. The signals at 9.5 (black arrow in Fig. 4.8) and around 8 ppm (magenta arrow in Fig. 4.8) are present only in the degraded BC and can be assign to aldehydes (-H-C=O) and aromatic groups respectively. The aldehydes groups can be formed only in two cases: either due to the oxidation of a methyl groups or by the molecule fragmentation. I speculate that aromatic rings form in the centre of the polyenic chain, as the double bonds rearranged to form them. In the range 5-3 ppm (see inset in Fig. 4.8) there are signals that can be associated to protons that are bound to C sp^3 linked to heteroatoms (probably oxygen).

HPLC analysis HPLC analysis has been performed using BC with ϵ=144000, 30000 and 3500 $L{\cdot}mol^{-1}cm^{-1}$; the data acquired in the VIS region (at 450 nm) are reported in Fig. 4.9A, while Fig. 4.9B shows the analysis in the UV range (at 245 nm).
The HPLC spectra acquired in the VIS range show BC signals at elution time of about 40 min (see inset in Fig. 4.9A), whose intensities are strongly decreased with increasing BC degradation (as already demonstrated by UV-VIS absorption). The peak at 41 min is assigned to Cis-BC, while that at 42 min to Trans-BC; the peak

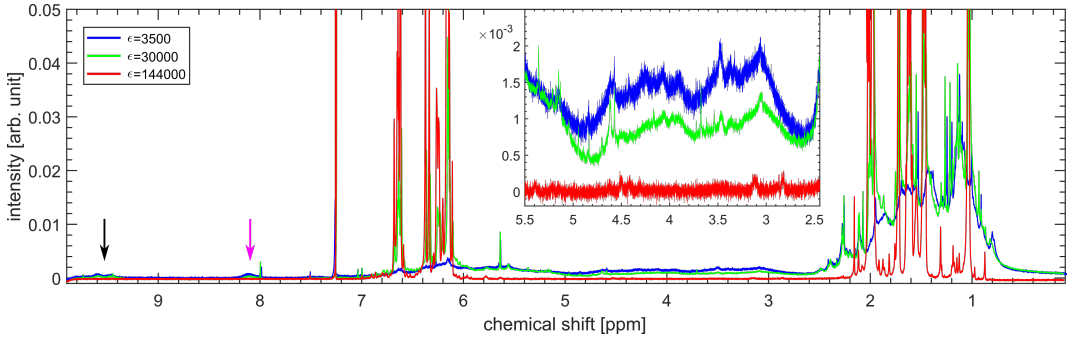

Fig. 4.8: NMR spectra of BC in $CDCl_3$.

between these two that is present in the non-degraded BC can be assigned to BC isomers.

Concerning the analysis in the UV range, in addition to the BC signals at elution time of about 40 min, I observe that for short times (see magenta arrow in Fig. 4.9B), the UV signal is greater for the degraded BC (the highest peak around 1 min is due to the solvent used for the elution). Since the analysis has been performed with an inverse phase chromatographic column, these signals can be due to either oxidised species or BC fragments.

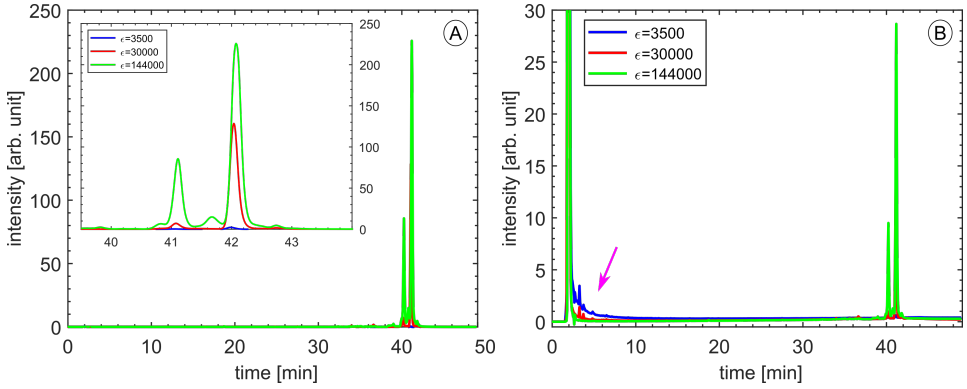

Fig. 4.9: HPLC spectra of BC acquired in A) VIS and B) UV range.

MALDI-TOF analysis BC with ϵ=144000 (red lines in the following figures) and ϵ=30000 (blue lines in the following figures) L·mol^{-1}cm^{-1} have been analysed with a MALDI-TOF spectrometer, both in positive and negative mode, by dissolving the BC powder in 1:1=H_2O:acetonitrile, 0.1% trifluoroacetic acid.

Fig. 4.10 reports the data acquired in negative mode: a peak at 535.4 m/z ([BC-H]$^-$) is present in both spectra; in the degraded BC spectrum appears a peak at 551.3 m/z, that is compatible to the oxygen presence ([M-H+O]$^-$).

Concerning the analysis in positive mode (see Fig. 4.11), I note that at low laser fluence only non-degraded BC can be detected (spectrum reported in Fig. 4.11A). By increasing the laser intensity, some peaks appear in the low mass range, as shown in Fig. 4.11B. These signals can be due to BC-fragments, probably generated

by the laser fragmentation of some BC oligomers during the MALDI-TOF analysis. At these laser fluence the degraded BC can be detected, too; yet in this case the intensity of the signals in the low mass range is of the same order of magnitude of that of BC itself (see Fig. 4.11C). Fig. 4.12 reports the zoom around 536 m/z for non-degraded and degraded BC. The highest peak is at 536.4 m/z and can be associated to the radical cation $[BC]^+$. In BC-degraded spectrum other peaks appear that can be assigned to oxidised BC species($[M\text{-}H+O]^+$, $[M\text{-}H+2O]^+$, $[M\text{-}H+3O]^+$ and $[M\text{-}H+4O]^+$).

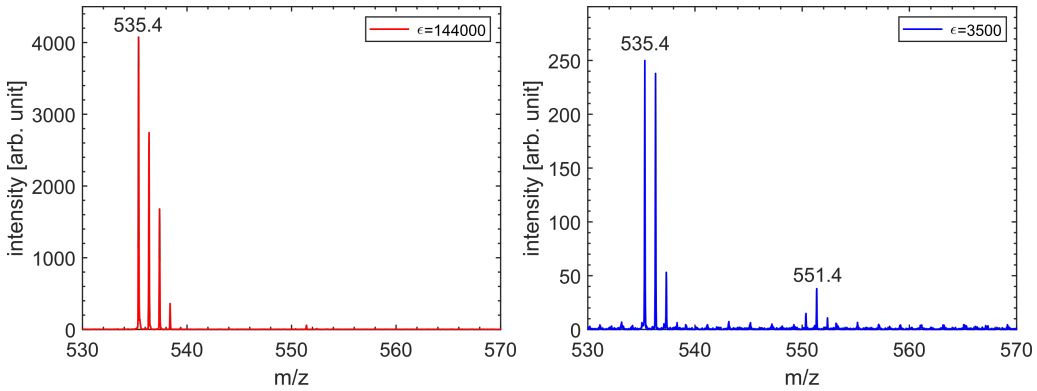

Fig. 4.10: MALDI-TOF spectra of BC with ϵ=144000 (left panel) and 3500 (right panel) L·mol^{-1}cm^{-1} acquired in negative mode.

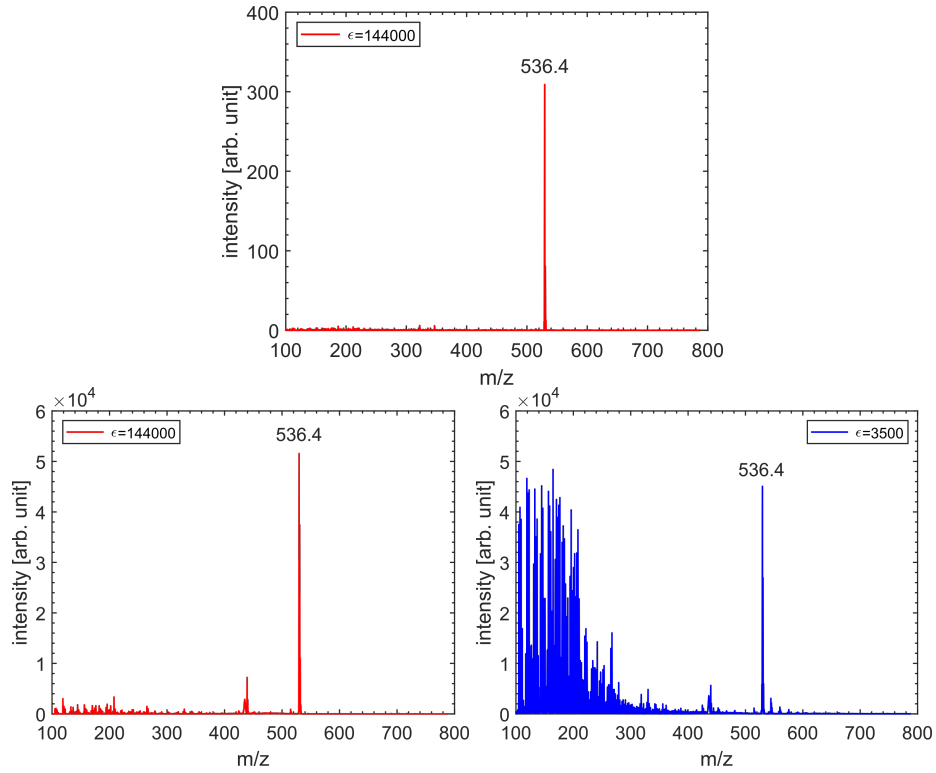

Fig. 4.11: MALDI-TOF spectra acquired in positive mode of BC with ϵ=144000 L·mol^{-1}cm^{-1} at low laser fluence (upper panel), at high laser fluence (bottom left panel) and of BC with ϵ=3500 L·mol^{-1}cm^{-1} at high laser fluence (bottom right panel).

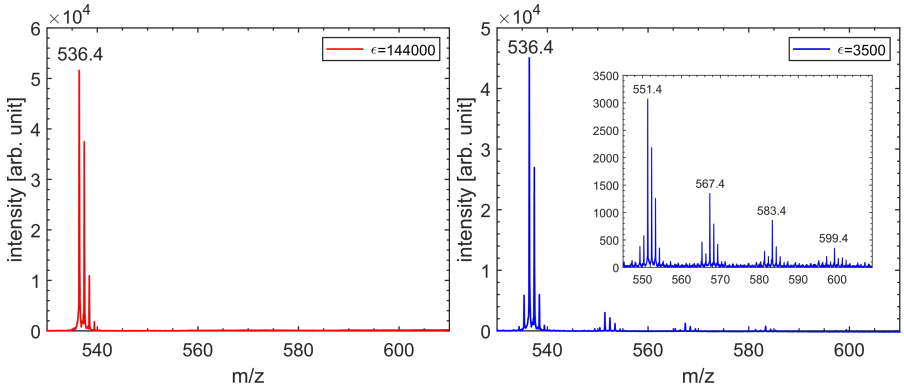

Fig. 4.12: Zoom of MALDI-TOF spectra of BC with ϵ=144000 (left panel) and 3500 (right panel) L·mol^{-1}cm^{-1} acquired in positive mode.

BC dissolved in organic solvents

One of the main problem I face during the analysis of released drugs is the tiny amount of molecules available. In a typical release experiment from Psi, I recover few tens of nmoles of compound, thus the interactions and secondary reaction of these molecules with solvent impurities become relevant. Here below I show the results obtained by dissolving BC in $CDCl_3$ and THF.

BC dissolved in $CHCl_3$ I prepare a 1.5 mg/mL BC solution in $CDCl_3$ stabilised with silver wires (stab-$CDCl_3$) (referred to "sol. X") and I dilute 5 μL of it in 2 mL of both $CDCl_3$ and stab-$CDCl_3$. The BC spectrum is clearly visible when I dilute "sol. X" in stab-CDCl3 (see Fig. 4.13, blue line), yet no signal is present in the BC region performing the dilution in $CDCl_3$ (see Fig. 4.13, red line).

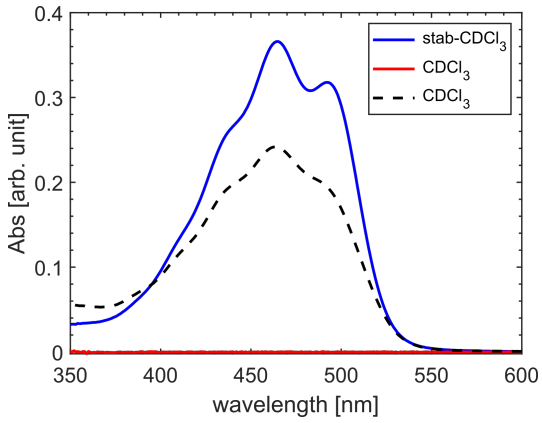

Fig. 4.13: Absorption spectra of 5 μL of sol. X in 2 mL of stab-$CDCl_3$ (blue line) and $CDCl_3$ (red line); absorption spectra of 30 μL of sol. X in 2 mL of $CDCl_3$ (black-dotted line).

I add 5 μL at a time of sol. X to the latter BC solution: no BC absorption spectrum has been observed until 30 μL of sol. X are added in the 2 mL (spectrum with black dotted line in Fig. 4.13). According to this titration and hypothesizing that the

stoichiometry of the reaction between impurities and BC is 1:1, I estimate that the concentration of reacting impurities in $CDCl_3$ is 0.045 mM, corresponding to 3.6 ppm.
Since it has been reported that trace amounts of HCl or free Cl dissolved in $CDCl_3$ may induced BC polymerization [10], I perform NMR analysis to understand whether BC polymers are present. This measurement requires BC concentration higher than those used in the previous experiments to obtain a good S/N ratio. Thus, I concentrate a 45 μM BC solution in $CDCl_3$ up to 2.5 mM and the acquired spectrum is reported in Fig. 4.14. There is an evident peak broadening, suggesting that BC oligomerization/polymerization is occurred.

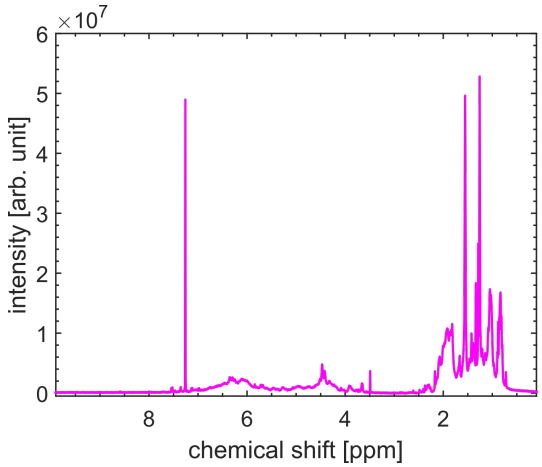

Fig. 4.14: NMR spectra of BC in $CDCl_3$.

BC dissolved in THF Similarly to the results presented in the above, I check the effects that oxidant impurities in anhydrous THF have on BC degradation.
THF is known to contain peroxides species and to quantify their amount I prepare a 0.01 M aqueous solution of KI, that I add to the same amount of both THF just opened (THF_{new}) and opened few weeks before the analysis (THF_{old}). The acquired absorption spectra are reported in Fig. 4.15 (left panel). The relative amount of peroxides in the solutions can be estimated from the ratio between the intensities at 354 nm, since this peak is due to the I_2 formed when I^- reacts with the peroxides and I find that the peroxides concentration in THF_{old} is 5 times that in THF_{new}.
I dissolved BC (ϵ=144000 L·mol^{-1}cm^{-1}) in THF_{old} and THF_{new} and I do not observe any variation in the BC absorbance within 24 h. Yet, when degraded-BC is dissolved in THF_{new}, I note a decrease in absorbance within 24 h (as reported in the right panel of Fig. 4.15). The facts that non-degraded BC does not change its spectral characteristics, neither in THF_{old} nor in THF_{old}, while degraded BC is further degraded even in THF_{new} suggest that the BC degradation in THF might occur through radical reactions: once the process is started, it is quicker and possibly catalysed by the peroxides present in solution.

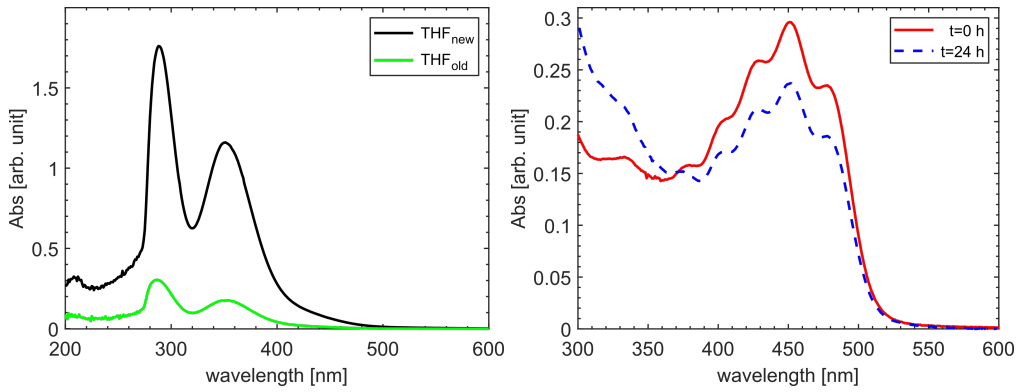

Fig. 4.15: Left panel reports the absorption spectra of THF_{new} (black line) and THF_{old} (green line) dissolved in 0.01 M aqueous solution of KI. Right panel shows the absorption spectra of BC with ϵ=12000 L·mol^{-1}cm^{-1} dissolved in THF_{new} at time t=0 (red continuous line) and after 24 h (blue dotted line): the value of the absorbance maximum is decreased by 20%.

Methods

UV-VIS analysis has been performed on a Varian CARY-100 UV-VIS Spectrophotometer, with spectral resolution of 1 nm; all the spectra have been acquired using a quartz cuvette and baseline corrected against the same cuvette filled with the solvent.

ζ-potential measurements have been performed on a Zetasizer Nano ZS instrument (Malvern Instruments, Worcestershire, UK) equipped with a 633 nm He-Ne and a universal dip cell (ZEN1002). The ζ-potential has been estimated by applying the Smoluchowski model and by using refractive index and absorbance values of 2 and 0.2, respectively.

FTIR spectra have been acquired on a micro-FTIR Nicolet iN10 instrument equipped with a liquid nitrogen cooled detector. 300 μm^2 of the samples have been scanned in %R mode in the range 700-4000 cm^{-1} with a 4 cm^{-1} spectral resolution.

RAMAN measurements have been performed on a LabRAM Aramis equipped with a 532 nm laser and a 1800 lines/mm grating. Each spectrum has been acquired by summing up 30 acquisitions, each one integrating the signal for 2 seconds.

HPLC analysis has been carried out on Agilent 1100 (Agilent Technologies, USA) by injecting 10 μL of sample onto an RP-8 column (Agilent ZORBAX Eclipse XDB-C8) and then detecting the eluted analytes with a photodiode array detector (Agilent 1220 Series, Agilent Technologies, Santa Clara, USA). Analytical separation has been achieved by using a gradient program (constant flow 0.8 mL/min) starting with a 65:35 ratio of mobile phases A (70:30 CH_3OH/H_2O containing 12 mM ammonium acetate) and B (CH_3OH with12 mM ammonium acetate) that has been gradually increased to 100% B over 40 min.

NMR measurements (NMR ^1H, 400 MHz) have been recorded in stab-$CDCl_3$ at 300 K on a Bruker Avance 400 MHz NMR spectrometer, using a 5 mm BBI probe with

90° proton pulse length of 8.7 μs at a transmission power of 0 db and equipped with pulsed gradient field utility. The chemical shift scale has been calibrated on the residual proton signal of $CDCl_3$ at 7.26 ppm.

MALDI-TOF analyisis has been performed in both positive and negative mode on a MALDI-TOF/TOF 4800 AB Sciex, equipped with a Nd:YAG (355 nm) 200 Hz laser; the extraction fields have been set at 20kV and the delay extraction fixed at 400 ns. Each spectrum is the accumulation of 1500 spectra acquired in 30 different randomly selected spot areas.

List of publications

Publications related to this thesis work:

- A. Lion, N. Laidani, P. Bettotti, C. Piotto, G. Pepponi, M. Barozzi, M. Scarpa, "Angle resolved XPS for selective characterization of internal and external surface of porous silicon", Applied Surface Science, 406, 144-149 (2017).

- C. Piotto, G. Guella, P. Bettotti, "Fluorinated surfaces: smart substrates for matrix-free laser desorption ionization", Rapid Communications in Mass Spectrometry 31, 1228-1230 (2017).

- C. Piotto, P. Bettotti, "Porous Silicon: From Optical Sensor to Drug Delivery System", in "Submicron Porous Materials" (Bettotti ed.), Spinger, 217-252 (2017).

- C.Piotto, P. Bettotti, "Surfactant mediated clofazimine release from nanocellulose-hydrogels", submitted.

- C.Piotto, P. Bettotti, "Role of surface heterogeneous nucleation on nanoporous drug delivery systems", submitted.

- C.Piotto, P. Bettotti, "Nanocellulose hydrogels self-emulsifying drug delivery system for hydrophobic molecules", in preparation.

Other publications:

- G. Daaboul, P. Gagni, L. Benussi, P. Bettotti, M. Ciani, M. Cretich, R. Ghidoni, Y. Ayca, C. Piotto, D. Prosperi, B. Santini, S. M. Unlu, M. Chiari, "Digital detection of exosomes by interferometric imaging", Scientific Reports, 6 (2016).

- L. Cenci, C. Piotto, P. Bettotti, A. M. Bossi, "Study on molecularly imprinted nanoparticle modified microplates for pseudo-ELISA assays", Talanta, 178, 772-779 (2018).

- L. Cenci, R. Tatti, R. Tognato, E. Ambrosi, C. Piotto, A. M. Bossi, "Synthesis and characterization of peptide-imprinted nanogels of controllable size and affinity", European Polymer Journal, Available online (August 2018).

- P. Gagni, A, Romanato, G. Bergamaschi, P. Bettotti, R. Vanna, C. Piotto, C. Morasso, M. Chiari, M. Cretich, A. Gori, "A Self-assembling Peptide Hydrogel for Ultrarapid 3D Bioassays", submitted.

- L. Lunelli, F. Caradonna, C. Potrich, C. Piotto, P. Bettotti, L. Vanzetti, C. Pederzolli, G. Guella, "A new silanizing agent tailored to surface bio-functionalization", submitted.

Bibliography

[1] Anna Lion, Nadhira Laidani, Paolo Bettotti, et al. „Angle resolved XPS for selective characterization of internal and external surface of porous silicon“. In: *Applied Surface Science* 406 (2017), pp. 144–149 (cit. on p. 2).

[2] Chia-Chen Wu and Michael J Sailor. „Selective functionalization of the internal and the external surfaces of mesoporous silicon by liquid masking“. In: *ACS nano* 7.4 (2013), pp. 3158–3167 (cit. on p. 2).

[3] De-Xiang Zhang, Chiaki Yoshikawa, Nicholas G. Welch, et al. „Spatially controlled surface modification of porous silicon for sustained drug delivery applications“. In: *Scientific reports* 9.1 (2019), p. 1367 (cit. on p. 2).

[4] N. Seedher and M. Kanojia. „Micellar solubilization of some poorly soluble antidiabetic drugs: A technical note“. In: *AAPS PharmSciTech* 9.2 (2008), pp. 431–436 (cit. on p. 2).

[5] P.A. Bhat, A.A. Dar, and G.M. Rather. „Solubilization capabilities of some cationic, anionic, and nonionic surfactants toward the poorly water-soluble antibiotic drug erythromycin“. In: *Journal of Chemical and Engineering Data* 53.6 (2008), pp. 1271–1277 (cit. on p. 2).

[6] S.D. Bhattamishra and R.K. Padhy. „Estimation of Ibuprofen solubilization in cationic and anionic surfactant media: Application of micelle binding model“. In: *Indian Journal of Chemical Technology* 16.5 (2009), pp. 426–430 (cit. on p. 2).

[7] Joan R O'Reilly, Owen I Corrigan, and Caitriona M O'Driscoll. „The effect of simple micellar systems on the solubility and intestinal absorption of clofazimine (B663) in the anaesthetised rat“. In: *International journal of pharmaceutics* 105.2 (1994), pp. 137–146 (cit. on p. 2).

[8] Thennakoon M Sampath Udeni Gunathilake, Yern Chee Ching, Cheng Hock Chuah, et al. „Influence of a nonionic surfactant on curcumin delivery of nanocellulose reinforced chitosan hydrogel“. In: *International journal of biological macromolecules* 118 (2018), pp. 1055–1064 (cit. on pp. 2, 82).

[9] Yuan Yuan, Yanxiang Gao, Like Mao, and Jian Zhao. „Optimisation of conditions for the preparation of β-carotene nanoemulsions using response surface methodology“. In: *Food chemistry* 107.3 (2008), pp. 1300–1306 (cit. on p. 3).

[10] T Treszczanowicz, T Kasprzycka-Guttman, D Cieślak, and AJ Treszczanowicz. „Distribution coefficient of β-carotene between an organic solvent and water“. In: *Journal of Chemical & Engineering Data* 43.4 (1998), pp. 632–634 (cit. on pp. 3, 94).

[11]Patrick Borel, P Grolier, M Armand, et al. „Carotenoids in biological emulsions: solubility, surface-to-core distribution, and release from lipid droplets.“ In: *Journal of lipid research* 37.2 (1996), pp. 250–261 (cit. on p. 3).

[12]Rachel E. Kopec, Jessica L. Cooperstone, Morgan J. Cichon, and Steven J. Schwartz. „Analysis Methods of Carotenoids“. In: *Analysis of Antioxidant-Rich Phytochemicals*. Ed. by Zhimin Xu and Luke R. Howard. Wiley, 2012, pp. 105–148 (cit. on p. 3).

[13]Paola Palozza, Rita Muzzalupo, Sonia Trombino, Ambra Valdannini, and Nevio Picci. „Solubilization and stabilization of β-carotene in niosomes: delivery to cultured cells“. In: *Chemistry and Physics of lipids* 139.1 (2006), pp. 32–42 (cit. on pp. 3, 11).

[14]Christoph Nacke and Jens Schrader. „Micelle based delivery of carotenoid substrates for enzymatic conversion in aqueous media“. In: *Journal of Molecular Catalysis B: Enzymatic* 77 (2012), pp. 67–73 (cit. on p. 3).

[15]Dale A Cooper, D Ronald Webb, and John C Peters. „Evaluation of the potential for olestra to affect the availability of dietary phytochemicals“. In: *The Journal of nutrition* 127.8 (1997), pp. 1699–1709 (cit. on p. 3).

[16]Sonja Köhn, Henrike Kolbe, Michael Korger, et al. „Aggregation and interface behaviour of carotenoids“. In: *carotenoids*. Springer, 2008, pp. 53–98 (cit. on p. 3).

[17]L Zabodalova, T Ishchenko, N Skvortcova, D Baranenko, and V Chernjavskij. „Liposomal beta-carotene as a functional additive in dairy products“. In: *ISSN 1406-894X* 12.3 (2009), pp. 825–834 (cit. on p. 3).

[18]Ana Belščak-Cvitanović, Arijana Bušić, Lidija Barišić, et al. „Emulsion templated microencapsulation of dandelion (Taraxacum officinale L.) polyphenols and β-carotene by ionotropic gelation of alginate and pectin“. In: *Food hydrocolloids* 57 (2016), pp. 139–152 (cit. on p. 3).

[19]S Ariviani, S Anggrahini, S Naruki, and S Raharjo. „Characterization and chemical stability evaluation of β-carotene microemulsions prepared by spontaneous emulsification method using VCO and palm oil as oil phase.“ In: *International food research journal* 22.6 (2015) (cit. on p. 3).

[20]Jiajia Rao, Eric Andrew Decker, Hang Xiao, and David Julian McClements. „Nutraceutical nanoemulsions: influence of carrier oil composition (digestible versus indigestible oil) on β-carotene bioavailability“. In: *Journal of the Science of Food and Agriculture* 93.13 (2013), pp. 3175–3183 (cit. on p. 3).

[21]Boon-Seang Chu, Sosaku Ichikawa, Sumiyo Kanafusa, and Mitsutoshi Nakajima. „Preparation of protein-stabilized β-carotene nanodispersions by emulsification–evaporation method“. In: *Journal of the American Oil Chemists' Society* 84.11 (2007), pp. 1053–1062 (cit. on p. 3).

[22]Mandeep Kaur, Mohit Bawa, and Minni Singh. „β–CAROTENE-β–CYCLODEXTRIN INCLUSION COMPLEX: TOWARDS ENHANCED AQUEOUS SOLUBILITY“. In: *Journal of Global Biosciences* 5.2 (2016), pp. 3665–3675 (cit. on p. 3).

[23]Dhanashree Hemant Surve, Atish Tulsiram Paul, and Anil B Jindal. „Nanotechnology Based Delivery of Nutraceuticals“. In: *Environmental Nanotechnology*. Springer, 2019, pp. 63–107 (cit. on p. 3).

[24]Global Alliance for TB Drug Development (TB Alliance). „Clofazimine-A Review“. In: *Tuberculosis* 88 (2008), pp. 96–99 (cit. on pp. 3, 68).

[25] Marc-Alexandre Schott, Martine Domurado, Laurent Leclercq, Christel Barbaud, and Dominique Domurado. „Solubilization of water-insoluble drugs due to random amphiphilic and degradable poly (dimethylmalic acid) derivatives“. In: *Biomacromolecules* 14.6 (2013), pp. 1936–1944 (cit. on pp. 3, 62, 64).

[26] Pauric Bannigan, Edel Durack, Conor Madden, Matteo Lusi, and Sarah P Hudson. „Role of Biorelevant Dissolution Media in the Selection of Optimal Salt Forms of Oral Drugs: Maximizing the Gastrointestinal Solubility and in Vitro Activity of the Antimicrobial Molecule, Clofazimine“. In: *ACS Omega* 2.12 (2017), pp. 8969–8981 (cit. on p. 3).

[27] Yingyue Zhang, Jie Feng, Simon A McManus, et al. „Design and Solidification of Fast-Releasing Clofazimine Nanoparticles for Treatment of Cryptosporidiosis“. In: *Molecular pharmaceutics* 14.10 (2017), pp. 3480–3488 (cit. on pp. 3, 82, 83).

[28] Lorenzo Angiolini, Sabrina Valetti, Boiko Cohen, Adam Feiler, and Abderrazzak Douhal. „Fluorescence imaging of antibiotic clofazimine encapsulated within mesoporous silica particle carriers: relevance to drug delivery and the effect on its release kinetics“. In: *Physical Chemistry Chemical Physics* 20.17 (2018), pp. 11899–11911 (cit. on p. 3).

[29] Robert O'connor, JF O'sullivan, and Richard O'kennedy. „The pharmacology, metabolism, and chemistry of clofazimine“. In: *Drug metabolism reviews* 27.4 (1995), pp. 591–614 (cit. on p. 3).

[30] Jason Baik and Gus R Rosania. „Macrophages sequester clofazimine in an intracellular liquid crystal-like supramolecular organization“. In: *PloS one* 7.10 (2012), e47494 (cit. on p. 3).

[31] Jason Baik, Kathleen A Stringer, Gerta Mane, and Gus R Rosania. „Multiscale distribution and bioaccumulation analysis of clofazimine reveals a massive immune system-mediated xenobiotic sequestration response“. In: *Antimicrobial agents and chemotherapy* 57.3 (2013), pp. 1218–1230 (cit. on p. 3).

[32] Geetha Bolla and Ashwini Nangia. „Clofazimine mesylate: a high solubility stable salt“. In: *Crystal Growth & Design* 12.12 (2012), pp. 6250–6259 (cit. on pp. 3, 79).

[33] VB Patel and AN Misra. „Encapsulation and stability of clofazimine liposomes“. In: *Journal of microencapsulation* 16.3 (1999), pp. 357–367 (cit. on p. 3).

[34] Reeta T Mehta. „Liposome encapsulation of clofazimine reduces toxicity in vitro and in vivo and improves therapeutic efficacy in the beige mouse model of disseminated Mycobacterium avium-M. intracellulare complex infection.“ In: *Antimicrobial agents and chemotherapy* 40.8 (1996), pp. 1893–1902 (cit. on p. 3).

[35] Youssef Bakkour, Vincent Darcos, Fanny Coumes, Suming Li, and Jean Coudane. „Brush-like amphiphilic copolymers based on polylactide and poly (ethylene glycol): Synthesis, self-assembly and evaluation as drug carrier“. In: *Polymer* 54.7 (2013), pp. 1746–1754 (cit. on p. 3).

[36] Vincent Darcos, Sarah El Habnouni, Benjamin Nottelet, Abdeslam El Ghzaoui, and Jean Coudane. „Well-defined PCL-graft-PDMAEMA prepared by ring-opening polymerisation and click chemistry“. In: *Polymer Chemistry* 1.3 (2010), pp. 280–282 (cit. on p. 3).

[37] Isam Ismail Salem, Gerhard Steffan, and Nejat Düzgünes. „Efficacy of clofazimine–modified cyclodextrin against Mycobacterium avium complex in human macrophages“. In: *International journal of pharmaceutics* 260.1 (2003), pp. 105–114 (cit. on p. 3).

[38] Ajit S Narang and Anand K Srivastava. „Evaluation of solid dispersions of clofazimine“. In: *Drug development and industrial pharmacy* 28.8 (2002), pp. 1001–1013 (cit. on p. 3).

[39] Khin Yin Win and Si-Shen Feng. „Effects of particle size and surface coating on cellular uptake of polymeric nanoparticles for oral delivery of anticancer drugs“. In: *Biomaterials* 26.15 (2005), pp. 2713–2722 (cit. on pp. 4, 8, 9).

[40] Shilpa Sant, Sarah L Tao, Omar Z Fisher, et al. „Microfabrication technologies for oral drug delivery“. In: *Advanced drug delivery reviews* 64.6 (2012), pp. 496–507 (cit. on p. 4).

[41] Kyeongsoon Park, Ick Chan Kwon, and Kinam Park. „Oral protein delivery: Current status and future prospect“. In: *Reactive and Functional Polymers* 71.3 (2011), pp. 280–287 (cit. on p. 4).

[42] Katsuhiko Ariga, Yuri M Lvov, Kohsaku Kawakami, Qingmin Ji, and Jonathan P Hill. „Layer-by-layer self-assembled shells for drug delivery“. In: *Advanced drug delivery reviews* 63.9 (2011), pp. 762–771 (cit. on p. 4).

[43] Kavita Khanvilkar, Maureen D Donovan, and Douglas R Flanagan. „Drug transfer through mucus“. In: *Advanced drug delivery reviews* 48.2-3 (2001), pp. 173–193 (cit. on p. 4).

[44] Zheng Cai, Yan Wang, Li-Jun Zhu, and Zhong-Qiu Liu. „Nanocarriers: a general strategy for enhancement of oral bioavailability of poorly absorbed or pre-systemically metabolized drugs“. In: *Current Drug Metabolism* 11.2 (2010), pp. 197–207 (cit. on pp. 4, 8).

[45] M Hayashi, T Sakai, Y Hasegawa, et al. „Physiological mechanism for enhancement of paracellular drug transport“. In: *Journal of controlled release* 62.1-2 (1999), pp. 141–148 (cit. on p. 4).

[46] Thorsteinn Loftsson and Marcus E Brewster. „Pharmaceutical applications of cyclodextrins: basic science and product development“. In: *Journal of pharmacy and pharmacology* 62.11 (2010), pp. 1607–1621 (cit. on p. 5).

[47] Natalie L Trevaskis, William N Charman, and Christopher JH Porter. „Lipid-based delivery systems and intestinal lymphatic drug transport: a mechanistic update“. In: *Advanced drug delivery reviews* 60.6 (2008), pp. 702–716 (cit. on p. 5).

[48] Abu TM Serajuddin. „Salt formation to improve drug solubility“. In: *Advanced drug delivery reviews* 59.7 (2007), pp. 603–616 (cit. on p. 5).

[49] Ruchi Tiwari, Gaurav Tiwari, Birendra Srivastava, and Awani K Rai. „Solid dispersions: an overview to modify bioavailability of poorly water soluble drugs“. In: *International Journal of PharmTech Research* 1.4 (2009), pp. 1338–1349 (cit. on p. 6).

[50] Colin R Gardner, Christopher T Walsh, and Örn Almarsson. „Drugs as materials: valuing physical form in drug discovery“. In: *Nature Reviews Drug Discovery* 3.11 (2004), p. 926 (cit. on p. 6).

[51] Naga K Duggirala, Miranda L Perry, Örn Almarsson, and Michael J Zaworotko. „Pharmaceutical cocrystals: along the path to improved medicines“. In: *Chemical Communications* 52.4 (2016), pp. 640–655 (cit. on pp. 6, 7).

[52]Prakash Khadka, Jieun Ro, Hyeongmin Kim, et al. „Pharmaceutical particle technologies: An approach to improve drug solubility, dissolution and bioavailability“. In: *Asian journal of pharmaceutical sciences* 9.6 (2014), pp. 304–316 (cit. on p. 7).

[53]CM Keck, S Kobierski, R Mauludin, and RH Müller. „Novel Top-Down Technologies: Effective Production of Ultra-Fine Drug Nanocrystals“. In: *Drug Delivery Strategies for Poorly Water-Soluble Drugs*. Ed. by D Douroumis and A Fahr. Wiley, 2013, pp. 247–263 (cit. on p. 7).

[54]Anshu Sharma and CP Jain. „Solid dispersion: A promising technique to enhance solubility of poorly water soluble drug“. In: *International Journal of Drug Delivery* 3.2 (2011), pp. 149–170 (cit. on p. 7).

[55]Ki-Taek Kim, Jae-Young Lee, Mee-Yeon Lee, et al. „Solid dispersions as a drug delivery system“. In: *Journal of pharmaceutical Investigation* 41.3 (2011), pp. 125–142 (cit. on p. 7).

[56]GA Hughes. „Nanostructure-mediated drug delivery“. In: *Nanomedicine* 1.1 (2005), pp. 22–30 (cit. on p. 7).

[57]Suresh Sagadevan and Mathan Periasamy. „A REVIEW ON ROLE OF NANOSTRUCTURES IN DRUG DELIVERY SYSTEM.“ In: *Reviews on Advanced Materials Science* 36.2 (2014) (cit. on p. 7).

[58]Suwussa Bamrungsap, Zilong Zhao, Tao Chen, et al. „Nanotechnology in therapeutics: a focus on nanoparticles as a drug delivery system“. In: *Nanomedicine* 7.8 (2012), pp. 1253–1271 (cit. on pp. 7, 9, 12).

[59]Kinam Park. „Nanotechnology: What it can do for drug delivery“. In: *Journal of controlled release: official journal of the Controlled Release Society* 120.1-2 (2007), p. 1 (cit. on p. 7).

[60]Justin Siefker, Pankaj Karande, and Marc-Olivier Coppens. „Packaging biological cargoes in mesoporous materials: opportunities for drug delivery“. In: *Expert opinion on drug delivery* 11.11 (2014), pp. 1781–1793 (cit. on p. 8).

[61]Simo Näkki, Jussi Rytkönen, Tuomo Nissinen, et al. „Improved stability and biocompatibility of nanostructured silicon drug carrier for intravenous administration“. In: *Acta biomaterialia* 13 (2015), pp. 207–215 (cit. on p. 8).

[62]S Köllner, S Dünnhaupt, C Waldner, et al. „Mucus permeating thiomer nanoparticles“. In: *European Journal of Pharmaceutics and Biopharmaceutics* 97 (2015), pp. 265–272 (cit. on p. 8).

[63]Mirkka P Sarparanta, Luis M Bimbo, Ermei M Mäkilä, et al. „The mucoadhesive and gastroretentive properties of hydrophobin-coated porous silicon nanoparticle oral drug delivery systems“. In: *Biomaterials* 33.11 (2012), pp. 3353–3362 (cit. on p. 8).

[64]Amy B Foraker, Rob J Walczak, Michael H Cohen, et al. „Microfabricated porous silicon particles enhance paracellular delivery of insulin across intestinal Caco-2 cell monolayers“. In: *Pharmaceutical research* 20.1 (2003), pp. 110–116 (cit. on p. 8).

[65]Rajesh Singh, Shailesh Singh, and James W Lillard. „Past, present, and future technologies for oral delivery of therapeutic proteins“. In: *Journal of pharmaceutical sciences* 97.7 (2008), pp. 2497–2523 (cit. on p. 8).

[66] Camile B Woitiski, Rui A Carvalho, António J Ribeiro, Ronald J Neufeld, and Francisco Veiga. „Strategies toward the improved oral delivery of insulin nanoparticles via gastrointestinal uptake and translocation“. In: *BioDrugs* 22.4 (2008), pp. 223–237 (cit. on p. 8).

[67] P Jani, GW Halbert, J Langridge, and AT Florence. „The uptake and translocation of latex nanospheres and microspheres after oral administration to rats“. In: *Journal of pharmacy and pharmacology* 41.12 (1989), pp. 809–812 (cit. on p. 8).

[68] Edith Mathiowitz, Jules S Jacob, Yong S Jong, et al. „Biologically erodable microspheres as potential oral drug delivery systems“. In: *Nature* 386.6623 (1997), p. 410 (cit. on p. 8).

[69] Sae-Hae Kim, Kyung-Yeol Lee, and Yong-Suk Jang. „Mucosal immune system and M cell-targeting strategies for oral mucosal vaccination“. In: *Immune network* 12.5 (2012), pp. 165–175 (cit. on p. 8).

[70] Anne des Rieux, Vincent Pourcelle, Patrice D Cani, Jacqueline Marchand-Brynaert, and Véronique Préat. „Targeted nanoparticles with novel non-peptidic ligands for oral delivery“. In: *Advanced drug delivery reviews* 65.6 (2013), pp. 833–844 (cit. on p. 8).

[71] Archana Swami, Jinjun Shi, Suresh Gadde, et al. „Nanoparticles for targeted and temporally controlled drug delivery“. In: *Multifunctional nanoparticles for drug delivery applications*. Springer, 2012, pp. 9–29 (cit. on p. 9).

[72] Vesa-Pekka Lehto, Jarno Salonen, Helder Santos, and Joakim Riikonen. „Nanostructured Silicon-Based Materials as a Drug Delivery System for Water-Insoluble Drugs“. In: *Drug Delivery Strategies for Poorly Water-Soluble Drugs*. Ed. by D Douroumis and A Fahr. Wiley, 2013, pp. 477–508 (cit. on pp. 9, 32).

[73] VJ Mohanraj and Y Chen. „Nanoparticles-a review“. In: *Tropical journal of pharmaceutical research* 5.1 (2006), pp. 561–573 (cit. on p. 9).

[74] José das Neves, Maria Fernanda Bahia, Mansoor M Amiji, and Bruno Sarmento. „Mucoadhesive nanomedicines: characterization and modulation of mucoadhesion at the nanoscale“. In: *Expert opinion on drug delivery* 8.8 (2011), pp. 1085–1104 (cit. on p. 9).

[75] Omid C Farokhzad and Robert Langer. „Impact of nanotechnology on drug delivery“. In: *ACS nano* 3.1 (2009), pp. 16–20 (cit. on p. 9).

[76] David A Lavan, Terry McGuire, and Robert Langer. „Small-scale systems for in vivo drug delivery“. In: *Nature biotechnology* 21.10 (2003), p. 1184 (cit. on p. 9).

[77] Rajesh Singh and James W Lillard Jr. „Nanoparticle-based targeted drug delivery“. In: *Experimental and molecular pathology* 86.3 (2009), pp. 215–223 (cit. on p. 9).

[78] Jayanth Panyam and Vinod Labhasetwar. „Biodegradable nanoparticles for drug and gene delivery to cells and tissue“. In: *Advanced drug delivery reviews* 55.3 (2003), pp. 329–347 (cit. on p. 9).

[79] Manisha P Desai, Vinod Labhasetwar, Gordon L Amidon, and Robert J Levy. „Gastrointestinal uptake of biodegradable microparticles: effect of particle size“. In: *Pharmaceutical research* 13.12 (1996), pp. 1838–1845 (cit. on p. 9).

[80]M Ann Clark, Mark A Jepson, and Barry H Hirst. „Exploiting M cells for drug and vaccine delivery“. In: *Advanced drug delivery reviews* 50.1-2 (2001), pp. 81–106 (cit. on p. 9).

[81]S Caban, E Aytekin, A Sahin, and Y Capan. „Nanosystems for drug delivery“. In: *OA Drug Des Deliv* 18.2 (2014), pp. 1–7 (cit. on pp. 9, 12).

[82]Luigi Battaglia and Marina Gallarate. „Lipid nanoparticles: state of the art, new preparation methods and challenges in drug delivery“. In: *Expert opinion on drug delivery* 9.5 (2012), pp. 497–508 (cit. on pp. 10, 11).

[83]Fardin Tamjidi, Mohammad Shahedi, Jaleh Varshosaz, and Ali Nasirpour. „Nanostructured lipid carriers (NLC): A potential delivery system for bioactive food molecules“. In: *Innovative Food Science & Emerging Technologies* 19 (2013), pp. 29–43 (cit. on p. 10).

[84]Sílvia S Guterres, Marta P Alves, and Adriana R Pohlmann. „Polymeric nanoparticles, nanospheres and nanocapsules, for cutaneous applications“. In: *Drug target insights* 2 (2007), p. 117739280700200002 (cit. on pp. 10, 11).

[85]Ketie Saralidze, Leo H Koole, and Menno LW Knetsch. „Polymeric microspheres for medical applications“. In: *Materials* 3.6 (2010), pp. 3537–3564 (cit. on p. 10).

[86]C Mayer. „Nanocapsules as drug delivery systems“. In: *The International journal of artificial organs* 28.11 (2005), pp. 1163–1171 (cit. on p. 11).

[87]Pavankumar Kothamasu, Hemanth Kanumur, Niranjan Ravur, et al. „Nanocapsules: the weapons for novel drug delivery systems“. In: *BioImpacts: BI* 2.2 (2012), p. 71 (cit. on p. 11).

[88]CE Mora-Huertas, Hatem Fessi, and Abdelhamid Elaissari. „Polymer-based nanocapsules for drug delivery“. In: *International journal of pharmaceutics* 385.1-2 (2010), pp. 113–142 (cit. on p. 11).

[89]Ngoc Trinh Huynh, C Passirani, Patrick Saulnier, and Jean-Pierre Benoit. „Lipid nanocapsules: a new platform for nanomedicine“. In: *International journal of pharmaceutics* 379.2 (2009), pp. 201–209 (cit. on p. 11).

[90]Qin Guo, Jie Cai, Pengyu Li, et al. „Comparison of bile salt/phosphatidylcholine mixed micelles in solubilization to sterols and stability“. In: *Drug design, development and therapy* 10 (2016), p. 3789 (cit. on p. 11).

[91]SR Croy and GS Kwon. „Polymeric micelles for drug delivery“. In: *Current pharmaceutical design* 12.36 (2006), pp. 4669–4684 (cit. on p. 11).

[92]R Neslihan Gursoy and Simon Benita. „Self-emulsifying drug delivery systems (SEDDS) for improved oral delivery of lipophilic drugs“. In: *Biomedicine & Pharmacotherapy* 58.3 (2004), pp. 173–182 (cit. on p. 11).

[93]Amarnath Sharma and Uma S Sharma. „Liposomes in drug delivery: progress and limitations“. In: *International journal of pharmaceutics* 154.2 (1997), pp. 123–140 (cit. on p. 11).

[94]Jung Seok Lee and Jan Feijen. „Polymersomes for drug delivery: design, formation and characterization“. In: *Journal of controlled release* 161.2 (2012), pp. 473–483 (cit. on p. 11).

[95] Mingjun Liu and Jean MJ Fréchet. „Designing dendrimers for drug delivery“. In: *Pharmaceutical science & technology today* 2.10 (1999), pp. 393–401 (cit. on p. 11).

[96] Thorsteinn Loftsson, Pekka Jarho, Mar Masson, and Tomi Järvinen. „Cyclodextrins in drug delivery“. In: *Expert opinion on drug delivery* 2.2 (2005), pp. 335–351 (cit. on p. 12).

[97] Gaurav Tiwari, Ruchi Tiwari, and Awani K Rai. „Cyclodextrins in delivery systems: Applications“. In: *Journal of Pharmacy and Bioallied Sciences* 2.2 (2010), p. 72 (cit. on p. 12).

[98] Allan S Hoffman. „The origins and evolution of controlled drug delivery systems“. In: *Journal of controlled release* 132.3 (2008), pp. 153–163 (cit. on p. 12).

[99] Nelson A Ochekpe, Patrick O Olorunfemi, and Ndidi C Ngwuluka. „Nanotechnology and drug delivery part 2: nanostructures for drug delivery“. In: *Tropical Journal of Pharmaceutical Research* 8.3 (2009) (cit. on p. 12).

[100] Madjid Soltani, Pu Chen, et al. „Nanotechnology in drug delivery systems“. In: *International Journal of Drug Delivery* 4.3 (2012), pp. 275–288 (cit. on p. 12).

[101] Juergen Siepmann and F Siepmann. „Mathematical modeling of drug delivery“. In: *International journal of pharmaceutics* 364.2 (2008), pp. 328–343 (cit. on p. 14).

[102] Juergen Siepmann, Ronald A Siegel, and Florence Siepmann. „Diffusion controlled drug delivery systems“. In: *Fundamentals and applications of controlled release drug delivery*. Springer, 2012, pp. 127–152 (cit. on pp. 14, 16).

[103] Juergen Siepmann and Florence Siepmann. „Modeling of diffusion controlled drug delivery“. In: *Journal of Controlled Release* 161.2 (2012), pp. 351–362 (cit. on p. 14).

[104] J Crank. *The mathematics of diffusion*. Oxford University Press, 1975 (cit. on p. 15).

[105] Takeru Higuchi. „Rate of release of medicaments from ointment bases containing drugs in suspension“. In: *Journal of pharmaceutical sciences* 50.10 (1961), pp. 874–875 (cit. on p. 15).

[106] R Baker and H Lonsdale. „Controlled Release: Mechanisms and Rates“. In: *Controlled Release of Biologically Active Agents*. Ed. by A Tanquary and R Lacey. Plenum: New York, 1974, pp. 15–71 (cit. on p. 16).

[107] Tamotsu Koizumi and Suwannee P Panomsuk. „Release of medicaments from spherical matrices containing drug in suspension: theoretical aspects“. In: *International journal of pharmaceutics* 116.1 (1995), pp. 45–49 (cit. on p. 16).

[108] Juergen Siepmann and Nicholas A Peppas. „Higuchi equation: derivation, applications, use and misuse“. In: *International journal of pharmaceutics* 418.1 (2011), pp. 6–12 (cit. on p. 17).

[109] J Siepmann and NA Peppas. „Modeling of drug release from delivery systems based on hydroxypropyl methylcellulose (HPMC)“. In: *Advanced drug delivery reviews* 64 (2012), pp. 163–174 (cit. on p. 17).

[110] Arthur A Noyes and Willis R Whitney. „The rate of solution of solid substances in their own solutions.“ In: *Journal of the American Chemical Society* 19.12 (1897), pp. 930–934 (cit. on p. 18).

[111] Magdalena Jarosz, Anna Pawlik, Michał Szuwarzyński, Marian Jaskuła, and Grzegorz D Sulka. „Nanoporous anodic titanium dioxide layers as potential drug delivery systems: Drug release kinetics and mechanism“. In: *Colloids and Surfaces B: Biointerfaces* 143 (2016), pp. 447–454 (cit. on p. 18).

[112] Paulo Costa and Jose Manuel Sousa Lobo. „Modeling and comparison of dissolution profiles“. In: *European journal of pharmaceutical sciences* 13.2 (2001), pp. 123–133 (cit. on p. 18).

[113] Philip L Ritger and Nikolaos A Peppas. „A simple equation for description of solute release II. Fickian and anomalous release from swellable devices“. In: *Journal of controlled release* 5.1 (1987), pp. 37–42 (cit. on p. 19).

[114] Kosmas Kosmidis, Panos Argyrakis, and Panos Macheras. „A reappraisal of drug release laws using Monte Carlo simulations: the prevalence of the Weibull function“. In: *Pharmaceutical research* 20.7 (2003), pp. 988–995 (cit. on p. 19).

[115] Amalia Hadjitheodorou and George Kalosakas. „Analytical and numerical study of diffusion-controlled drug release from composite spherical matrices“. In: *Materials Science and Engineering: C* 42 (2014), pp. 681–690 (cit. on p. 19).

[116] Amalia Hadjitheodorou and George Kalosakas. „Quantifying diffusion-controlled drug release from spherical devices using Monte Carlo simulations“. In: *Materials Science and Engineering: C* 33.2 (2013), pp. 763–768 (cit. on p. 19).

[117] EV Christidi and G Kalosakas. „Dynamics of the fraction of drug particles near the release boundary“. In: *The European Physical Journal Special Topics* 225.6-7 (2016), pp. 1245–1254 (cit. on p. 19).

[118] Vasiliki Papadopoulou, Kosmas Kosmidis, Marilena Vlachou, and Panos Macheras. „On the use of the Weibull function for the discernment of drug release mechanisms“. In: *International journal of pharmaceutics* 309.1-2 (2006), pp. 44–50 (cit. on p. 19).

[119] Maxime Ignacio, Mykyta V Chubynsky, and Gary W Slater. „Interpreting the Weibull fitting parameters for diffusion-controlled release data“. In: *Physica A: Statistical Mechanics and its Applications* 486 (2017), pp. 486–496 (cit. on p. 20).

[120] A Uhlir Jr. „Electrolytic shaping of germanium and silicon“. In: *Bell System Technical Journal* 35.2 (1956), pp. 333–347 (cit. on p. 21).

[121] Leigh T Canham. „Silicon quantum wire array fabrication by electrochemical and chemical dissolution of wafers“. In: *Applied Physics Letters* 57.10 (1990), pp. 1046–1048 (cit. on pp. 21, 29).

[122] V Lehmann. „The physics of macropore formation in low doped n-type silicon“. In: *Journal of the Electrochemical Society* 140.10 (1993), pp. 2836–2843 (cit. on pp. 22, 25).

[123] Michael J Sailor. *Porous silicon in practice: preparation, characterization and applications*. Wiley, 2012 (cit. on pp. 23, 24).

[124] D Graf, M Grundner, R Schulz, and L Muhlhoff. „Oxidation of HF-treated Si wafer surfaces in air“. In: *Journal of applied physics* 68.10 (1990), pp. 5155–5161 (cit. on pp. 23, 27).

[125]Michio Niwano, Jun-ichi Kageyama, Kazunari Kurita, et al. „Infrared spectroscopy study of initial stages of oxidation of hydrogen-terminated Si surfaces stored in air“. In: *Journal of applied physics* 76.4 (1994), pp. 2157–2163 (cit. on p. 23).

[126]D Gräf, M Grundner, and R Schulz. „Reaction of water with hydrofluoric acid treated silicon (111) and (100) surfaces“. In: *Journal of Vacuum Science & Technology A: Vacuum, Surfaces, and Films* 7.3 (1989), pp. 808–813 (cit. on p. 23).

[127]M Morita, T Ohmi, E Hasegawa, M Kawakami, and M Ohwada. „Growth of native oxide on a silicon surface“. In: *Journal of Applied Physics* 68.3 (1990), pp. 1272–1281 (cit. on p. 23).

[128]J Jakubowicz. „Nanoporous silicon fabricated at different illumination and electrochemical conditions“. In: *Superlattices and Microstructures* 41.4 (2007), pp. 205–215 (cit. on p. 23).

[129]H Jungblut, J Jakubowicz, S Schweizer, and HJ Lewerenz. „Mechanism of initial structure formation on highly doped n-Si (111)“. In: *Journal of Electroanalytical Chemistry* 527.1-2 (2002), pp. 41–46 (cit. on p. 23).

[130]MIJ Beale, JD Benjamin, MJ Uren, NG Chew, and AG Cullis. „An experimental and theoretical study of the formation and microstructure of porous silicon“. In: *Journal of Crystal Growth* 73.3 (1985), pp. 622–636 (cit. on p. 24).

[131]Robert Vajtai. *Springer handbook of nanomaterials*. Springer Science & Business Media, 2013 (cit. on p. 24).

[132]V Lehmann and S Ronnebeck. „The Physics of Macropore Formation in Low-Doped p-Type Silicon“. In: *Journal of The Electrochemical Society* 146.8 (1999), pp. 2968–2975 (cit. on p. 25).

[133]Elisabet Xifré Pérez. *Design, fabrication and characterization of porous silicon multilayer optical devices*. Universitat Rovira i Virgili, 2008 (cit. on pp. 25, 29).

[134]Stefan Guldin. *Inorganic nanoarchitectures by organic self-assembly*. Springer Science & Business Media, 2013 (cit. on p. 26).

[135]Vesna Janicki, Jordi Sancho-Parramon, Sergiy Yulin, Marcel Flemming, and Andrey Chuvilin. „Optical and structural properties of Nb2O5–SiO2 mixtures in thin films“. In: *Surface and Coatings Technology* 206.17 (2012), pp. 3650–3657 (cit. on p. 26).

[136]B Gauthier-Manuel. „Simultaneous determination of the thickness and optical constants of weakly absorbing thin films“. In: *Measurement Science and Technology* 9.3 (1998), p. 485 (cit. on p. 26).

[137]Leigh T Canham. „Properties of porous silicon“. In: Institution of Electrical Engineers. 1997 (cit. on pp. 27, 29).

[138]Xiaoge Gregory Zhang. *Electrochemistry of Silicon and its Oxide*. Springer Science & Business Media, 2007 (cit. on p. 28).

[139]Fabrizio Cattaruzza, Antonio Cricenti, Alberto Flamini, et al. „Carboxylic acid terminated monolayer formation on crystalline silicon and silicon nitride surfaces. A surface coverage determination with a fluorescent probe in solution“. In: *Journal of Materials Chemistry* 14.9 (2004), pp. 1461–1468 (cit. on p. 28).

[140]Michael P Stewart and Jillian M Buriak. „Exciton-mediated hydrosilylation on photoluminescent nanocrystalline silicon“. In: *Journal of the American Chemical Society* 123.32 (2001), pp. 7821–7830 (cit. on pp. 28, 29).

[141]Lawrence A Huck and Jillian M Buriak. „Toward a mechanistic understanding of exciton-mediated hydrosilylation on nanocrystalline silicon“. In: *Journal of the American Chemical Society* 134.1 (2011), pp. 489–497 (cit. on p. 28).

[142]J Salonen, V-P Lehto, M Björkqvist, E Laine, and L Niinistö. „Studies of thermally-carbonized porous silicon surfaces“. In: *physica status solidi (a)* 182.1 (2000), pp. 123–126 (cit. on p. 28).

[143]L Pavesi. „Porous silicon based light emitting diodes: a progress report“. In: *physica status solidi (a)* 165.1 (1998), pp. 91–96 (cit. on p. 29).

[144]TK Sham, DT Jiang, I Coulthard, et al. „Origin of luminescence from porous silicon deduced by synchrotron-light-induced optical luminescence“. In: *Nature* 363.6427 (1993), p. 331 (cit. on p. 29).

[145]MW Cole, JF Harvey, RA Lux, DW Eckart, and R Tsu. „Microstructure of visibly luminescent porous silicon“. In: *Applied physics letters* 60.22 (1992), pp. 2800–2802 (cit. on p. 29).

[146]Mita Dasog, Zhenyu Yang, Sarah Regli, et al. „Chemical insight into the origin of red and blue photoluminescence arising from freestanding silicon nanocrystals“. In: *Acs Nano* 7.3 (2013), pp. 2676–2685 (cit. on p. 29).

[147]Philippe M Fauchet. „Photoluminescence and electroluminescence from porous silicon“. In: *Journal of luminescence* 70.1-6 (1996), pp. 294–309 (cit. on p. 29).

[148]N Daldosso, A Ghafarinazari, P Cortelletti, et al. „Orange and blue luminescence emission to track functionalized porous silicon microparticles inside the cells of the human immune system“. In: *Journal of Materials Chemistry B* 2.37 (2014), pp. 6345–6353 (cit. on pp. 29, 30).

[149]Ravin Jugdaohsingh, Simon HC Anderson, Katherine L Tucker, et al. „Dietary silicon intake and absorption“. In: *The American journal of clinical nutrition* 75.5 (2002), pp. 887–893 (cit. on p. 30).

[150]Suet Peng Low, Keryn A Williams, Leigh T Canham, and Nicolas H Voelcker. „Generation of reactive oxygen species from porous silicon microparticles in cell culture medium“. In: *Journal of Biomedical Materials Research Part A: An Official Journal of The Society for Biomaterials, The Japanese Society for Biomaterials, and The Australian Society for Biomaterials and the Korean Society for Biomaterials* 93.3 (2010), pp. 1124–1131 (cit. on p. 30).

[151]Luis M Bimbo, Mirkka Sarparanta, Hélder A Santos, et al. „Biocompatibility of thermally hydrocarbonized porous silicon nanoparticles and their biodistribution in rats“. In: *ACS nano* 4.6 (2010), pp. 3023–3032 (cit. on p. 30).

[152]Emily J Anglin, Lingyun Cheng, William R Freeman, and Michael J Sailor. „Porous silicon in drug delivery devices and materials“. In: *Advanced drug delivery reviews* 60.11 (2008), pp. 1266–1277 (cit. on p. 30).

[153]Mirkka Sarparanta, Ermei Makila, Teemu Heikkila, et al. „18F-labeled modified porous silicon particles for investigation of drug delivery carrier distribution in vivo with positron emission tomography“. In: *Molecular pharmaceutics* 8.5 (2011), pp. 1799–1806 (cit. on p. 30).

[154]Edward Lansing Cussler. *Diffusion: mass transfer in fluid systems*. Cambridge university press, 2009 (cit. on p. 35).

[155]Gero Decher. „Fuzzy nanoassemblies: toward layered polymeric multicomposites“. In: *science* 277.5330 (1997), pp. 1232–1237 (cit. on p. 35).

[156]Herman Z Cummins. „Liquid, glass, gel: The phases of colloidal Laponite“. In: *Journal of Non-Crystalline Solids* 353.41-43 (2007), pp. 3891–3905 (cit. on p. 36).

[157]Kazutoshi Haraguchi. „Synthesis and properties of soft nanocomposite materials with novel organic/inorganic network structures“. In: *Polymer journal* 43.3 (2011), p. 223 (cit. on p. 36).

[158]Kan Tang and Nicolaas AM Besseling. „Formation of polyelectrolyte multilayers: ionic strengths and growth regimes“. In: *Soft Matter* 12.4 (2016), pp. 1032–1040 (cit. on p. 37).

[159]Eduardo Guzmán, Hernán Ritacco, José EF Rubio, Ramón G Rubio, and Francisco Ortega. „Salt-induced changes in the growth of polyelectrolyte layers of poly (diallyldimethylammonium chloride) and poly (4-styrene sulfonate of sodium)“. In: *Soft Matter* 5.10 (2009), pp. 2130–2142 (cit. on p. 37).

[160]Neal E Craft and Joseph H Soares. „Relative solubility, stability, and absorptivity of lutein and. beta.-carotene in organic solvents“. In: *Journal of Agricultural and Food Chemistry* 40.3 (1992), pp. 431–434 (cit. on pp. 40, 76).

[161]PS Kalsi. *Spectroscopy of organic compounds*. New Age International, 2007 (cit. on pp. 47, 89).

[162]Nicole L Fry, Gerry R Boss, and Michael J Sailor. „Oxidation-induced trapping of drugs in porous silicon microparticles“. In: *Chemistry of Materials* 26.8 (2014), pp. 2758–2764 (cit. on p. 49).

[163]My Ahmed Said Azizi Samir, Fannie Alloin, and Alain Dufresne. „Review of recent research into cellulosic whiskers, their properties and their application in nanocomposite field“. In: *Biomacromolecules* 6.2 (2005), pp. 612–626 (cit. on pp. 51, 53).

[164]Robert J Moon, Ashlie Martini, John Nairn, John Simonsen, and Jeff Youngblood. „Cellulose nanomaterials review: structure, properties and nanocomposites“. In: *Chemical Society Reviews* 40.7 (2011), pp. 3941–3994 (cit. on pp. 52–55).

[165]R Malcolm Brown Jr. „The biosynthesis of cellulose“. In: *Journal of Macromolecular Science, Part A: Pure and Applied Chemistry* 33.10 (1996), pp. 1345–1373 (cit. on p. 52).

[166]Inder M Saxena and R Malcolm Brown Jr. „Cellulose biosynthesis: current views and evolving concepts“. In: *Annals of botany* 96.1 (2005), pp. 9–21 (cit. on p. 52).

[167]Antoinette C O'sullivan. „Cellulose: the structure slowly unravels“. In: *Cellulose* 4.3 (1997), pp. 173–207 (cit. on p. 53).

[168]Yoshiharu Nishiyama. „Structure and properties of the cellulose microfibril“. In: *Journal of wood science* 55.4 (2009), pp. 241–249 (cit. on p. 53).

[169] Yoshiharu Nishiyama, Paul Langan, and Henri Chanzy. „Crystal structure and hydrogen-bonding system in cellulose Iβ from synchrotron X-ray and neutron fiber diffraction“. In: *Journal of the American Chemical Society* 124.31 (2002), pp. 9074–9082 (cit. on p. 53).

[170] Yoshiharu Nishiyama, Junji Sugiyama, Henri Chanzy, and Paul Langan. „Crystal structure and hydrogen bonding system in cellulose Iα from synchrotron X-ray and neutron fiber diffraction“. In: *Journal of the American Chemical Society* 125.47 (2003), pp. 14300–14306 (cit. on p. 53).

[171] Junji Sugiyama, Roger Vuong, and Henri Chanzy. „Electron diffraction study on the two crystalline phases occurring in native cellulose from an algal cell wall“. In: *Macromolecules* 24.14 (1991), pp. 4168–4175 (cit. on pp. 53, 54).

[172] Tomoya Imai, Jean-Luc Putaux, and Junji Sugiyama. „Geometric phase analysis of lattice images from algal cellulose microfibrils“. In: *Polymer* 44.6 (2003), pp. 1871–1879 (cit. on p. 54).

[173] Shinichiro Iwamoto, Kentaro Abe, and Hiroyuki Yano. „The effect of hemicelluloses on wood pulp nanofibrillation and nanofiber network characteristics“. In: *Biomacromolecules* 9.3 (2008), pp. 1022–1026 (cit. on p. 54).

[174] Tsuguyuki Saito, Yoshiharu Nishiyama, Jean-Luc Putaux, Michel Vignon, and Akira Isogai. „Homogeneous suspensions of individualized microfibrils from TEMPO-catalyzed oxidation of native cellulose“. In: *Biomacromolecules* 7.6 (2006), pp. 1687–1691 (cit. on p. 54).

[175] Richard K Johnson, Audrey Zink-Sharp, Scott H Renneckar, and Wolfgang G Glasser. „A new bio-based nanocomposite: fibrillated TEMPO-oxidized celluloses in hydroxypropylcellulose matrix“. In: *Cellulose* 16.2 (2009), pp. 227–238 (cit. on p. 54).

[176] Tsuguyuki Saito, Masayuki Hirota, Naoyuki Tamura, et al. „Individualization of nano-sized plant cellulose fibrils by direct surface carboxylation using TEMPO catalyst under neutral conditions“. In: *Biomacromolecules* 10.7 (2009), pp. 1992–1996 (cit. on p. 54).

[177] MF Semmelhack, Chuen S Chou, and David A Cortes. „Nitroxyl-mediated electrooxidation of alcohols to aldehydes and ketones“. In: *Journal of the American Chemical Society* 105.13 (1983), pp. 4492–4494 (cit. on p. 55).

[178] T Saito, Y Okita, TT Nge, J Sugiyama, and A Isogai. „TEMPO-mediated oxidation of native cellulose: Microscopic analysis of fibrous fractions in the oxidized products“. In: *Carbohydrate polymers* 65.4 (2006), pp. 435–440 (cit. on p. 55).

[179] Arjan EJ de Nooy, Arie C Besemer, and Herman van Bekkum. „Selective oxidation of primary alcohols mediated by nitroxyl radical in aqueous solution. Kinetics and mechanism“. In: *Tetrahedron* 51.29 (1995), pp. 8023–8032 (cit. on pp. 55, 57).

[180] AEJ De Nooy, AC Besemer, and H Van Bekkum. „Highly selective TEMPO mediated oxidation of primary alcohol groups in polysaccharides“. In: *Recueil des Travaux Chimiques des Pays-Bas* 113.3 (1994), pp. 165–166 (cit. on p. 55).

[181] Daniel O Carlsson, Jonas Lindh, Maria Strømme, and Albert Mihranyan. „Susceptibility of Iα-and Iβ-dominated cellulose to TEMPO-mediated oxidation“. In: *Biomacromolecules* 16.5 (2015), pp. 1643–1649 (cit. on p. 55).

[182]Yusuke Okita, Tsuguyuki Saito, and Akira Isogai. „Entire surface oxidation of various cellulose microfibrils by TEMPO-mediated oxidation“. In: *Biomacromolecules* 11.6 (2010), pp. 1696–1700 (cit. on p. 55).

[183]Akira Isogai, Tsuguyuki Saito, and Hayaka Fukuzumi. „TEMPO-oxidized cellulose nanofibers“. In: *nanoscale* 3.1 (2011), pp. 71–85 (cit. on p. 56).

[184]Youssef Habibi. „Key advances in the chemical modification of nanocelluloses“. In: *Chemical Society Reviews* 43.5 (2014), pp. 1519–1542 (cit. on p. 56).

[185]Ryuji Shinoda, Tsuguyuki Saito, Yusuke Okita, and Akira Isogai. „Relationship between length and degree of polymerization of TEMPO-oxidized cellulose nanofibrils“. In: *Biomacromolecules* 13.3 (2012), pp. 842–849 (cit. on p. 57).

[186]Tsuguyuki Saito, Satoshi Kimura, Yoshiharu Nishiyama, and Akira Isogai. „Cellulose nanofibers prepared by TEMPO-mediated oxidation of native cellulose“. In: *Biomacromolecules* 8.8 (2007), pp. 2485–2491 (cit. on pp. 57, 59).

[187]Enas M Ahmed. „Hydrogel: Preparation, characterization, and applications: A review“. In: *Journal of advanced research* 6.2 (2015), pp. 105–121 (cit. on p. 57).

[188]M Georg and TE Abraham. „Poly ionic hydrocolloids for intestinal delivery of protein drugs: alginate and chitosan“. In: *J Control Release* 114 (2006), pp. 1–14 (cit. on p. 57).

[189]Kytai Truong Nguyen and Jennifer L West. „Photopolymerizable hydrogels for tissue engineering applications“. In: *Biomaterials* 23.22 (2002), pp. 4307–4314 (cit. on p. 57).

[190]Peter Cass, Warren Knower, Eliana Pereeia, Natalie P Holmes, and Tim Hughes. „Preparation of hydrogels via ultrasonic polymerization“. In: *Ultrasonics sonochemistry* 17.2 (2010), pp. 326–332 (cit. on p. 57).

[191]Bin Fei, Radoslaw A Wach, Hiroshi Mitomo, Fumio Yoshii, and Tamikazu Kume. „Hydrogel of biodegradable cellulose derivatives. I. Radiation-induced crosslinking of CMC“. In: *Journal of Applied Polymer Science* 78.2 (2000), pp. 278–283 (cit. on p. 57).

[192]Radoslaw A Wach, Hiroshi Mitomo, Fumio Yoshii, and Tamikazu Kume. „Hydrogel of biodegradable cellulose derivatives. II. Effect of some factors on radiation-induced crosslinking of CMC“. In: *Journal of Applied Polymer Science* 81.12 (2001), pp. 3030–3037 (cit. on p. 57).

[193]Chunyu Chang and Lina Zhang. „Cellulose-based hydrogels: Present status and application prospects“. In: *Carbohydrate polymers* 84.1 (2011), pp. 40–53 (cit. on p. 58).

[194]Azadeh Bashari, Anahita Rouhani Shirvan, and Mina Shakeri. „Cellulose-based hydrogels for personal care products“. In: *Polymers for Advanced Technologies* (2018) (cit. on p. 58).

[195]Lihui Weng, Lina Zhang, Dong Ruan, Lianghe Shi, and Jian Xu. „Thermal gelation of cellulose in a NaOH/thiourea aqueous solution“. In: *Langmuir* 20.6 (2004), pp. 2086–2093 (cit. on p. 58).

[196]L Li, PM Thangamathesvaran, CY Yue, et al. „Gel network structure of methylcellulose in water“. In: *Langmuir* 17.26 (2001), pp. 8062–8068 (cit. on p. 58).

[197] Heinrich Thiele. „Richtwirkung von Ionen auf anisotrope Kolloide-Ionotropie“. In: *Naturwissenschaften* 34.4 (1947), pp. 123–123 (cit. on p. 58).

[198] Gregor T Grant, Edwin R Morris, David A Rees, Peter JC Smith, and David Thom. „Biological interactions between polysaccharides and divalent cations: the egg-box model“. In: *FEBS letters* 32.1 (1973), pp. 195–198 (cit. on p. 58).

[199] Cecilia Ada Maestri, Michela Abrami, Sharon Hazan, et al. „Role of sonication pretreatment and cation valence in the sol-gel transition of nano-cellulose suspensions“. In: *Scientific reports* 7.1 (2017), p. 11129 (cit. on p. 58).

[200] Takahiro Yano, Sacha Kassovska-Bratinova, J Shin Teh, et al. „Reduction of clofazimine by mycobacterial Type 2 NADH: Quinone oxidoreductase a pathway for the generation of bactericidal levels of reactive oxygen species“. In: *Journal of Biological Chemistry* 286.12 (2011), pp. 10276–10287 (cit. on p. 62).

[201] Yang Meng, Chenyu Wu, Jiaxing Zhang, et al. „Amphiphilic alginate as a drug release vehicle for water-insoluble drugs“. In: *Colloid Journal* 77.6 (2015), pp. 754–760 (cit. on p. 62).

[202] Haichen Nie, Huaping Mo, Mingtao Zhang, et al. „Investigating the interaction pattern and structural elements of a drug–polymer complex at the molecular level“. In: *Molecular pharmaceutics* 12.7 (2015), pp. 2459–2468 (cit. on p. 62).

[203] Hans Bisswanger. *Enzyme kinetics: principles and methods*. Wiley, 2017 (cit. on p. 62).

[204] Cecilia Ada Maestri, Paolo Bettotti, and Marina Scarpa. „Fabrication of complex-shaped hydrogels by diffusion controlled gelation of nanocellulose crystallites“. In: *Journal of Materials Chemistry B* 5.40 (2017), pp. 8096–8104 (cit. on p. 64).

[205] Philip L Ritger and Nikolaos A Peppas. „A simple equation for description of solute release I. Fickian and non-fickian release from non-swellable devices in the form of slabs, spheres, cylinders or discs“. In: *Journal of controlled release* 5.1 (1987), pp. 23–36 (cit. on p. 66).

[206] Hong Dong, James F Snyder, Kristen S Williams, and Jan W Andzelm. „Cation-induced hydrogels of cellulose nanofibrils with tunable moduli“. In: *Biomacromolecules* 14.9 (2013), pp. 3338–3345 (cit. on p. 67).

[207] Masrat Maswal, Oyais Ahmad Chat, Suraya Jabeen, et al. „Solubilization and cosolubilization of carbamazepine and nifedipine in mixed micellar systems: insights from surface tension, electronic absorption, fluorescence and HPLC measurements“. In: *RSC Advances* 5.10 (2015), pp. 7697–7712 (cit. on p. 71).

[208] Nuzhat Rehman, Mohammad Amin Mir, Musarat Jan, et al. „Mixed micellization and interfacial properties of polyoxyethylene sorbitan esters with cetylpyridinium chloride: a tensiometric study“. In: *Journal of surfactants and detergents* 12.4 (2009), pp. 295–304 (cit. on p. 71).

[209] Liliana De Campo, Anan Yaghmur, Nissim Garti, et al. „Five-component food-grade microemulsions: structural characterization by SANS“. In: *Journal of colloid and interface science* 274.1 (2004), pp. 251–267 (cit. on p. 71).

[210] Christian Wischke and Steven P Schwendeman. „Principles of encapsulating hydrophobic drugs in PLA/PLGA microparticles“. In: *International Journal of pharmaceutics* 364.2 (2008), pp. 298–327.

[211] Sandra Klein. „The use of biorelevant dissolution media to forecast the in vivo performance of a drug“. In: *The AAPS journal* 12.3 (2010), pp. 397–406.

[212] M Vallet-Regi, A Ramila, RP Del Real, and J Pérez-Pariente. „A new property of MCM-41: drug delivery system“. In: *Chemistry of Materials* 13.2 (2001), pp. 308–311.

[213] J Salonen, L Laitinen, AM Kaukonen, et al. „Mesoporous silicon microparticles for oral drug delivery: loading and release of five model drugs“. In: *Journal of controlled release* 108.2-3 (2005), pp. 362–374.

[214] Fangqiong Tang, Linlin Li, and Dong Chen. „Mesoporous silica nanoparticles: synthesis, biocompatibility and drug delivery“. In: *Advanced materials* 24.12 (2012), pp. 1504–1534.

[215] Yu Chen, Hangrong Chen, Limin Guo, et al. „Hollow/rattle-type mesoporous nanostructures by a structural difference-based selective etching strategy“. In: *ACS nano* 4.1 (2009), pp. 529–539.

[216] Weixia Qing, Yong Wang, Youyou Wang, et al. „The modified nanocrystalline cellulose for hydrophobic drug delivery“. In: *Applied Surface Science* 366 (2016), pp. 404–409.

[217] Jindrayani Nyoo Putro, Suryadi Ismadji, Chintya Gunarto, et al. „The effect of surfactants modification on nanocrystalline cellulose for paclitaxel loading and release study“. In: *Journal of Molecular Liquids* (2019).

[218] Shuangjiang Feng, Shuxue Wang, Yuanfei Lv, et al. „Dual pH-and thermal-responsive nanocomposite hydrogels for controllable delivery of hydrophobic drug baicalein“. In: *Polymer International* 68.3 (2019), pp. 494–502.

[219] Shiqi Wang, Reva Attah, Jiali Li, Yitong Chen, and Rongjun Chen. „A pH-responsive amphiphilic hydrogel based on pseudopeptides and poly (ethylene glycol) for oral delivery of hydrophobic drugs“. In: *ACS Biomaterials Science & Engineering* 4.12 (2018), pp. 4236–4243.

[220] Chayanika Deka, Deepanwita Deka, Montu Moni Bora, Dhruva Kumar Jha, and Dilip Kumar Kakati. „Investigation of pH-Sensitive Swelling and Curcumin Release Behavior of Chitglc Hydrogel“. In: *Journal of Polymers and the Environment* 26.10 (2018), pp. 4034–4045.

[221] Amey S Puranik, Ludovic P Pao, Vanessa M White, and Nicholas A Peppas. „In vitro evaluation of pH-responsive nanoscale hydrogels for the oral delivery of hydrophobic therapeutics“. In: *Industrial & Engineering Chemistry Research* 55.40 (2016), pp. 10576–10590.

[222] Zipei Zhang, Ruojie Zhang, and David Julian McClements. „Encapsulation of β-carotene in alginate-based hydrogel beads: Impact on physicochemical stability and bioaccessibility“. In: *Food Hydrocolloids* 61 (2016), pp. 1–10.

[223] Graziela VL Gomes, Mirella R Sola, Luís FP Marostegan, et al. „Physico-chemical stability and in vitro digestibility of beta-carotene-loaded lipid nanoparticles of cupuacu butter (Theobroma grandiflorum) produced by the phase inversion temperature (PIT) method“. In: *Journal of Food Engineering* 192 (2017), pp. 93–102.

[224] Like Mao, Di Wang, Fuguo Liu, and Yanxiang Gao. „Emulsion design for the delivery of β-carotene in complex food systems“. In: *Critical reviews in food science and nutrition* 58.5 (2018), pp. 770–784.

[225] Dieter Horn and Jens Rieger. „Organic nanoparticles in the aqueous phasetheory, experiment, and use“. In: *Angewandte Chemie International Edition* 40.23 (2001), pp. 4330–4361.

[226] Richard P Sear. „Nucleation: theory and applications to protein solutions and colloidal suspensions“. In: *Journal of Physics: Condensed Matter* 19.3 (2007), p. 033101.

[227] Qiang Zeng and Shilang Xu. „Thermodynamics and characteristics of heterogeneous nucleation on fractal surfaces“. In: *The Journal of Physical Chemistry C* 119.49 (2015), pp. 27426–27433.

[228] Ying-Xin Liu, Xiu-Juan Wang, Jie Lu, and Chi-Bun Ching. „Influence of the roughness, topography, and physicochemical properties of chemically modified surfaces on the heterogeneous nucleation of protein crystals“. In: *The Journal of Physical Chemistry B* 111.50 (2007), pp. 13971–13978.

[229] Simona Fermani, Chiara Vettraino, Irene Bonacini, et al. „Heterogeneous Crystallization of Proteins: Is it a Prenucleation Clusters Mediated Process?“ In: *Crystal Growth & Design* 13.7 (2013), pp. 3110–3115.

[230] Graham W Burton, Janusz Daroszewski, James G Nickerson, et al. „β-Carotene autoxidation: oxygen copolymerization, non-vitamin A products, and immunological activity“. In: *Canadian Journal of Chemistry* 92.4 (2014), pp. 305–316.

[231] Mindaugas Macernis, Juozas Sulskus, Svetlana Malickaja, Bruno Robert, and Leonas Valkunas. „Resonance Raman spectra and electronic transitions in carotenoids: a density functional theory study“. In: *The Journal of Physical Chemistry A* 118.10 (2014), pp. 1817–1825.

[232] S Schlücker, A Szeghalmi, M Schmitt, J Popp, and W Kiefer. „Density functional and vibrational spectroscopic analysis of β-carotene“. In: *Journal of Raman Spectroscopy* 34.6 (2003), pp. 413–419.

[233] Craig P Marshall and Alison Olcott Marshall. „The potential of Raman spectroscopy for the analysis of diagenetically transformed carotenoids“. In: *Philosophical Transactions of the Royal Society of London A: Mathematical, Physical and Engineering Sciences* 368.1922 (2010), pp. 3137–3144.